ASTROPHYSICAL USES OF CMB LENSING

Sudeep Das

A DISSERTATION

PRESENTED TO THE FACULTY

OF PRINCETON UNIVERSITY

IN CANDIDACY FOR THE DEGREE

OF DOCTOR OF PHILOSOPHY

RECOMMENDED FOR ACCEPTANCE

BY THE DEPARTMENT OF

ASTROPHYSICAL SCIENCES

Adviser: David N. Spergel

November 2008

Abstract

The future of Cosmic Microwave Background (CMB) research lies in exploiting the arcminute scale secondary anisotropies which encode information about the late time interaction of the CMB photons with the structure in the Universe. A specific form of such interaction is the gravitational lensing of the CMB photons by intervening matter - the main topic of this thesis. Upcoming experiments like the Atacama Cosmology Telescope (ACT) and PLANCK will measure these anisotropies with unprecedented resolution and sensitivity. In four separate papers, laid out as four chapters in this thesis, we present new techniques to model and analyze such high resolution data and explore the implications of such measurements on Cosmology, mainly in the context of CMB lensing. The first chapter describes a novel and accurate method for simulating high resolution lensed CMB maps by ray-tracing through a large scale structure simulation. This method does not adopt the flat sky approximation and retains information from large angular scales in the dark matter distribution. Maps simulated through this method will be instrumental in developing the detection and analysis techniques for CMB lensing in high resolution CMB experiments like ACT. In the second chapter, we describe a new and efficient method for measuring the power spectrum of arcminute resolution CMB maps. At these resolutions, the CMB power spectrum is extremely red and is prone to aliasing of power due to hard edges and point source masks. By combining two new techniques, namely, prewhitening and the adaptive multitaper method, we show that these problems can be efficiently remedied and the uncertainties in the final power spectrum estimate can be reduced by several factors over those obtainable by the now standard methods. These techniques will be also useful for estimat-

ing higher order statistics from the maps, like the ones related to the detection of CMB lensing and its cross-correlation with large scale structure tracers. In the third chapter, we explore how such cross-correlations can be turned into Cosmological probes. We propose an estimator for cosmological distance ratios based on the cross-correlation of galaxy counts with the gravitational lensing of galaxies and the CMB and show that it can be measured to sufficient accuracy in future experiments so as to provide useful constraints on curvature and dark energy evolution. Finally, we show that CMB lensing can be used to constrain the void and the texture hypotheses that have been put forward for explaining the intriguing *Cold Spot anomaly* in the WMAP data.

Acknowledgements

My deep interest in Physics and Cosmology, which has eventually led to this thesis, has been seeded and nurtured over the years by various acquaintances. Looking back, I think that the longest lasting influence has been the stimulating têtê-à-têtê I used to have over idle hours with my long time friend, Subhajit Chatterjee, while we were in school. Most of these would germinate from popular science books or articles, many of them technically beyond the scope of our limited comprehension at that age, but they helped seed a deep awe for the workings of Nature in my mind. Years later, he gifted me a copy of the wonderful book, "The First Three Minutes" by Steven Weinberg, which was my first exposure to Cosmology and an instant *coup de foudre*. During these early years, I came in contact with many great educators, and I specially thank Dipankar Das, Prabhash Tewari and Indrani Chakraborty for teaching me to think outside the box.

The foundations of my knowledge in Physics was mostly laid in the carefree but intensely stimulating atmosphere of Presidency College, Calcutta. There, studying outside the syllabus was the norm, and I was exposed to such classics as the Landau series and the Feynman Lectures, through the guidance of eminent teachers like Dipanjan Rai Chaudhuri, Debapriyo Shyam and Mira De, to whom I am thoroughly indebted. I also learned a lot from classmates and seniors at college: Rahul Biswas, Tapomoy Guha and Rajdeep Sensarma, to name a few.

It was also at Presidency that I met Sanghamitra Deb, who has made this world a better place for me. I am deeply grateful to her for standing by me all these years; caring, understanding, enduring and inspiring.

At the Indian Institute of Technology, Kanpur, I received constant encouragement from eminent professors like Alak K. Majumdar, Satish D. Joglekar, Debashish Chowdhury and Pankaj Jain, to whom I am deeply grateful. My sincere thanks to Domenico Marinucci and Nicola Vittorio at the University of Rome, Tor Vergata, for the exceptional summer research experience in their group, which exposed me to CMB physics.

The first year WMAP results were published when I was working in Rome and for the next few days everyone there seemed to be engulfed by the Spergel et al. paper. Incidentally, my project in Rome was also based on a paper by Komatsu and Spergel, and I came to like both papers so much that I secretly wished I could work with David Spergel some day. Therefore, coming to Princeton was a dream come true for me and working with David was even more so. I found him not only an excellent and caring adviser, but also an educator of a discipline that goes beyond just doing research. Working with him has not only taught me the tricks of the trade, but also to be a critical but impartial scientist. I must admit that during my first meetings with him, I could hardly understand most of what he said without delving into it for a week after the conversation. But over time, the lag between listening to him and registering what he meant has slowly disappeared - revealing his style of letting students grow independently, with occasional nudges in the right direction. I am grateful to him for his continuous encouragement during the course of the thesis and his patience, understanding and guidance during times when progress seemed stymied. On a separate note, I also thank him for the graduate student espresso machine - it has injected a new vibrancy in the cultural scene of the basement, enough to make the staunchest avoider of the basement stop and exclaim: "Set a new course. There's coffee in that nebula!".

I have also learned a great deal from Jerry Ostriker, who taught me the basic principles of gravitational lensing. I also thank him for agreeing to be a Reader for my thesis. His sharp intellect and breadth of knowledge has been a continuous source of inspiration. I am also indebted to Bohdan Paczynscky, Jeremy Goodman, Bruce Draine, Jim Gunn and Scott Tremaine for the excellent courses they taught. I regret not to have been able to work with Bohdan before he passed away. I have immensely enjoyed working with Paul

Bode, who has been ever so helpful and has always painstakingly answered my detailed queries about the nitty-gritties of simulations. It has been a pleasure to have collaborated with Amir Hajian, whose perseverance and positive attitude has inspired me. Without his help and enthusiasm, the power spectrum estimation paper would not have been possible. I also thank Joanna Dunkley, Viviana Acquaviva, Yen-Ting Lin and Neelima Sehgal for numerous stimulating discussions - I learned a lot from each of them. I will always cherish the detailed technical discussions I had with Chris Hirata and I am grateful to him for his suggestions in the CMB lensing simulation project and for letting me adapt his spherical harmonic transform code for my purpose.

Since I got involved in the Atacama Cosmology Telescope Project, I have worked very closely with Toby Marriage, who has been a constant source of inspiration. Over the numerous hours that we have worked together, I have learned much from him, not only about science and code writing, but also in terms of discipline and organization. He has been a great friend. I am grateful to Lyman Page, for agreeing to be on my thesis committee and for his thoughtful comments on my thesis as a Reader. I also thank him for providing me with a workspace in Jadwin, when Peyton Hall was under renovation.

Life in the basement would be boring but for the wonderful Creatures that dwell there. Each and everyone of them, have, in their own way, made my graduate student life cheerful. I am specially grateful to Aurelien, Ed, Simon, Nadia, Nicole, Will, Shirley, Eric, Katie and Ian for their continuous help and support from the day I arrived here. Kudos to Khee-Gan for keeping the coffee flowing! I also thank Beth Reid for being great friend. Among acquaintances outside the department, I am specially thankful to Subhayu Basu and Kunal Dasgupta for friendships I will always cherish.

I would like to thank Jill Knapp and Jim Stone for making my graduate student life smooth and full of encouragement. Mindy Lipman has been wonderful and has helped me on innumerable occasions, starting from the very day I accepted Princeton's offer! Charlotte Zanidakis is an absolute marvel - she has helped me with visas, with submission of applications when I was sitting in a desert town in Chile, and has made sure that each

an every step leading to my dissertation was completed on time. She is the most efficient academic administrator I have ever known! I thank Suzy Chaos, Marlene Levine and Irene Renda for helping me on various occasions. Kudos to Susan Dawson for being a beacon of excellence and efficiency - there would be many complicated issues that I would have been entangled in if not for her continuous support. Any measure of gratitude would fall short of what she deserves for clearing up the very complicated situation I was in during the last couple of months of my thesis, due to my loss of student status. Although it seemed next to impossible, she used her unparalleled knowledge of the system to make sure that I was not left without financial support during that time!

I am grateful to the Princeton University Graduate School for its continuous encouragement and also for support through the Charlotte Elizabeth Procter Fellowship during my final year.

I would like to end by saying that nothing would have been possible without the dedication that my parents, Dr. Swapan Kumar Das and Mrs. Jharna Das, has shown towards my education. Throughout, they have respected my choices and encouraged me full-heartedly in everything I wanted to pursue. They taught me never to be daunted by failure, to stand up and carry myself with dignity.

Preface

This thesis consists of four chapters and an appendix. The introduction to the first chapter serves as a brief introduction to the thesis and discusses some of the potentialities of CMB lensing. Each chapter constitutes a paper, which has been or will be submitted to a journal for peer review, as detailed below. In the following, I delineate my personal contribution to each paper and provide a complete list of collaborators on each project. Detailed acknowledgements for each paper has been appended to the end of each chapter.

Chapter 1

A Large Sky Simulation of the Gravitational Lensing of the Cosmic Microwave Background

Sudeep Das and Paul Bode

Astrophysical Journal 682 (2008) 1

I performed all analytical calculations in the paper and wrote the lensing code. The text was written by me under the guidance of David Spergel and Paul Bode. The original idea of performing CMB lensing simulations in a spherical sky geometry was suggested by David Spergel. The large scale structure light-cone simulation was performed by Paul Bode, from which spherical shells were extracted and projected onto HEALPix pixels using a plug-in that I wrote. The spherical harmonic transform operations are based on the Non-isolatitute Spherical Harmonic Transform code generously provided to me by Chris Hirata. During the development of the project, I has numerous useful discussions with David Spergel and Chris Hirata for which I am grateful to both.

Chapter 2

Efficient Power Spectrum Estimation for High Resolution CMB Maps

Sudeep Das, Amir Hajian and David N. Spergel

Submitted to Physical Review D. ArXiv identifier: arXiv:0809.1092v1

The results in this paper are produced by a new power spectrum estimation code, called `TaperMaster`, which I have developed with Amir Hajian. I wrote the text under the guidance of David Spergel and Amir Hajian. The original idea of using the multitaper method was suggested to us by the late eminent geophysicist F. A. Dahlen. The real space prewhitening filter was proposed by David Spergel.

Chapter 3

Measuring Distance-ratios with CMB-galaxy Lensing Cross-Correlations

Sudeep Das and David N. Spergel

To be submitted to Physical Review D.

This project grew out of a discussion between me and David Spergel regarding the generalization of the cosmographic method to include CMB lensing. I performed all numerical and analytical calculations in the paper. For this paper, I developed a general purpose Fisher Matrix code including CMB lensing, which can be used to predict the parameter constraints achievable with upcoming and proposed experiments like Planck and CMBPOL.

Chapter 4

CMB Lensing and the WMAP Cold Spot

Sudeep Das and David N. Spergel

To be submitted to Physical Review D.

I wrote this paper under the guidance of David Spergel. Part of this work was done at the APC, Paris. I am grateful for their hospitality.

Appendix

Next Generation Redshift Surveys and the Origin of Cosmic Acceleration

Viviana Acquaviva, Amir Hajian, David N. Spergel and Sudeep Das

Physical Review D. 78 (2008) 043514

This paper was led by Viviana Acquaviva, Amir Hajian and David Spergel. My contribution to the paper was to predict how well CMB lensing can constrain the bias of the various large scale structure tracers, thereby reducing the uncertainty in the proposed estimator. I have included this paper in the thesis, because the method of constraining bias with CMB lensing cross-correlations will become a very important astrophysical tool in future, especially for the upcoming high redshift galaxy surveys, like the Herschel mission and will help in the understanding of galaxy formation, evolution and assembly.

Contents

Abstract **iii**

Acknowledgements **v**

Preface **ix**

List of Figures **xv**

List of Tables **xxvii**

1 A Large Sky Simulation of the Gravitational Lensing of the Cosmic Microwave Background **1**

1.1 Introduction 2

1.2 The Lensing Algorithm 7

1.2.1 Basic Equations 7

1.2.2 Discretization 8

1.2.3 Connection with effective lensing quantities 10

1.2.4 Multiple plane ray tracing 13

1.2.5 Interpolation on the sphere 15

1.3 Generation of the lensing planes 19

1.3.1 From the box to the sphere 19

1.3.2 From surface density to convergence 21

1.3.3 The unlensed CMB map 21

1.4 Measuring Angular Power Spectra . . . 21
1.5 Results . . . 26
1.6 Tests . . . 27
1.6.1 Tests for the mass sheets . . . 27
1.6.2 Tests for the convergence plane . . . 28
1.6.3 Tests for the lensed CMB map . . . 29
1.7 Conclusions . . . 30

Acknowledgements **42**

References **43**

2 Efficient Power Spectrum Estimation for High Resolution CMB Maps **46**
2.1 Introduction . . . 47
2.2 A Brief Review of the Multitaper Method . . . 49
2.2.1 Notations . . . 50
2.2.2 1-D Multitaper Theory . . . 50
2.2.3 Adaptive MTM . . . 56
2.2.4 AMTM in two dimensions . . . 58
2.2.5 Statistical Properties . . . 61
2.3 Application to the ideal CMB map . . . 63
2.4 Prewhitening for CMB Maps with mask and noise . . . 71
2.4.1 Prewhitening of noiseless CMB maps . . . 72
2.4.2 Prewhitening of Noisy Maps . . . 77
2.5 Mode-mode coupling and deconvolution . . . 79
2.6 Conclusion . . . 86
2.A Appendix: Statistical properties of multitaper estimators . . . 89
2.B Appendix: Mode-mode coupling matrix . . . 91

Acknowledgements **95**

References **96**

3 Measuring Distance-ratios with CMB-galaxy Lensing Cross-Correlations 99

3.1 Introduction 100

3.2 Lensing Ratio: The key observable 101

3.3 Upcoming surveys and a new probe of dark energy and curvature 103

3.4 Parameter constraints 106

3.5 Conclusions 113

3.A BAO and lensing ratios as probes of early dark energy 114

References **117**

4 CMB Lensing and the WMAP Cold Spot **119**

4.1 Introduction 119

4.2 Lensing by the Void 121

4.3 Lensing by the Texture 122

4.4 Can CMB Observations Detect Voids and Textures? 125

4.5 Conclusion 128

Acknowledgements **131**

References **132**

A Next Generation Redshift Surveys and the Origin of Cosmic Acceleration 135

A.1 Introduction 136

A.2 f(R) theories in the PPF formalism 137

A.3 Measuring the growth of structure 139

A.4 Results 144

A.5 Conclusions and discussion 146

References **148**

List of Figures

1.1 Geometry illustrating the point remapping used in the text 11

1.2 Geometry illustrating the multiple plane ray tracing method. 13

1.3 CMBVIEW 32

1.4 Effect of apodization of the window function. The continuous line is the unlensed CMB power spectrum and the dashed line is the lensed one. Both have been scaled by $f_{\rm sky}^{\rm eff}$, the effective fractional sky coverage (see text). The gray filled and open circles labeled "Tophat", represent, respectively, the theoretical unlensed and lensed power spectra convolved with a window function that is unity inside the polar cap and zero outside. The black filled and open circles represent the same quantities, but in the case of a window which is apodized at the edge of the polar cap, as discussed in the text. Aliasing of power to higher multipoles due to mode coupling is significantly reduced in the latter case. We use the apodized window to mask the polar cap maps for computing various power spectra, and use the corresponding theory power spectrum convolved with the same window for comparing our results with theory. (*Inset:* The mode coupling matrix $M_{\ell_1\ell_2}$ as a function of ℓ_1, for $\ell_2 = 3000$, showing the reduction in the power in off-diagonal elements as a result of apodization.) 33

1.5 The Polar Cap map obtained after subtracting the unlensed CMB map from the lensed CMB map. To enhance the contrast, we have remapped the color scale to the range $(-2\sigma, 2\sigma)$, σ being the standard deviation of the map. . 34

1.6 The lensed and unlensed CMB angular power spectra obtained from the simulation compared with the theoretical models. The red and orange dots represent, respectively, the lensed and unlensed angular power spectra obtained from the polar cap using the methods described in §1.4. The solid black curve signifies the theoretical unlensed power spectrum taking into account the mode coupling due to the apodized polar cap window function. The blue solid curve represents the same for the lensed power spectrum. . . 35

1.7 Lensed CMB angular power spectrum in the multipole range $500 < \ell < 3500$ obtained from the simulation compared with the theoretical model. The red dots represent the lensed angular power spectrum obtained from the polar cap using the methods described in §1.4. The solid black curve signifies the theoretical lensed CMB power spectrum taking into account the mode coupling due to the apodized polar cap window function. The dotted black curve represents the same for the theoretical unlensed power spectrum and is shown here for contrast to the lensed case. 36

1.8 The mass in the lensing-slices compared with that expected from theory. . . 37

1.9 The probability density function (PDF) of the surface mass density in the lensing-planes (circles) compared with the lognormal (dashed line) and the Das & Ostriker (2006) model (solid line). 38

1.10 Power spectrum of the effective convergence map $\mathbf{M}_1$ produced from the simulated lensing planes alone. The red line shows the power spectrum computed from the convergence map and the black solid line represents the theoretical power spectrum with non-linear corrections. The power spectrum is corrected for the shot noise contribution (see text) which is displayed as the dotted line. The black dashed line corresponds to the linear theory power spectrum. All theory power spectra are mode-coupled with the apodizing window. 39

1.11 Power spectrum of the effective convergence map ($\mathbf{M}_1 + \mathbf{M}_2$) after adding in high redshift contribution. The red line shows the power spectrum computed from the convergence map and the black solid line represents the theoretical power spectrum with non-linear corrections. The power spectrum is corrected for the shot noise contribution (see text) which is displayed as the dotted line. The black dashed line corresponds to the linear theory power spectrum. All theory power spectra are mode-coupled with the apodizing window. 40
1.12 Difference between the simulated and the theoretical binned power spectrum for lensed CMB. 41

2.1 Eigenvalues corresponding the different orders of DPSS tapers. Two cases with $NW = 3$ and 6 are shown for $N = 50$. Spectral concentration of the tapers rapidly worsen beyond $\alpha = 2NW - 1$. 54
2.2 Examples of DPSS tapers and the corresponding spectral window functions for the case $N = 50$ and $NW = 6$. *Upper panel:* Real space form of the tapers of orders 0, 4, 6 and 8. *Lower panel:* The spectral window functions corresponding to the tapers in the upper panel. For simplicity, the window functions are shown only in the range $-3W < f < 3W$ of frequency. The vertical dotted lines denote the edges of the bandwidth $(-W, W)$ within which the tapers are designed to be optimally concentrated. Tapers are ordered such that spectral leakage progressively increases for tapers of higher order. . . 55
2.3 *Top panel*: The first 4 two-dimensional tapers on a N×N grid with $N = 50$ and $NW = 5$. The order of the one-dimensional tapers corresponding to each taper is indicated on the top. *Bottom panel*: The logarithm of the spectral window functions $\Gamma(k^1, k^2)$, corresponding to the tapers on the upper panel. The color scale on the lower panel are standardized to be $(10^{-30}, 1)$ times the maximum in each plot. The white dotted lines represent the location of $\pm 2\pi W$ wavenumbers. 59

2.4 One realization of the CMB map on a 192×192 pixel grid. The physical size is 8 degrees on a side. Estimation of the power spectrum is done on the 4 degree $\times$ 4 degree subarea indicated by the rectangle. The color scale represents temperature fluctuations in micro-Kelvin. 63

2.5 Comparison of the simple periodogram method (labeled PM), the eigenvalue weighted multitaper (labeled MTM) and the adaptive multitaper (labeled AMTM) methods for estimating the power spectrum of a CMB map. In each plot, the continuous line represents the theory power spectrum used as an input for the Monte Carlo simulations. The open circles represent the mean values in each ℓ bin, averaged over 5000 realizations, while the vertical lines represent the 2σ spread. The bin width for this figure was $\Delta\ell = 180$. For the MTM and AMTM methods $N_{tap} = 3^2$ tapers with $N_{res} = 2$ were used (see text for details). Note that the power spectra for the multitaper methods appear smoothed because they are convolved with the window function of an effective taper. Standard decorrelation techniques, like the MASTER algorithm (Hivon et al., 2002) can be employed to de-bias and deconvolve all the above power spectra, but in the first two cases, where the mode-coupled power spectra are biased, decorrelation leads to bigger uncertainties in the deconvolved power spectra (see § 2.5). 64

2.6 Comparison of the probability distributions of the estimated power spectrum at three points (pixels) in the two-dimensional Fourier ($\boldsymbol{\ell}$) space. From left to right, these points are $(\ell^1, \ell^2) = (630, 630)$, $(1980, 630)$ and $(2880, 630)$, for which the modulus ℓ has been indicated in each figure. *Upper Panel:* Power spectrum estimation with $N_{res} = 2.0$ and $N_{tap} = 3^2$. The open circles (black), the diamonds (red) and the triangles (green) indicate the probability distribution of the quantity $\ell(\ell + 1)C_\ell/(2\pi)$ as estimated via the AMTM, MTM and PM methods from 5000 Monte Carlo simulations, respectively. The respective approximate theoretical forms as discussed in § 2.2.5 are overplotted as the continuous curve (black), the dotted curve (red) and the dashed curve (green) for each of the methods. The mean degree of freedom of the chi-square for each method is also indicated as ν_A for AMTM, ν_M for MTM and ν_P for the periodogram, PM. Each curve is also accompanied by a vertical line of the same style (and color) representing the mean value obtained from the Monte Carlo simulations. In each figure, the continuous (black) vertical line corresponding to the mean of the AMTM method, is also the value closest to the true power spectrum. It is actually the unbiased value of the pseudo power spectrum (see § 2.5). *Lower Panel:* Same as above but with $N_{res} = 3.0$ and $Ntap = 5^2$. 68

2.7 Comparison of the probability distributions of the estimated power spectrum in bins. Each panel is for a different combination of the N_{res} and N_{tap} as indicated on the top of the middle figure. The open circles (black), the diamonds (red) and the triangles (green) indicate the probability distribution of the quantity $\ell(\ell+1)C_\ell/(2\pi)$ in each bin as estimated via the AMTM, MTM and PM methods from 5000 Monte Carlo simulations, respectively. The respective approximate theoretical forms as discussed in § 2.2.5 (see eq. equation (2.37)) are over-plotted as the continuous curve (black), the dotted curve (red) and the dashed curve (green) for each of the methods. The mean degree of freedom of the chi-square for each method is also indicated as ν_A for AMTM, ν_M for MTM and ν_P for the periodogram, PM. The number of pixels in each bin is also indicated as N_b. Note that the periodogram is absent in each of the rightmost plots, as it is highly biased and lies outside the range plotted. 69

2.8 Covariance matrix of the bandpowers estimated via AMTM for three different parameter settings; from left to right these are: $N_{res} = 2.0, \quad N_{tap} = 3$; $N_{res} = 3.0, \quad N_{tap} = 5$ and $N_{res} = 4.0, \quad N_{tap} = 4$. Each square in the image represents a bin in ℓ. For the $N_{res} = 2.0$ and $N_{res} = 3.0$ cases, we chose the bin-widths to be twice the fundamental resolution element, i.e. $\Delta\ell = 2\ell_{fund} = 180$, while for the $N_{res} = 4.0$ case it was taken to be $4\ell_{fund} = 360$. There is appreciable covariance only between bins inside the resolution $\Delta\ell_W = 2\ N_{res}\ \ell_{fund}$ set by the taper, and the covariance drops drastically beyond that frequency. 70

2.9 "Disc-difference" function W_{R-3R} discussed in the text (solid line). The dashed line represents the function x^4. 75

2.10 Effect of disc-differencing and self-injection on the power spectrum. The dotted line is the true power spectrum with a large dynamic range. The disc-differencing operation alone produces the dashed curve which has a much smaller dynamic range, but is steeply rising at low multipoles. The disc radius used is $R = 1'$. The dot-dashed curve shows the true power spectrum multiplied by a constant α^2 where $\alpha = 0.02$. If we disc-difference the map followed by self-injection of a fraction α of the map, then the power spectrum of the processed map is the solid curve (given by equation (2.51)) which is conveniently flat over the range of multipoles. 76

2.11 Prewhitening and AMTM as a remedy to aliasing of power due to point source mask. The dotted curve represents the input power spectrum from which the map is generated. The triangles represent the recovered AMTM power spectrum ($N_{res} = 3.0$, $N_{tap} = 3^2$) of the map after a point source mask is applied directly to it. If, on the other hand, the map is first prewhitened (see text) and the mask is subsequently applied, one obtains the diamonds as the AMTM power spectrum. The solid curve is the theoretical prediction for the prewhitened power spectrum. Thereafter, one divides the spectrum by the prewhitening transfer function (see equation (2.51), obtaining a nearly unbiased estimate, denoted by the open circles. Note that the AMTM power spectra appear smoother than the true spectra as the former is convolved with the window function of the taper. 78

2.12 Same as in Fig. 2.11, but for a map with white noise. In addition to the standard prewhitening operation, a Gaussian smoothing has been applied to flatten the tail of the prewhitened map. 80

2.13 Deconvolution of the power spectrum. *Left panel*: Deconvolution of the periodogram with top-hat weighting. The black squares represent the binned power spectrum obtained directly from the map using the periodogram (straight FFT) method. As discussed in the text, this power spectrum is the true power spectrum convolved with the mode-mode coupling matrix due to the top-hat, the theoretical expectation for which is displayed as the blue line. The red points represent the binned power spectrum deconvolved via equation (2.60). The black line is the input power spectrum. The deconvolved binned power spectrum is to be compared with the binned input power spectrum which is displayed as the black histogram. All points displayed are the mean of 800 Monte Carlo simulations and the error bars correspond to the 2σ spread in their values. *Right Panel:* Same as above, but for the AMTM method. The mode-coupled power spectrum and the corresponding theoretical curve in this case have been artificially shifted below the deconvolved power spectra for easy viewing. As discussed in the text, the mode-coupled power spectrum produced by the AMTM method is a nearly unbiased estimate of the true power spectrum, while the mode-coupled periodogram (left panel) is highly biased at large multipoles. This bias causes the error bars in the deconvolved periodogram to be much larger than those in the deconvolved AMTM power spectrum at large ℓ, as shown in Fig. 2.14. 81

2.14 Fractional errors in the deconvolved binned power spectrum. The open circles represent the fractional errors for the periodogram method (left panel of Fig. 2.13). The filled circles represent the same for the AMTM method (right panel of Fig. 2.13). Although the deconvolved power spectrum obtained from either method is an unbiased estimate of the true power spectrum, the errors from the periodogram method are much larger at high ℓ because of the highly biased nature of the mode-coupled periodogram at those multipoles. 83

2.15 Effect of prewhitening on the errors in the deconvolved power spectrum in presence of a point source mask. *Top Panel:* For the AMTM method: The open circles represent the fractional 1σ error bars on the deconvolved power spectrum when prewhitening is not performed, showing that holes in the point source mask render the AMTM method biased at high multipoles and lead to large error bars. The filled circles represent the same after prewhitening has been performed, showing that prewhitening remedies the leakage of power and makes the power spectrum estimator nearly unbiased. *Bottom Panel:* The same as above, but for the periodogram or straight FFT. Note that prewhitening, if performed properly, makes the periodogram as good a power spectrum tool as the AMTM. 87

3.1 Cross power spectra, the ratio of which is being studied (cf. equation 3.8). Also shown are predicted 1σ errors in uniform bins of size $\Delta\ell = 30$. For the $C_\ell^{\Sigma\kappa_{\rm CMB}}$ case, the outer (lighter) errors correspond to lensing reconstruction using temperature and polarization with Planck, while the inner (darker) ones correspond to the same for CMBPOL. 104

3.2 Various power spectra that enter the calculation of the error on the lensing ratio (cf. eq. 3.13). Each of the noise power spectra has been plotted with the same line style as its corresponding signal power spectrum and labeled as N_ℓ. The noise spectrum for the CMB lensing reconstruction has been indicated both for Planck and CMBPOL. 107

3.3 *Left Panel*: Improvements of constrains in the $\Omega_k - \Omega_\Lambda$ plane for a vacuum energy model with Planck by adding a 1% measurement of the lensing-ratio. The outer solid contour is the 68% confidence interval from primary CMB alone while the inner solid contour is the same after adding the lensing-ratio. The dotted contours have the same interpretation but represent the case where information from lensing extraction has been added to the CMB Fisher matrix. *Right Panel:* Same as left, but for the $w - \Omega_\Lambda$ plane, assuming flatness. 108

3.4 Improvements in the constraints on the interesting subset of parameters in the eleven parameter model involving massive neutrinos and free dark-energy equation of state (see text). The interpretations of the contours are same as in Fig. 3.3 110

3.5 Constraints (68%) in the w-Ω_k plane from BAO and lensing-ratio measurements. The dashed line indicate constraints from the lensing-ratio while the dotted line represents the same for the BAO ratio. The solid contour shows the joint constraint. Regions outside the contours labeled "excluded" are not allowed due to the strong CMB prior (see text). 111

3.A.1 *Left:* Comoving angular diameter distance at the high redshift end for various models. The solid curve corresponds to the fiducial early dark energy model with $\Omega_d^0 = 0.742$, $w_0 = -1$ and $\Omega_d^e = 0.03$. The horizontal line indicates the value of $d_A(z_0)$ at the last scattering surface required by a wrong model with $\Omega_d^e = 0$, to keep the CMB angular scale, θ_A, constant. The dotted line represents a model with all parameters kept same as the fiducial model, except Ω_d^e which is set to zero. This falls short of the required $d_A(z_0)$ and hence the only free parameter in the model, Ω_d^0, has to be adjusted to achieve the required $d_A(z_0)$. The final model that would be wrongly inferred by matching the CMB acoustic scale, has $\Omega_d^0 = 0.735$ and is shown by the dashed line. *Right:* Fractional difference in the comoving angular diameter distance $d_A(z)$ from the fiducial model. The dotted line represents the fractional error for the same model as shown by the dotted line on the left plot. As expected the difference in this case goes to zero at low redshift. The dashed line shows fractional difference in the wrongly inferred model. Note that since this model had its Ω_d^0 shifted low, it overestimates the true distances by $\sim 1.5\%$ for $z \gtrsim 1$ and by 1.3% for $z \lesssim 0.5$. 114

3.A.2 *Left:* Fractional difference from the fiducial of the Hubble scale $c/H(z)$ in the wrongly inferred model of Fig. 3.A.1. *Right:* Same as left, for the lensing ratio as a function of the lens redshift. 116

4.1 Various terms that enter the calculation of the signal to noise equation (4.12). The solid curve represents the CMB power spectrum C_ℓ, while the dot-dashed curve represents the instrumental noise for the assumed experimental specifications (see text) and for an exposure time of 16 minutes. The upper (lower) dotted curve represents S_ℓ for the void with $\delta = -1$ ($\delta = -0.3$). The dashed line represents S_ℓ for the texture. 127

4.2 Signal to noise for the detection of the lensing template by the experiment described in the text, as a function of the time of exposure of an 8° square region centered on the Cold Spot. The upper (lower) dotted line corresponds to the case for the void with $\delta = -1$ ($\delta = -0.3$). The dashed line represent the case for the cosmic texture. 129

A.1 The behavior of $\epsilon(k, a) = \Omega_m^{-\gamma} d\ln D/d\ln a - 1$ in GR (solid line) and in $f(R)$ models, as a function of B_0 and k. Growth is enhanced for $B_0 \neq 0$ and at smaller scales in alternative theories. In GR, $\epsilon(a) = 0$. 140

A.2 Errors on $P(k)$, normalized to the SDSS-LRG median redshift (z=0.31) for all surveys. 143

A.3 $\epsilon(k, z)$ for the four surveys, as a factor of B_0 and k. Total errorbars around the ΛCDM case are shown in black; the smaller red errorbars are from bias only. 145

List of Tables

3.1 Predictions for the cross-correlation studies described in the text with foreground galaxies from ADEPT, background galaxies from LSST and different CMB experiments. The quantity $(S/N)^{cross}$ represents the signal-to-noise ratio in the estimation of the cross correlation between the foreground tracer density with CMB lensing. The last column shows percentage error in the lensing-ratio estimator, r of equation (3.8). We show the prediction for both temperature based (TT) and polarization based (POL) reconstruction of the deflection field from the lensed CMB. 106

A.1 Predictions for the errors on bias from the cross-correlation studies described in the text. For each combination of experiments, we display the number of galaxies per square degree ($\bar{n}$); the area of overlap (A), the signal-to-noise with which the cross correlation of tracer surface density with CMB-lensing can be extracted, (S/N), and the percentage error in the bias, b, for the tracer. 144

A.2 Currently available data for measurements of ϵ through β and b (from Nesseris & Perivolaropoulos (2008), with the addition of the measurement reported in Guzzo et al. (2008)), and comparison with our predictions. Only the error coming from uncertainties in β and b is considered. 147

Chapter 1

A Large Sky Simulation of the Gravitational Lensing of the Cosmic Microwave Background

Abstract

Large scale structure deflects cosmic microwave background (CMB) photons. Since large angular scales in the large scale structure contribute significantly to the gravitational lensing effect, a realistic simulation of CMB lensing requires a sufficiently large sky area. We describe simulations that include these effects, and present both effective and multiple plane ray-tracing versions of the algorithm, which employs spherical harmonic space and does not use the flat sky approximation. We simulate lensed CMB maps with an angular resolution of $\sim 0.'9$. The angular power spectrum of the simulated sky agrees well with analytical predictions. Maps generated in this manner are a useful tool for the analysis and interpretation of upcoming CMB experiments such as PLANCK and ACT.

1.1 Introduction

While the current generation of CMB experiments have had a significant impact on cosmology by helping to establish a standard paradigm for cosmology (Spergel et al., 2003, 2007), the upcoming generation of CMB experiments still has the potential to provide novel new insights into cosmology. PLANCK[1] and ground based experiments, such as the Atacama Cosmology Telescope (ACT)[2] , will be mapping the CMB sky with significantly higher angular resolution than ever before. Secondary anisotropies on small angular scales encode important information about the late time interaction of CMB photons with structure in the Universe. One of the most basic of these interactions is the gravitational effect of the large scale structure potentials deflecting the paths of the photons, an effect justifiably referred to as the Gravitational Lensing of the CMB.

The effect of gravitational lensing can be thought of as a remapping of the unlensed CMB field by a line-of-sight averaged deflection field (for a recent review, see Lewis & Challinor, 2006). Therefore, lensing does not change the one-point properties of the CMB. However, it does modify the two and higher-point statistics, and generates non-Gaussianity (Seljak, 1996; Zaldarriaga & Seljak, 1999; Zaldarriaga, 2000). Although the typical deflection suffered by a CMB photon during its cosmic journey is about three arcminutes, the deflections themselves are coherent over several degrees, which is comparable to the typical size of the acoustic features on the CMB. Thus lensing causes coherent distortions of the hot and cold spots on the CMB, and thereby broadens their size distribution. This leads to redistribution of power among the acoustic scales in the CMB, and shows up in the two-point statistics as a smoothing of the acoustic peaks. At smaller scales, where the primordial CMB is well approximated by a local gradient, deflectors of small angular size produce small-scale distortions in the CMB, thereby transferring power from large scales in the CMB to the higher multipoles. Also, although the primordial CMB can be safely assumed to be a Gaussian random field (Komatsu et al., 2003), and the large scale lensing potential can also be

[1] `http://www.rssd.esa.int/index.php?project=Planck`
[2] `http://www.physics.princeton.edu/act`

well approximated by a Gaussian random field, the lensed CMB— being a reprocessing of one Gaussian random field by another— is itself not Gaussian. The effect of lensing on the power spectrum of the CMB is important enough that it should be taken into account while deriving parameter constraints with future higher resolution experiments. But what is even more interesting is that the non-Gaussianity in the lensed CMB field should enable us to extract information about the projected large scale structure potential, and thereby constrain the late time evolution of the Universe and Dark Energy properties. Therein lies the main motivation of studying this effect in utmost detail. Progress in this area has been slow. Measurements of the CMB precise enough to enable a detection of weak lensing were not available in the pre-WMAP era. Also, picking out non-Gaussian signatures in the measured CMB sky by itself is extremely difficult, due to confusion from systematics, foregrounds, and limited angular resolution.

Rather than looking at signatures of lensing only in the CMB, one can also measure to what extent the deflection field estimated from the CMB correlates with tracers of the large scale structure which contributed to the lensing. It is easily realized that this approach is powerful (Peiris & Spergel, 2000) because many of the systematics disappear upon cross-correlating data sets. This approach was taken in recent years by Hirata et al. (2004) and Smith et al. (2007), using WMAP 1-year and 3-year data respectively. The former work looked at the cross correlation with SDSS luminous red galaxies (LRG), while the latter used the NRAO-VLA Sky Survey (NVSS) radio sources as their large scale structure tracers. As the lensing efficiency for the CMB is highest between redshifts of one and four, higher redshift tracers should show greater cross correlation signal, which makes the NVSS radio sources better tracers for such study; Smith et al. (2007) report a 3.4σ detection. An independent analysis by Hirata et al. (2008) looking for this effect in the WMAP 3-year data in cross correlation with SDSS LRG+QSO and NVSS sources find this signal at the 2.5σ level. With these pioneering efforts and with higher resolution CMB data from experiments such as ACT, PLANCK and the South Pole Telescope (SPT)[3] on the horizon, we are

[3]http://spt.uchicago.edu

entering an era where robust detection and characterization of this effect will become a reality. Also, with upcoming and proposed large scale structure projects (LSST[4] , SNAP[5] , ADEPT[6] , DESTINY[7] , etc.) there will in future be many more datasets to cross-correlate with the CMB.

One of the immediate results of such cross-correlation studies will be a measurement of the bias of the tracer population. Because such cross correlations tie together early universe physics from the CMB and late time evolution from large scale structure, they will also be sensitive to Dark Energy parameters (Hu et al., 2006) and neutrino properties (Smith et al., 2006a; Lesgourgues et al., 2006), and can potentially break several parameter degeneracies in the primordial CMB (M. Santolini, S. Das and D. N. Spergel, in preparation). Combination of galaxy or cluster lensing of the CMB with shear measurements from weak lensing of galaxies can also provide important constraints on the geometry of the Universe (see Chapter 3; Hu et al., 2007). Again, with high enough precision of CMB data, it is possible to estimate, using quadratic (Okamoto & Hu, 2003) or maximum likelihood (Hirata & Seljak, 2003) estimators, the deflection field that caused the lensing. Such estimates can be turned into strong constraints of the power spectrum of the projected lensing potential (Hu & Okamoto, 2002), which is also sensitive to the details of growth of structure. The estimated potential from the lensed CMB alone, or the potential estimated from weak lensing surveys (Marian & Bernstein, 2007), can be also used to significantly de-lens the CMB. This is particularly important in the detection of primordial tensor modes via measurements of CMB polarization. This is because (even though detection of the so-called B modes in CMB polarization is hailed as the definitive indicator of the presence of gravitational waves from the inflationary era) these mode can be potentially contaminated by the conversion of E-modes into B-modes via gravitational lensing. De-lensing provides a way of cleaning these contaminating B-modes produced by lensing and thereby probing the true gravitational wave signature.

[4] `http://www.lsst.org/lsst\_home.shtml`
[5] `http://snap.lbl.gov/`
[6] `http://universe.nasa.gov/program/probes/adept.html`
[7] `http://destiny.asu.edu/`

We describe a method for simulating the gravitational lensing of the CMB temperature field on a large area of the sky using a high resolution Tree-Particle-Mesh (TPM; Bode et al., 2000; Bode & Ostriker, 2003) simulation of large scale structure to produce the lensing potential. The reason for considering a large area of the sky is twofold. First, the deflection field has most of its power on large scales (the power spectrum of the deflection field peaks at $\ell \sim 50$ in the best-fit cosmological model), and much of the power redistribution in the acoustic peaks of the CMB occurs via coupling of modes in the CMB with these large coherent modes in the deflection field. A large sky allows for several such modes to be realized. It is estimated that a small (flat) sky simulation that misses these modes would typically underestimate the lensing effect by about 10% in the acoustic regime, and more in the damping tail (Hu, 2000). Second, one of the major goals of simulations such as this is to produce mock observations for upcoming CMB experiments. PLANCK is an all-sky experiment, and many of the future CMB experiments (including ACT and SPT) will observe relatively large patches of the sky. Therefore, simulating CMB fields on a large area of the sky is a necessity. This method fully takes into account the curvature of the sky. Although presented here for a polar cap like area, it can be trivially extended to the full sky.

The value of a simulation as described here is multifaceted, particularly in the development of algorithms for detection and characterization of the CMB lensing effect for a specific experiment. Since each experiment has a unique scanning mode, beam pattern, area coverage, and foregrounds, operations and optimizations performed on the data to extract the lensing information will have to be tailored to the specific experiment. A large-sky lensed CMB map acting as an input for a telescope simulator provides the flexibility of exploring various observing strategies, and also allows for superposition of known foregrounds. Another important aspect of this simulation is that the halos identified in the large scale structure simulation can be populated with different tracers of interest. Also, other signals, such as the Thermal and Kinetic Sunyaev Zel'dovich effects and weak lensing of galaxies by large scale structure, can be simulated using the same large scale structure.

This opens up the possibility of studying the cross-correlation of the CMB lensing signal with various indicators of mass, and thereby predicting the level of scientific impact that a specific combination of experiments can have.

As noted in Lewis (2005), the exact simulation of the lensed CMB sky, which requires the computation of spin spherical harmonics on an irregular grid defined by the original positions of the photons on the CMB surface, is computationally expensive and requires robust parallelization. Lewis (2005) suggested an alternative in which one would resample an unlensed CMB sky, generated with finer pixelation, at these unlensed positions. This method was implemented in the publicly available LensPix[8] code that was based on Lewis (2005). However, producing a high resolution lensed map requires a much higher resolution unlensed map, the generation of which becomes computationally more expensive as resolution increases. Here we put forward another alternative, in which we do the resampling with a combination of fast spherical harmonic transform on a regular grid followed by a high order polynomial interpolation. This interpolation scheme has been adapted from Hirata et al. (2004), and is called the Non-Isolatitude Spherical Harmonic Transform (NISHT). This method is accurate as well as fast, and does not require parallelization or production of maps at a higher resolution. Another added advantage of this method is that the same algorithm can be used to generate the gradient of a scalar field on an irregular grid. Since the deflection field is a gradient of the lensing potential, this opens up the possibility of performing a multiple plane ray tracing simulation. This is because the rays, as they propagate from one plane to another, end up on irregular grids, so the deflection fields on the subsequent planes have to be evaluated on irregular grids. At the time of the development of this project, LensPix did not include an interpolation scheme, and used the methods as described originally in that paper. Concurrently with the completing of the current work, an interpolation scheme (Akima, 1996) different from the one described here has been added to that code. Another notable difference of our results with LensPix, is that while the latter uses a Gaussian Random realization of the deflection field, we have used a large scale

[8]http://cosmologist.info/lenspix

structure simulation to produce the same, thereby including all higher order correlations due to non-linearities.

The chapter is laid out as follows. In §1.2 we explain the lensing algorithm, describing the governing equations in §1.2.1 and their discretization in §1.2.2. Then we discuss the effective lensing approach (§1.2.3) as well as the multiple plane ray tracing approach (§1.2.4). At the heart of the lensing algorithm lies the non-isolatitude spherical harmonic transform algorithm adapted from Hirata et al. (2004), which is reproduced in some detail for completeness in §1.2.5. As discussed earlier, we have employed a light cone N-body simulation and adopted a special polar cap like geometry for generating the lensing planes (§1.3). For comparison of the simulated fields with theoretical prediction, we compute the angular power spectra on the polar cap window; in §1.4 we describe some of the subtleties involved in computing the power spectra. We present our results in §1.5 and describe the tests that we have performed in §1.6. Conclusions are presented in §1.7.

1.2 The Lensing Algorithm

1.2.1 Basic Equations

We would like to note here that while the calculations for the simulation described here have been done for a flat universe, our approach is generalizable to non-flat geometries.

The deflection angle of a light ray propagating through the space is

$$d\boldsymbol{\alpha} = -2\nabla_{\perp}\Psi d\eta, \tag{1.1}$$

where is $d\boldsymbol{\alpha}$ is the deflection angle, Ψ is the Newtonian potential, $\nabla_{\perp}$ denotes the spatial gradient on a plane perpendicular to light propagation direction and η is the radial comoving distance. The transverse shift of the light ray position at η due to a deflection at η' is given by

$$d\mathbf{x}(\eta) = d_A(\eta - \eta')d\boldsymbol{\alpha}(\eta'), \tag{1.2}$$

where $d_A(\eta)$ is the comoving angular diameter distance.

The final angular position $\boldsymbol{\theta}(\eta) = \mathbf{x}(\eta)/d_A(\eta)$ is therefore given by

$$\begin{aligned} \boldsymbol{\theta}(\eta) &= \boldsymbol{\theta}(0) - \frac{2}{d_A(\eta)} \int_0^\eta d\eta' d_A(\eta - \eta') \nabla_\perp \Psi \\ &= \boldsymbol{\theta}(0) + \tilde{\boldsymbol{\alpha}}(\eta), \end{aligned} \tag{1.3}$$

where $\tilde{\boldsymbol{\alpha}}$ is the total effective deflection.

1.2.2 Discretization

We will now discretize the above equations by dividing the radial interval between the observer and the source into N concentric shells each of comoving thickness $\Delta\eta$. We project the matter in the i-th shell onto a spherical sheet at comoving distance η_i which is halfway between the the edges of the shell (i increases as one moves away from the observer). Since we shall be working in spherical coordinates it is advantageous to use angular differential operators instead of spatial ones. We rewrite equation (1.1) in terms of the angular gradient $\nabla_{\hat{\mathbf{n}}}$ as

$$d\boldsymbol{\alpha} = -\frac{2}{d_A(\eta)} \nabla_{\hat{\mathbf{n}}} \Psi d\eta. \tag{1.4}$$

At the j-th shell at η_j, the deflection angle due to the matter in the shell can be approximated by an integral of the above:

$$\boldsymbol{\alpha}^j = -\frac{2}{d_A(\eta_j)} \int_{\eta_j - \Delta\eta/2}^{\eta_j + \Delta\eta/2} \nabla_{\hat{\mathbf{n}}} \Psi(\tilde{\eta}\hat{\mathbf{n}}; \tilde{\eta}) d\tilde{\eta} \tag{1.5}$$

$$= -\nabla_{\hat{\mathbf{n}}} \phi^j(\hat{\mathbf{n}}), \tag{1.6}$$

where we have defined the 2-D potential on the sphere as

$$\phi^j(\hat{\mathbf{n}}) = \frac{2}{d_A(\eta_j)} \int_{\eta_j - \Delta\eta/2}^{\eta_j + \Delta\eta/2} \Psi(\tilde{\eta}\hat{\mathbf{n}}; \tilde{\eta}) d\tilde{\eta}. \tag{1.7}$$

Here, the notation $(\eta\hat{\mathbf{n}}; \eta)$ signifies that the potential is evaluated at the conformal look-back time η, when the photon was at the position $\eta\hat{\mathbf{n}}$. The potential can be related to the mass overdensity in the shell via Poisson's equation, which reads

$$\nabla_\eta^2 \Psi = \frac{4\pi G}{c^2} \frac{\rho - \bar{\rho}}{(1+z)^2}, \tag{1.8}$$

$\bar{\rho}$ being the mean matter density of the universe at redshift z. By integrating the above equation along the line of sight, one can arrive at a two dimensional version of the Poisson equation (Vale & White, 2003),

$$\nabla^2_{\hat{\mathbf{n}}}\phi^j(\hat{\mathbf{n}}) = \frac{8\pi G}{c^2}\frac{d_A(\eta_j)}{(1+z_j)^2}\Delta^j_\Sigma(\hat{\mathbf{n}}) \tag{1.9}$$

where the surface mass density

$$\Delta^j_\Sigma = \int_{\eta_j-\Delta\eta/2}^{\eta_j+\Delta\eta/2}(\rho-\bar{\rho})d\tilde{\eta}. \tag{1.10}$$

Note that in going from the three dimensional to the two dimensional version, the term containing the radial derivatives of the Laplacian can be neglected (Jain et al., 2000). One can show that this term is small by expanding the potential Ψ in Fourier modes $\mathbf{k}$, with components $k_\parallel$ parallel to the line of sight and $k_\perp$ transverse to it. Then, the ratio of the components of the line of sight integral in the parallel and transverse directions will be $\sim k^2_\parallel/k^2_\perp$. Due to cancellation along the line of sight, only the modes with wavelengths comparable to the line of sight depth of each slice will survive the radial integral. These would be the modes with $k_\parallel \lesssim \frac{2\pi}{\Delta\eta}$. On the other hand, the transverse component gets most of its contribution from scales smaller than ~ 100 Mpc i.e. $\kappa_\perp \gg 2\pi/100 \sim 0.1$ Mpc^{-1}. Under the effective lensing approximation, the projection is along the entire line of sight from zero redshift to the last scattering surface, $\Delta\eta \sim 10^4$ Mpc, giving $\kappa_\parallel \lesssim 10^{-3}$ Mpc^{-1}. Therefore, in this case the ratio of the radial and transverse components of the integral will be $\sim k^2_\parallel/k^2_\perp \ll 10^{-4}$. For a multiple plane case, we would typically employ 10 lensing planes for which this ratio would be $\ll 10^{-2}$. The approximation will break down if we employ thin shells.

Defining the field K as

$$K^j(\hat{\mathbf{n}}) = \frac{4\pi G}{c^2}\frac{d_A(\eta_j)}{(1+z_j)^2}\Delta^j_\Sigma(\hat{\mathbf{n}}), \tag{1.11}$$

equation (1.9) takes the form

$$\nabla^2_{\hat{\mathbf{n}}}\phi^j(\hat{\mathbf{n}}) = 2K^j(\hat{\mathbf{n}}). \tag{1.12}$$

It is convenient to define an angular surface mass density $\Delta_\Sigma^\theta(\hat{\mathbf{n}})$ as the mass per steradian,

$$\Delta_\Sigma^{\theta j}(\hat{\mathbf{n}}) = \int_{\eta_j-\Delta\eta/2}^{\eta_j+\Delta\eta/2} (\rho - \bar{\rho}) \frac{d_A(\tilde{\eta})^2}{(1+\tilde{z})^3} d\tilde{\eta}. \tag{1.13}$$

The surface mass density defined in equation (1.10) is related to this through the relation

$$\Delta_\Sigma = \Delta_\Sigma^\theta \frac{(1+z)^3}{d_A(\eta)^2}. \tag{1.14}$$

This implies the following form of equation (1.11),

$$K^j(\hat{\mathbf{n}}) = \frac{4\pi G}{c^2} \frac{(1+z_j)}{d_A(\eta_j)} \Delta_\Sigma^{\theta j}(\hat{\mathbf{n}}). \tag{1.15}$$

Equation (1.15) is the key equation here. The quantity K can be readily calculated once the mass density is radially projected onto the spherical sheet. Expanding both sides of equation (1.12) in spherical harmonics, one has the following relation between the components:

$$\phi_{\ell m} = \frac{2}{l(l+1)} K_{\ell m}. \tag{1.16}$$

It is interesting to note that the apparently divergent monopole ($l = 0$) modes in the lensing potential can be safely set to zero in all calculations, because a monopole term in the lensing potential does not contribute to the deflection field. Being the transverse gradient of the potential, the deflection angle $\boldsymbol{\alpha}(\hat{\mathbf{n}})$ is a vector (spin 1) field defined on the sphere and can be synthesized from the spherical harmonic components of the potential in terms of vector spherical harmonics, as will be described in § 1.2.5.

1.2.3 Connection with effective lensing quantities

In weak lensing calculations, one often takes an effective approach, in which one approximates the effect of deflectors along the entire line of sight by a projected potential or a convergence which is computed along a fiducial undeflected ray (often referred to as the Born approximation). One therefore defines an effective lensing potential out to comoving distance η_s as

$$\phi^{eff}(\hat{\mathbf{n}}) = 2 \int_0^{\eta_s} d\eta \frac{d_A(\eta_s - \eta)}{d_A(\eta) d_A(\eta_s)} \Psi(\eta\hat{\mathbf{n}}; \eta). \tag{1.17}$$

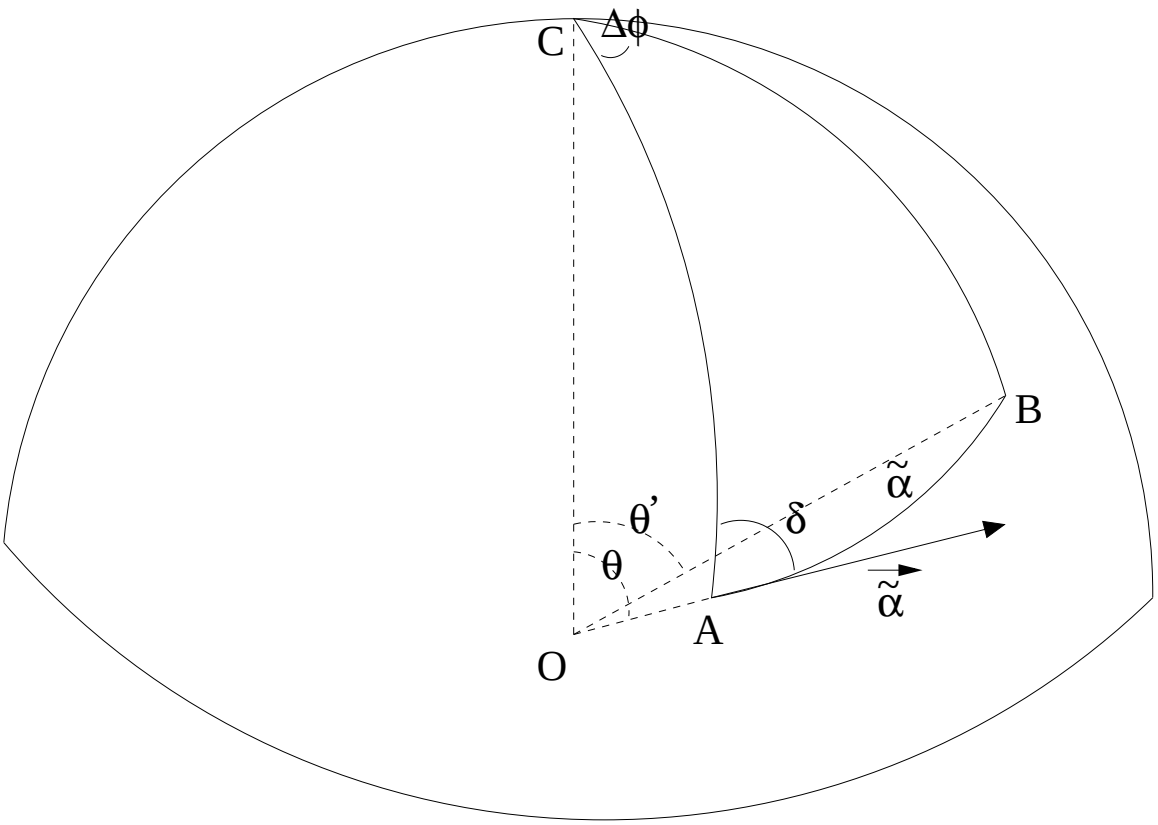

Figure 1.1: Geometry illustrating the point remapping used in the text

In terms of the projected potential, the effective deflection (see Eq. 1.3) is given by the angular gradient, $\tilde{\boldsymbol{\alpha}} = -\nabla_{\hat{\mathbf{n}}}\phi^{eff}$. An effective convergence is also defined in a similar manner:

$$\begin{aligned}\kappa(\hat{\mathbf{n}}) &= \frac{1}{2}\nabla^2_{\hat{\mathbf{n}}}\phi^{eff}(\hat{\mathbf{n}}) \\ &= \int d\eta \frac{d_A(\eta_s-\eta)d_A(\eta)}{d_A(\eta_s)}\nabla^2_{\perp}\Psi(\eta\hat{\mathbf{n}};\eta). \end{aligned} \tag{1.18}$$

In terms of the fields ϕ^j and K^j defined on the multiple planes, these quantities are immediately identified as the following sums,

$$\phi^{eff}(\hat{\mathbf{n}}) \simeq \sum_j \frac{d_A(\eta_s-\eta_j)}{d_A(\eta_s)}\phi^j(\hat{\mathbf{n}}), \tag{1.19}$$

$$\kappa(\hat{\mathbf{n}}) \simeq \sum_j \frac{d_A(\eta_s-\eta_j)}{d_A(\eta_s)}K^j(\hat{\mathbf{n}}). \tag{1.20}$$

Once κ is obtained one can go through the analog of equation (1.16) and take its transverse gradient to obtain the effective deflection $\tilde{\boldsymbol{\alpha}}$. Using this, one can find the source position corresponding to the observed position $\theta(0)$:

$$\boldsymbol{\theta}_s = \boldsymbol{\theta}(0) + \tilde{\boldsymbol{\alpha}}. \tag{1.21}$$

In §1.5, we shall use this effective or single plane approximation to lens the CMB.

Equation (1.21) is to be interpreted in the following manner (Challinor & Chon, 2002). The effective deflection angle is a tangent vector at the undeflected position of the ray. The original position of the ray on the source, or unlensed, plane is to be found by moving along a geodesic on the sphere in the direction of the tangent vector and covering a length $\tilde{\alpha}$ of an arc. The correct remapping equations can be easily derived from identities of spherical triangles (Lewis, 2005). For completeness, we give the derivation here.

In Fig. 1.1, let the initial and final position of the ray in question be the points A$\equiv(\theta,\phi)$ and B$\equiv(\theta',\phi+\Delta\phi)$, respectively. The North pole of the sphere is indicated as C, so that the dihedral angle at A is also the angle between $\tilde{\boldsymbol{\alpha}}$ and $-\mathbf{e}_\theta$, so that

$$\tilde{\boldsymbol{\alpha}} = -\tilde{\alpha}\cos\delta\mathbf{e}_\theta + \tilde{\alpha}\sin\delta\mathbf{e}_\phi. \tag{1.22}$$

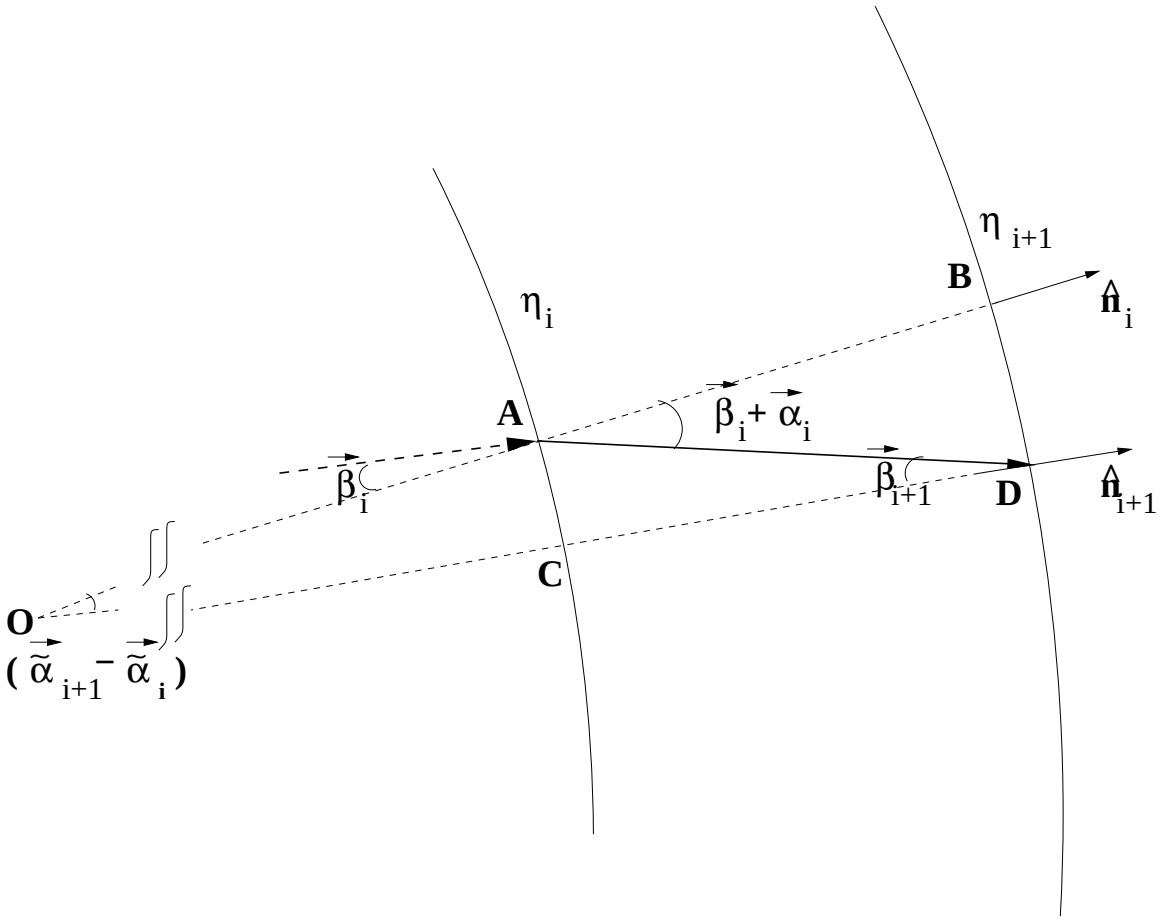

Figure 1.2: Geometry illustrating the multiple plane ray tracing method.

Now, applying the spherical cosine rule to the triangle ABC, we have

$$\cos\theta' = \cos\theta\ \cos\tilde{\alpha} + \sin\theta \sin\tilde{\alpha}\cos\delta, \tag{1.23}$$

and applying the sine rule

$$\sin\Delta\phi = \sin\tilde{\alpha}\frac{\sin\delta}{\sin\theta'}. \tag{1.24}$$

We use these equations to remap points on the CMB sky and on the intermediate spherical shells in the multiple plane case, as described below.

1.2.4 Multiple plane ray tracing

In the multiple plane case, we shoot ray outwards from the common center of the spherical shell (i.e. the observer) and follow their trajectories out to the CMB plane, thereby studying

the time reversed version of the actual phenomenon. We assume all intermediate deflections are small, as is really the case. Here we describe how we keep track of a ray propagating between multiple planes, as shown in Fig. 1.2. We assume a flat cosmology for this purpose. At some intermediate stage of the ray propagation, let a ray be incident on the i-th plane at the point A, where it gets deflected and reaches the i+1-th plane at the point D. The ray incident at A will not in general lie on the same plane as defined by the deflected ray $\vec{AD}$ and the center O of the sphere, which we also consider as the plane of the figure. Assuming that we know the incidence angle $\boldsymbol{\beta_i}$, we can obtain the additional angle of deflection $\boldsymbol{\alpha}_i$ due to the matter on plane i and compute the net deflection $\boldsymbol{\alpha}_i + \boldsymbol{\beta}_i$. Let us denote by $\tilde{\boldsymbol{\alpha}}_i$, the effective angle, by which a ray has to be remapped from its observed position $\boldsymbol{\theta}(0)$ to its current position $\boldsymbol{\theta}_i$ on plane i, so that

$$\boldsymbol{\theta}_i = \boldsymbol{\theta}(0) + \tilde{\boldsymbol{\alpha}}_i. \tag{1.25}$$

Obviously, $\tilde{\boldsymbol{\alpha}}_1 = 0$ and $\boldsymbol{\theta}_1 = \boldsymbol{\theta}(0)$. Therefore, the effective angle $(\tilde{\boldsymbol{\alpha}}_{i+1} - \tilde{\boldsymbol{\alpha}}_i)$ by which the ray has to be remapped from point B to point D on the shell i+1 can be readily calculated from two descriptions of the arc BD,

$$\eta_{i+1}(\tilde{\boldsymbol{\alpha}}_{i+1} - \tilde{\boldsymbol{\alpha}}_i) = (\eta_{i+1} - \eta_i)(\boldsymbol{\alpha}_i + \boldsymbol{\beta}_i). \tag{1.26}$$

In order to repeat this process for the (i+2)-th shell, one needs to know the value of the new incidence angle $\boldsymbol{\beta}_{i+1}$. We now equate two ways of finding the length of the arc AC,

$$\eta_i(\tilde{\boldsymbol{\alpha}}_{i+1} - \tilde{\boldsymbol{\alpha}}_i) = (\eta_{i+1} - \eta_i)\boldsymbol{\beta}_{i+1}. \tag{1.27}$$

Substituting $(\tilde{\boldsymbol{\alpha}}_{i+1} - \tilde{\boldsymbol{\alpha}}_i)$ from equation (1.26),

$$\boldsymbol{\beta}_{i+1} = \frac{\eta_i}{\eta_{i+1}}(\boldsymbol{\alpha}_i + \boldsymbol{\beta}_i). \tag{1.28}$$

Since we shoot the rays radially on the first plane, $\boldsymbol{\beta}_1 = 0$; therefore equations (1.26) and (1.28) can be used to propagate the ray back to the CMB surface, which we take to be the $(N+1)$-th plane, i.e. $\boldsymbol{\theta}_s = \boldsymbol{\theta}_{N+1}$. Although we only discuss results obtained with the effective or single plane approximation here, the multiple plane version is straightforward to perform and will be reported elsewhere.

1.2.5 Interpolation on the sphere

In practice we have used the HEALPix [9] (Gorski et al., 2005) scheme to represent fields on the sphere. At various stages of the lensing calculation, an accurate algorithm for interpolation on the sphere becomes a necessity. In the effective lensing approximation, the original positions of the rays will in general be off pixel centers. This implies that the lensed CMB field is essentially generated by sampling the unlensed CMB surface at points which are usually not pixel centers. Hence, obtaining the lensed CMB field is essentially an interpolation operation. In the case of multiple lensing planes, it is again obvious that (except for the first plane, on which we can shoot rays at pixel centers by way of convenience) the deflection field itself has to be evaluated at off-center points on all subsequent planes. So, together with the interpolation of the temperature map, we need to go between spin-0 and spin-1 fields on an arbitrary grid. Therefore, one needs, in general, a spherical harmonic transform algorithm that can deal with an irregular grid on the sphere.

For this purpose, we adopt the Non-isolatitude Spherical Harmonic Transform (NISHT) algorithm proposed by Hirata et al. (2004); details of the algorithm can be found in Appendix A of that paper. Here we have reproduced the key equations for clarity, and described the salient features of the general algorithm with special attention to aspects which are relevant for the current application.

The basic operation for generating the lensed CMB maps can be broken up into two steps:

L1. generating the deflection field on the sphere at points where the rays land from the previous plane, and

L2. sampling the unlensed CMB surface at the source-plane positions of the rays to generate the lensed CMB field.

Of course, in case of the effective lensing simulation, one can conveniently generate the deflection field at the pixel centers in step **L1** above. As step **L2** is a series of operations involving scalars and therefore conceptually simpler, we shall explain the NISHT algorithm

[9] `http://healpix.jpl.nasa.gov`

in relation to this step. Step **L1**, which involves spin-1 fields on the sphere, is conceptually similar to the spin-0 case.

The problem in step **L2** is that we know the CMB temperature field $T(\hat{\mathbf{n}})$ on the HEALPix grid $\{\hat{\mathbf{n}}\}$ as well as the source-plane positions of the rays $\{\hat{\mathbf{n}}'\}$ on the polar cap, and we want to sample the CMB field at $\{\hat{\mathbf{n}}'\}$. Suppose, by applying the steps for spherical harmonic analysis (as will be described later), we have the spherical harmonic components, $T_{\ell m}$ of the temperature field. Now, we need to synthesize the field using these $T_{\ell m}$'s at the points $\{\hat{\mathbf{n}}'\}$. This operation can be formally written as

$$T(\hat{\mathbf{n}}') = \sum_{\ell=0}^{\ell_{\max}} \sum_{m=-\ell}^{\ell} T_{\ell m} Y_{\ell m}(\hat{\mathbf{n}}'), \tag{1.29}$$

where $\ell_{\max}$ is the Nyquist multipole and is set by the resolution of the HEALPix grid as, $\ell_{\max} \simeq \pi/\sqrt{\Omega_{\rm pix}}$ (cf. equation 1.40). This synthesis operation can be split into the following four steps (Eqns. 1.30 through 1.35 are essentially reproduced for completeness from Appendix A of Hirata et al. 2004):

1. *Coarse Grid Latitude Transform*

   As the first step, we perform a transform in the latitude direction on an equally spaced set of points, $(\theta = \pi\alpha/L, \phi = 0)$, where α is an integer in the range $0 \leq \alpha \leq L$ and L is a small integral multiple of some power of two such that $L > \ell_{\max}$:

   $$T_m(\theta = \frac{\alpha}{L}\pi) = \sum_{\ell=|m|}^{\ell_{\max}} T_{\ell m} Y_{\ell m}(\theta = \frac{\alpha}{L}\pi, \phi = 0). \tag{1.30}$$

   The above calculation involves $O({\ell_{\max}}^2 L)$ operations.

2. *Refinement of Latitude Grid*

   In this step we reduce the θ grid spacing from $\frac{\alpha}{L}\pi$ to $\frac{\alpha}{L'}\pi$ where $L' > L$. We take advantage of the fact the sampling theorem can be applied to a linear combination of spherical harmonics which is band limited ($\ell \leq \ell_{\max}$) in the multipole space, and hence can be written as a Fourier sum,

   $$T_m(\theta) = \sum_{n=-\ell_{\max}}^{\ell_{\max}} C_{m,n} e^{in\theta}. \tag{1.31}$$

We determine the coefficients $C_{m,n}$ via a fast Fourier Transform (FFT) of length $2L$ and evaluate $T_m(\theta = \frac{\alpha}{L'}\pi)$ using an inverse FFT of length $2L'$. This step saves us the expensive generation of Associated Legendre Polynomials on the finer grid. Each FFT requires $O(\ell_{\rm max} L \log(L))$ operations.

3. *Projection onto Equicylindrical Grid*

   Next, we perform the standard SHT step of taking an FFT in the longitudinal direction to generate $T(\theta = \frac{\alpha}{L'}\pi, \phi = \frac{\gamma}{L'}\pi)$,

$$T(\theta = \frac{\alpha}{L'}\pi, \phi = \frac{\gamma}{L'}\pi) = \sum_{m=-\ell_{\rm max}}^{m=\ell_{\rm max}} T_m(\theta) e^{im\phi}. \tag{1.32}$$

   After this step we have synthesized the map on an Equicylindrical projection (ECP) grid. The operation count for this step is $O(L'^2 \log L')$ and the total operation count including this step is $O({\ell_{\rm max}}^3)$.

4. *Interpolation onto the final grid*

   In the final step, given a required position $\hat{\mathbf{n}}'$, we find the nearest grid point in the ECP grid and determine the fractional offset, $(\delta\alpha, \delta\gamma)$ between the two points,

$$\alpha + \delta\alpha = L'\frac{\theta}{\pi};\ \gamma + \delta\gamma = L'\frac{\phi}{\pi}. \tag{1.33}$$

   Then we perform a two dimensional polynomial interpolation using $(2K)^2$ points around the nearest grid point, obtaining the value at the required point as

$$T \simeq \sum_{\mu=-K+1}^{K} w_\mu(\delta_\alpha) \sum_{\nu=-K+1}^{K} w_\nu(\delta_\gamma) T(\frac{\alpha+\mu}{L'}\pi, \frac{\gamma+\nu}{L'}\pi), \tag{1.34}$$

   with the weights computed using Lagrange's interpolation formula,

$$w_\rho(\delta) = \frac{(-1)^{K-\rho}}{(K-\rho)!(K-1+\rho)!(\delta-\rho)} \prod_{\sigma=-K+1}^{K} (\delta - \sigma). \tag{1.35}$$

The inverse of the synthesis operation described above is the analysis operation, in which the spherical harmonic coefficients of a map defined on an irregular grid is needed. This can be thought of as the transpose of the above operations applied in reverse, and hence can be accomplished in an equal number of steps.

The above algorithm can be easily extended to deal with vector and tensor fields on the sphere. For a vector (spin 1) field, the natural basis of expansion are the vector spherical harmonics,

$$\begin{aligned} \mathbf{Y}^V_{\ell m} &= \frac{1}{\sqrt{\ell(\ell+1)}}\nabla Y_{\ell m} \\ \mathbf{Y}^A_{\ell m} &= \frac{1}{\sqrt{\ell(\ell+1)}}\hat{\mathbf{n}}\times\nabla Y_{\ell m}, \end{aligned} \tag{1.36}$$

where the superscripts V and A represent the "vector-like" and the "axial-vector-like" components, respectively. In terms of these a vector field $\mathbf{v}(\hat{\mathbf{n}})$ can be expanded as,

$$\mathbf{v}(\hat{\mathbf{n}}) = \sum_{\ell=0}^{\ell_{\rm max}}\sum_{m=-\ell}^{\ell} V_{\ell m}\mathbf{Y}^V_{\ell m}(\hat{\mathbf{n}}) + A_{\ell m}\mathbf{Y}^A_{\ell m}(\hat{\mathbf{n}}). \tag{1.37}$$

Therefore, given the $(V_{\ell m}, A_{\ell m})$ components one can go through the analogs of the above steps for the scalar field synthesis. In fact, to accomplish step **L1** of the lensing algorithm, we go from the convergence field K to the deflection field,

$$\begin{aligned} \boldsymbol{\alpha} = -\nabla\phi &= -\sum_{\ell=0}^{\ell_{\rm max}}\sum_{m=-\ell}^{\ell}\phi_{\ell m}\nabla Y_{\ell m} \\ &= -\sum_{\ell=0}^{\ell_{\rm max}}\sum_{m=-\ell}^{\ell}\frac{2}{\ell(\ell+1)}K_{\ell m}\nabla Y_{\ell m} \\ &= -\sum_{\ell=0}^{\ell_{\rm max}}\sum_{m=-\ell}^{\ell}\frac{2}{\sqrt{\ell(\ell+1)}}K_{\ell m}\mathbf{Y}^V_{\ell m}. \end{aligned} \tag{1.38}$$

Therefore, we go from the K field on the polar cap to the spherical harmonic components $K_{\ell m}$ using the analysis algorithm for scalar fields; then we divide the result by $\sqrt{\ell(\ell+1)}/2$. This defines the vector field harmonic components as $(V_{\ell m}, A_{\ell m}) = (-2K_{\ell m}/\sqrt{\ell(\ell+1)}, 0)$ from which we synthesize the deflection field at the required points.

The accuracy of the interpolation can be controlled by two parameters: the rate at which the finer grid oversamples the field i.e. the ratio $L'/\ell_{\rm max}$, and the order of the polynomial K used for the interpolation. Increasing either of these increases the accuracy. In this paper we have used $L' = 4\ell_{\rm max}$ and $K = 10$, which yields a fractional interpolation accuracy per Fourier mode of $\sim 10^{-9}$.

1.3 Generation of the lensing planes

An N-body dark matter simulation was performed to generate the large scale structure; this same simulation has been discussed in Sehgal et al. (2007) and Bode et al. (2007), so we refer the reader to these papers for more details. Briefly, a spatially flat ΛCDM cosmology was used, with a total matter density parameter $\Omega_{\rm m} = 0.26$ and vacuum energy density $\Omega_\Lambda = 0.74$. The scalar spectral index of the primordial power spectrum was set to $n_s = 0.95$ and the linear amplitude normalized to $\sigma_8 = 0.77$. The present day value of the Hubble parameter $H_0 = 72\,{\rm kms}^{-1}{\rm Mpc}^{-1}$. A periodic box of size $L = 1000\,h^{-1}$Mpc was used with $N = 1024^3$ particles; therefore the particle mass was $m_p = 6.72 \times 10^{10} h^{-1} M_\odot$. The cubic spline softening length was set to 16.28 h^{-1}Mpc.

1.3.1 From the box to the sphere

We create the lensing planes on-the-fly from the N-body simulation. At each large time step (set by a Courant condition such that no particle moves more than $\sim 122 h^{-1}$kpc in this time) the positions and velocities of the particles in a thin shell are saved. The mean radius of the shell is the comoving distance to the redshift at that time, and the width (a few h^{-1}Mpc) corresponds to the time step. Each shell is centered on the origin of the simulation and covers one octant of the sky ($x, y, z > 0$). Note that for shells with radii greater than the simulation box size, periodic copies of the box are used. Thus a given structure will appear more than once in the full light cone, albeit at different times and viewed from different angles. We then Euler rotate the coordinate axes so that the new z-axis passes through the centroid of the octant. This is done to make the centroid correspond to the North Pole on the HEALPix sphere. We use the HEALPix routine `vec2pix` to find the pixel that contains the particle's position on the sky. We then place the mass of the particle into that pixel by assigning to it the surface mass density $\Sigma_p = m_p/\Omega_{\rm pix}$, where $\Omega_{\rm pix}$ is the area of a pixel in steradians (cf. equation 1.40). Thus, if n particles fall inside the beam defined by a pixel, then the pixel ends up having a surface mass density of $n\Sigma_p$. To simplify the geometry, we save only those particles which fall inside a Polar Cap like region defined

by the disc of maximum radius that can be cut out from the octant (see Fig. 1.3).

By the end of the run, 449 such planes were produced from the simulation, spanning $z = 4.0$ to $z = 0$. As these are far too many planes for the purpose of lensing, we reduce them into ~ 50 planes by dividing up the original planes into roughly equal comoving distance bins and adding up the surface mass density pixel by pixel for all planes that fall inside a bin to yield a single plane per bin. Hereafter, we shall refer to the original planes from the TPM run as the TPM-planes and the small number of planes constructed by projecting them as the lensing-planes.

The angular radius of the Polar Cap is given by $\theta_{\rm cap} = \arccos(2/\sqrt{6})$, and the solid angle subtended by it is $\Omega_{\rm cap} = 2\pi(1 - \cos\theta_{\rm cap}) = 1.981\ {\rm sr} = 3785\ {\rm sq-deg}$. Due to pixelation, the true total area $\tilde{\Omega}_{\rm cap}$ of the $N_{\rm cap}$ pixels that make up the Polar Cap is not exactly equal to $\Omega_{\rm cap}$, but rather

$$\tilde{\Omega}_{\rm cap} = N_{\rm cap}\,\Omega_{\rm pix}\,. \tag{1.39}$$

We will denote the surface mass density in pixel p as σ_p which has units of mass per steradian.

In HEALPix , the resolution is controlled by the parameter NSIDE, which determines the number, $N_{\rm pix}$ of equal area pixels into which the entire sphere is pixelated, through the relation $N_{\rm pix} = 12 \times {\rm NSIDE}^2$, so that the area of each pixel becomes,

$$\Omega_{\rm pix} = \frac{4\pi}{N_{\rm pix}}\ {\rm steradians}. \tag{1.40}$$

The angular resolution is often expressed through the number $\theta_{\rm res} = \sqrt{\Omega_{\rm pix}}$. It is also useful to define the fraction area of the sphere covered by the polar cap as,

$$f_{\rm sky} = \frac{\tilde{\Omega}_{\rm cap}}{4\pi}. \tag{1.41}$$

For results presented in this paper the resolution parameter NSIDE was set to 4096 , which corresponds to an angular resolution of $0.'896$.

[11] http://www.jportsmouth.com/code/CMBview/cmbview.html

1.3.2 From surface density to convergence

To construct the quantities required for lensing, we first convert the surface mass density maps into surface over-density maps $\Delta\Sigma^{\theta}$ as defined in equation (1.14). It is straightforward to obtain the K-maps defined in equation (1.15) from the above map. Finally, equation (1.20) is used to obtain the effective convergence map on the Polar Cap. It is evident that the convergence map constructed out of the simulated lensing planes in this way will only contain the contribution from large scale structure up to the redshift of the farthest lensing plane ($z = 4.05$). However, to accurately lens the CMB we need to add in the contribution from higher redshifts up to the last scattering surface. We do this by generating a Gaussian random field from a theoretical power spectrum of the convergence between $z = 4.05$ and $z = z_{\rm CMB}$, computed from the matter power spectrum obtained using CAMB, and adding it onto the convergence map from the TPM simulation.

1.3.3 The unlensed CMB map

We used the `synfast` facility in HEALPix to generate the unlensed CMB map. This takes as an input a theoretical unlensed power spectrum and synthesizes a Gaussian-random realization of the unlensed CMB field. For computing the theoretical power spectrum we have used the publicly available Boltzmann transfer code CAMB[12] , with the same set of cosmological parameters as used for the large scale structure simulation.

1.4 Measuring Angular Power Spectra

At several stages we compute the power spectra of the maps to compare with theory. For example, to verify that we have created the convergence map correctly, the angular power spectrum of the κ map is computed and compared to the theory. Also, we do the same for the lensed map on the polar cap. We use the `map2alm` facility of HEALPix to perform a spherical harmonic decomposition of a map $T(\hat{\mathbf{n}})$ on the Polar Cap. The resulting spherical

[12] `http://www.camb.info`

harmonic components, i.e. $\tilde{T}^{\rm pix}_{\ell m}$'s, are then combined to obtain the pseudo-power spectrum,

$$\tilde{C_\ell}^{\rm pix} = \frac{1}{2\ell+1}\sum_{m=-\ell}^{\ell}\left|\tilde{T}^{\rm pix}_{\ell m}\right|^2. \tag{1.42}$$

There are two effects that need to be taken into account before comparing the above result with theory, namely the finite pixel size, signified by the superscript, "pix" and the incomplete sky coverage, represented by the tilde.

To simplify the following discussion of pixelation effects, for the moment we shall ignore the effect of the incomplete sky coverage. Also, we shall use the shorthand notation $\Sigma_{\ell m}$ to denote the sum $\sum_{\ell=0}^{\infty}\sum_{m=-\ell}^{\ell}$. Due to the finite pixel size, a field realized on the HEALPix sphere is a smoothed version of the true underlying field, i.e. the value of the field in pixel i is given by

$$T^{{\rm pix}(i)} = \int d^2\hat{\mathbf{n}} w^{(i)}(\hat{\mathbf{n}}) T(\hat{\mathbf{n}}), \tag{1.43}$$

where $w^{(i)}$ is the window function of the i-th pixel as is given by

$$w^{(i)}(\hat{\mathbf{n}}) = \begin{cases} \Omega_{\rm pix}^{-1} & \text{inside pixel } i \\ 0 & \text{elsewhere.} \end{cases} \tag{1.44}$$

Expanding the true field T in terms of spherical harmonics as

$$T(\hat{\mathbf{n}}) = \sum_{\ell m} T_{\ell m} Y_{\ell m}(\hat{\mathbf{n}}),$$

we have

$$T^{{\rm pix}(i)} = \sum_{\ell m} w^{(i)}_{\ell m} T_{\ell m}, \tag{1.45}$$

where

$$w^{(i)}_{\ell m} = \int d^2\hat{\mathbf{n}} w^{(i)}(\hat{\mathbf{n}}) Y_{\ell m}(\hat{\mathbf{n}}) \tag{1.46}$$

is the spherical harmonic transform of the pixel window function. In the HEALPix scheme, due to the azimuthal variation of the pixel shapes over the sky, especially in the polar cap area, a complete analysis would require the computation of these coefficients for each and every pixel. However, even for a moderate NSIDE, this calculation becomes computationally

unfeasible. Therefore, it is customary to ignore the azimuthal variation and rewrite equation (1.46) as

$$w_{\ell m}^{(i)} = w_{\ell}^{(i)} Y_{\ell m}(\hat{\mathbf{n}}_i), \tag{1.47}$$

where one defines an azimuthally averaged window function

$$w_{\ell}^{(i)} = \frac{4\pi}{(2\ell+1)} \left[\sum_{m=-\ell}^{\ell} |w_{\ell m}|^2 \right]^{1/2}. \tag{1.48}$$

From equations (1.47) and (1.45) it immediately follows that the estimate of the power spectrum of the pixelated field is given by

$$C_{\ell}^{\rm pix} = w_{\ell}^2 \left\langle T_{\ell m} T_{\ell m}^* \right\rangle = w_{\ell}^2 C_{\ell} \tag{1.49}$$

where one defines the pixel averaged window function,

$$w_{\ell} = \left(\frac{1}{N_{\rm pix}} \sum_{i=0}^{N_{\rm pix}-1} (w_{\ell}^{(i)})^2 \right)^{1/2}. \tag{1.50}$$

This function is available for $\ell < 4\times$NSIDE in the HEALPix distribution. We take out the effect of the pixel window by dividing the computed power spectrum by the square of the above function. Coming back to the case at hand, where we have both pixel and incomplete sky effects, we recover the power spectrum $\tilde{C}_{\ell}$ after correcting for the pixel window function in this manner.

The second and more important effect that one needs to take into account results from the fact that our field is defined only inside the polar cap. This is equivalent to multiplying a full sky map with a mask which has value unity inside the polar cap and zero outside. As is well known, such a mask leads to a coupling between various multipoles, leading to a power spectrum which is biased away from the true value. As this effect tends to move power across multipoles, the problem is more acute for highly colored power spectra like the CMB.

Let us denote the effective all-sky mask with W, where

$$W(\hat{\mathbf{n}}) = \begin{cases} 1 & \text{inside the polar cap,} \\ 0 & \text{elsewhere.} \end{cases} \tag{1.51}$$

The spherical harmonic components of the masked field is therefore given by

$$\tilde{T}_{\ell m} = \int d^2\hat{\mathbf{n}} T(\hat{\mathbf{n}}) W(\hat{\mathbf{n}}) Y^*_{\ell m}(\hat{\mathbf{n}}) \tag{1.52}$$

$$= \sum_{\ell' m'} T_{\ell' m'} \int d^2\hat{\mathbf{n}} Y_{\ell' m'}(\hat{\mathbf{n}}) W(\hat{\mathbf{n}}) Y^*_{\ell m}(\hat{\mathbf{n}}) \tag{1.53}$$

and the measured power spectrum by (see for example Hivon et al., 2002)

$$\tilde{C}_{\ell_1} = \frac{1}{(2\ell_1+1)} \sum_{m_1=-\ell_1}^{\ell_1} \left\langle \tilde{T}_{\ell_1 m_1} \tilde{T}^*_{\ell_1 m_1} \right\rangle$$

$$= \sum_{\ell_2} M_{\ell_1 \ell_2} C_{\ell_2} \tag{1.54}$$

where C_{ℓ_2} is the true power spectrum and M is the mode coupling matrix given by

$$M_{\ell_1 \ell_2} = \frac{(2\ell_2+1)}{4\pi} \sum_{\ell_3} (2\ell_3+1) \mathcal{W}_{\ell_3} \begin{pmatrix} 0 & 0 & 0 \\ \ell_1 & \ell_2 & \ell_3 \end{pmatrix}^2, \tag{1.55}$$

with the power spectrum of the mask defined as

$$\mathcal{W}_\ell = \frac{1}{2\ell+1} \sum_m |W_{\ell m}|^2, \tag{1.56}$$

$W_{\ell m}$ being the spherical harmonic components of the mask $W(\hat{\mathbf{n}})$.

For a polar cap with angular radius Θ, this function is analytically known to be (Dahlen & Simons, 2007)

$$\mathcal{W}^{\rm cap}_\ell = \frac{\pi}{(2\ell+1)^2} [P_{\ell-1}(\cos\Theta) - P_{\ell+1}(\cos\Theta)]^2. \tag{1.57}$$

where P_ℓ is a Legendre Polynomial of order ℓ and $P_{-1}(\mu) = 1$.

The window function in equation (1.51) corresponding to the polar cap is a "tophat" in the sense that it abruptly falls to zero at the edge. The power spectrum (equation (1.57)) of this window has an oscillatory behavior showing a lot of power over a large range of multipoles, an effect sometimes called *ringing*. Ringing causes the mode coupling matrix, $M_{\ell\ell'}$ to develop large off-diagonal terms, as illustrated in Fig. 1.4, and consequently the value of the measured power spectrum at any multipole (equation (2.54)) has non-trivial contributions from many neighboring multipoles. This causes the measured power spectrum to be biased, and its effect is particularly evident for power spectra with a sharp fall-off

such as the CMB. As is evident from Fig. 1.4, the effect of mode coupling due to the polar cap becomes a serious problem for the lensed and unlensed power spectra starting at moderately low multipoles ($\ell \sim 2000$). Although in principle one could compare the measured power spectrum with a theoretical power spectrum which has been convolved with the same mode coupling matrix, the effect is so strong in this case that the lensed and unlensed spectra almost overlap each other. This problem can be mitigated in principle by inverting a binned version of the mode coupling matrix and thereby decorrelating the power spectra. However an easier and less computationally expensive solution can be achieved in the following manner.

The off diagonal terms of the mode coupling matrix can be reduced significantly by apodizing the polar cap window function. Parenthetically, we note that there exists a general method of generating tapers on a cut-sky map, so as to minimize the effect of mode coupling. This is referred to as the multi-taper method (see Chapter 2; Dahlen & Simons, 2007). However, for our purpose, it suffices to define a simpler apodizing window as

$$W(\hat{\mathbf{n}}) = \begin{cases} 1 & \text{for } \theta < \theta_0 < \theta_{\rm cap} \\ \sin(\frac{\pi}{2}\frac{\theta_{\rm cap}-\theta}{\theta_{\rm cap}-\theta_0}) & \text{for } \theta_0 < \theta < \theta_{\rm cap} \\ 0 & \text{for } \theta > \theta_{\rm cap}. \end{cases} \tag{1.58}$$

The power spectrum of this window can be easily computed using HEALPix , and thus the mode coupling matrix can be readily generated using equation (1.55). We found that an apodization window with $(\theta_{\rm cap} - \theta_0) \simeq 1.2$ degree, corresponding to ~ 80 pixels, works extremely well without eating into too much of the map. A section of the mode coupling matrix and the corresponding convolved power spectrum are displayed in Fig. 1.4. This figure shows that the power spectrum convolved with the apodized window function has negligible mode coupling. Parenthetically, it is interesting to note that simply scaling the theory power spectrum by the fraction of the sky covered, $f_{\rm sky}$, seems to do a good job in mimicking the effect of the partial sky coverage, at least for the lower multipoles. In fact, this approximation is an exact result for a white power spectrum. However, when the window is apodized, the effective area of coverage, $f_{\rm sky}^{\rm eff} = \int W^2(\hat{\mathbf{n}}) d^2\hat{\mathbf{n}}/4\pi$, goes down a

little (by $\sim 2.5\%$ for our apodization). We use $f_{\rm sky}^{\rm eff}$ scaled theory power spectra only in some plots in this paper. For the analysis, we perform the full mode coupling calculation. Therefore, when comparing the power spectrum of some quantity defined on the polar cap with theoretical predictions, we first multiply the map by the apodized window and compare the resulting power spectrum with the theoretical power spectrum mode-coupled through the same weighting window.

1.5 Results

We illustrate the algorithm with an effective lensing simulation at the HEALPix resolution of $NSIDE = 4096$. Since some rays end up outside the polar cap after lensing, we have actually used an unlensed CMB realization (using the `synfast` facility of HEALPix) on an area larger than our fiducial polar cap to accommodate those rays. As the gradient of the lensing potential is ill defined at the edge of the polar cap, we ignore a ring of pixels near the edge of the lensed map for all subsequent analyses. It is particularly instructive to look at the difference of the lensed and the unlensed maps, as shown in Fig. 1.5, as it shows the large scale correlations imprinted on the CMB due to the large scale modes in the deflection field.

We compute the angular power spectrum of the lensed and unlensed CMB maps using an apodized weighting scheme as discussed in §1.4. The resulting power spectra are displayed in Fig. 1.6 for the entire range of multipoles analyzed, and are compared with the mode-coupled theoretical power spectra. The theoretical lensed CMB power spectrum used for the calculation was generated with the CAMB code, using the all-sky correlation function technique (Challinor & Lewis, 2005) and including nonlinear corrections to the matter power spectrum. In Fig. 1.7, we show a zoomed-in version of the lensed power spectrum, in the multipole range $500 < \ell < 3500$. From visual inspection of these plots it is evident that the simulation does a good job in reproducing the theoretically expected lensed power spectrum, at least in the range of multipoles over which the computation of the theoretical power spectrum is robust. We defer a detailed comparison of the simulation to the theory

to §1.6.3.

1.6 Tests

1.6.1 Tests for the mass sheets

In this section we perform some sanity checks to ensure that the projection from the simulation box onto the Polar Cap has been properly performed. We first test that the total mass in each slice is equal to the theoretical mass expected from the mean cosmology, the later being given by

$$M_{\rm slice}^{\rm theory} = \Omega_{\rm m}\rho_{\rm crit}\bar{\eta}^2\tilde{\Omega}_{\rm cap}\Delta\eta \tag{1.59}$$

where $\Delta\eta$ is the comoving thickness of the slice at a comoving distance $\bar{\eta}$. We compare this quantity with

$$M_{\rm slice} = \sum_{i=1}^{N_{\rm cap}} \sigma_i \Omega_{\rm pix} \tag{1.60}$$

which is the total mass on the plane from the simulation. The percentage difference between the two is depicted in Fig. 1.8 for the lensing-planes. Notice that the agreement is good to within 0.5% for the high redshift planes, in which the solid angle $\Omega_{\rm cap}$ corresponds to a large comoving area. For low redshifts there are large variations due to the fact that matter is highly clustered and $\Omega_{\rm cap}$ corresponds to a small comoving area. These fluctuations at low redshift represent the chance inclusion or exclusion of large dark matter halos within the light cone.

Next, we make sure that the probability density function (PDF) of the surface mass density is well behaved for each plane, and is well modeled by analytic PDFs such as the lognormal (Kayo et al., 2001; Taruya et al., 2002) or the model proposed by Das & Ostriker (2006). In Fig. 1.9 we show these two models over-plotted on the PDFs drawn from the forty-five lensing-planes.

The model of Das & Ostriker (2006) is a better fit to the simulation than the lognormal, especially at high surface mass density. Note in that paper the authors used the first year WMAP parameters, whereas the present simulation is run with the WMAP 3-year

parameters, including a significantly different σ_8. The fact that the model still represents the simulation well suggests that it is quite general.

1.6.2 Tests for the convergence plane

As described in §1.3.2, the effective convergence plane was produced by a two step process. First, we computed the effective convergence plane by weighting the surface mass density planes from the simulation with appropriate geometrical factors. Let us call it the map $\mathbf{M}_1$. This map, therefore, includes contribution from the large scale structure only out to the redshift of the farthest TPM plane, $z = 4.05$. Next we added in the contribution from $z > 4.05$, by generating a Gaussian random realization of the effective convergence from a theoretical power spectrum (the map $\mathbf{M}_2$). Therefore the final convergence map is simply $(\mathbf{M}_1 + \mathbf{M}_2)$. It is interesting to compare the power spectrum of the map $\mathbf{M}_1$ with that expected from theoretical considerations. Since CMB lensing is most sensitive to large scale modes, we should make sure that these modes were realized correctly in our simulated convergence plane. Incidentally, these scales are also linear to mildly nonlinear. Therefore, we should expect the power spectrum of the convergence map to be well replicated by the theoretical prediction at least in the quasi-linear range of multipoles ($\ell \lesssim 2000$) where simple non-linear prescriptions suffice. In order to compute the theoretical power spectra for the maps $\mathbf{M}_1$ and $(\mathbf{M}_1 + \mathbf{M}_2)$, we used the Limber approximation to project the matter power spectrum $P(k, \eta)$ computed from CAMB. The Limber approximation simplifies the full curved-sky calculation, and is valid for $l \gtrsim 10$. Since for lower values of the multipole we have few realizations of the convergence modes, the power spectrum computed from the simulated map is noisy in this regime, rendering it practically useless for comparison with theory. Therefore, an accurate computation of the theoretical convergence power spectrum for these lowest multipoles is unnecessary, and the Limber calculation suffices. Under the same approximation, the shot noise contribution to the convergence field can be computed as

$$C_\ell^{\rm shot} = \sum_j \Delta\eta_j \left(\frac{3}{2}\Omega_{\rm m}(1+z_j)\frac{(\eta_s - \eta_j)\eta_j}{\eta_s}\frac{H_0^2}{c^2}\right)^2 \frac{1}{\bar{n}_j}, \tag{1.61}$$

where $\bar{n}_j = N_j/(\eta_j^2 \Delta\eta_j \tilde{\Omega}_{\rm cap})$, N_j being the total number of particles in the j-th shell. We compute both a linear and a non-linear version of the convergence power spectrum, where the latter includes non-linear corrections to the matter power spectrum from a halo model based fitting formula (Smith et al., 2003). We plot the power spectrum computed from the simulated convergence map $\mathbf{M}_1$, and the corresponding theoretical power spectra, in Fig. 1.10. As is evident from the figure, the simulated power spectrum is in accord with the linear theory power spectrum for $\ell \lesssim 300$, beyond which the effect non-linearities creep in. However, it is impressive that the non-linear corrections to the power spectrum are in good agreement with the simulation up to relatively high multipoles. The same quantities are plotted for the convergence map out to the redshift of the CMB in Fig. 1.11. We find in both cases that beyond multipoles of ~ 6000 the simulation contains more non-linear power than predicted by the theory.

1.6.3 Tests for the lensed CMB map

Since CMB lensing is essentially a remapping of points, the one-point statistics should remain unaffected by the lensing. We check for this by drawing up the one-point PDF's of the unlensed and lensed maps, and find them to be consistent to within 0.8%. Next, we compare the power spectrum of the simulated lensed map (cf. Figures 1.6 & 1.7) with the theoretical predictions as computed with the CAMB code. For a quantitative comparison, we consider a range of multipoles ($500 \leq \ell \leq 3500$) in the acoustic regime. We do not consider the lower multipoles as they exhibit negligible lensing effect. We found that for a fixed input cosmology, the tail ($\ell \gtrsim 3500$) of the lensed CMB power spectrum predicted by CAMB depends somewhat sensitively on input parameters, specifically the combination $k\eta_{\rm max}$, which controls the maximum value of the wavenumber for which the matter power spectrum in computed. However, the lensed power spectrum from CAMB is robust towards changes in the auxiliary input parameters for the range of multipoles, $\ell < 3500$. Also, the lensed CMB multipoles beyond this range couple to relatively small scale modes of the deflection field where our simulation has more power than expected from non-linear theory.

In fact, beyond $\ell \simeq 4000$ the simulated power spectrum is found to deviate systematically from the theoretical spectrum.

As the simulated power spectrum, $\tilde{C_\ell}^{\rm sim}$, was computed using an apodized window as described in §1.4, the appropriate theoretical curve to compare this result with is the power spectrum from CAMB after it has been convolved with the coupling matrix defined by the same weighting scheme (cf. equation 2.54). We denote the latter quantity by $\tilde{C_l}^{\rm theory}$. In order to facilitate the comparison we bin the raw spectrum in ℓ. In the multipole range considered ($500 \leq \ell \leq 4000$), the quantity $\mathcal{C}_\ell = \ell^4 C_\ell$ is flat (see Fig. 1.7) and therefore a better candidate for binning. We denote the difference between the simulated and the theoretical version of this quantity by

$$\delta\mathcal{C}_l \equiv \tilde{\mathcal{C}}_l^{\rm sim} - \tilde{\mathcal{C}}_l^{\rm theory}. \tag{1.62}$$

For each of the N bins indexed by b, we compute the mean, $\delta\mathcal{C}_b$, and the sample variance, s_b^2, of the observations falling inside that bin. In order to account for that fact that cosmic variance errors will be higher in our case due to incomplete sky coverage, we define an effective variance as $\sigma_b^2 = s_b^2/f_{\rm sky}^{\rm eff}$.

We quantify the goodness of fit between the simulation and the model by defining a χ^2 statistic as

$$\chi^2 = \sum_{b=1}^{N} \frac{(\delta\mathcal{C}_b)^2}{\sigma_b^2}. \tag{1.63}$$

We perform the χ^2 analysis by uniformly binning the power spectra in the range $500 \leq \ell \leq 4000$ into 52 bins with a bin width of $\Delta\ell = 60$.The binned values along with the error bars are displayed in Fig. 1.12. We find a value $\chi^2 = 52.93$, suggesting an appreciable agreement with the theory.

1.7 Conclusions

In this paper, we have put forward an algorithm for end-to-end simulation of the gravitational lensing of the cosmic microwave background, starting with an N-body simulation and fully taking into account the curvature of the sky. The method is applicable to maps of

any geometry on the surface of the sphere, including the whole sky. Our algorithm includes prescriptions for generating spherical convergence planes from an N-body light cone and subsequently ray-tracing through the planes to simulate lensing. The central feature of the algorithm is the use of a highly accurate interpolation method that enables sampling of both the deflection fields on intermediate lensing planes and the unlensed CMB map on an irregular grid. We have provided a detailed description of both a multiple plane ray tracing and an effective lensing version of the algorithm. The latter setting has been used to illustrate the algorithm, by generating an $\sim 1'$ resolution lensed CMB map. We have compared the power spectra of the effective convergence map and the lensed CMB map with theoretical predictions, and have obtained good agreement. After this paper was completed, Fosalba et al. (2007) described a similar method of producing convergence maps in spherical geometry, and Carbone et al. (2007) also described their techniques for simulating CMB lensing maps. The latter used broadly similar techniques to those described here, although they used a different method to obtain the deflection field.

Applications of the algorithm can be manifold. The associated large scale structure planes can be populated with tracers of mass and foreground sources, in order to simulate cross-correlation studies and to investigate the effects of contamination. This lensing portion of the algorithm can be applied to generate lensed maps in large scale structure simulations that produce spherical shells (Fosalba et al., 2007). The multiple plane algorithm can be particularly useful, after trivial modifications, in simulating weak lensing of galaxies or the 21-cm background on a large sky. The lensed CMB maps can be used as inputs to telescope simulators for projects such as ACT and PLANCK, and will help in the analysis and interpretation of data. We intend to release all-sky high resolution lensed CMB maps made using this algorithm in near future.

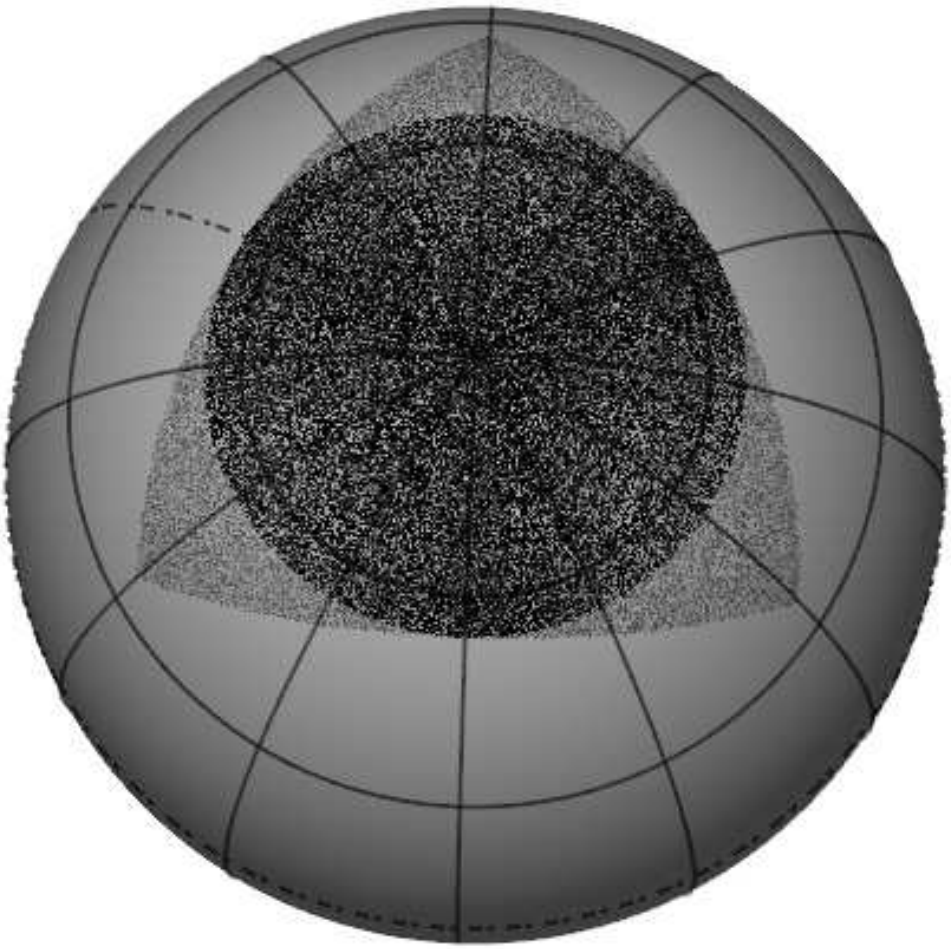

Figure 1.3: Illustration of the Polar Cap geometry. The figure shows a 3-D rendering of the sphere using the CMBVIEW[11]software, looking down towards the North Pole. The lightly shaded triangular region correspond to the positions of the particles in the octant from the N-body simulation box at a typical time step. The darker dots define what we call the Polar Cap in the text. The surface mass density of the pixels inside this Polar Cap region are saved in shells out to z=4.

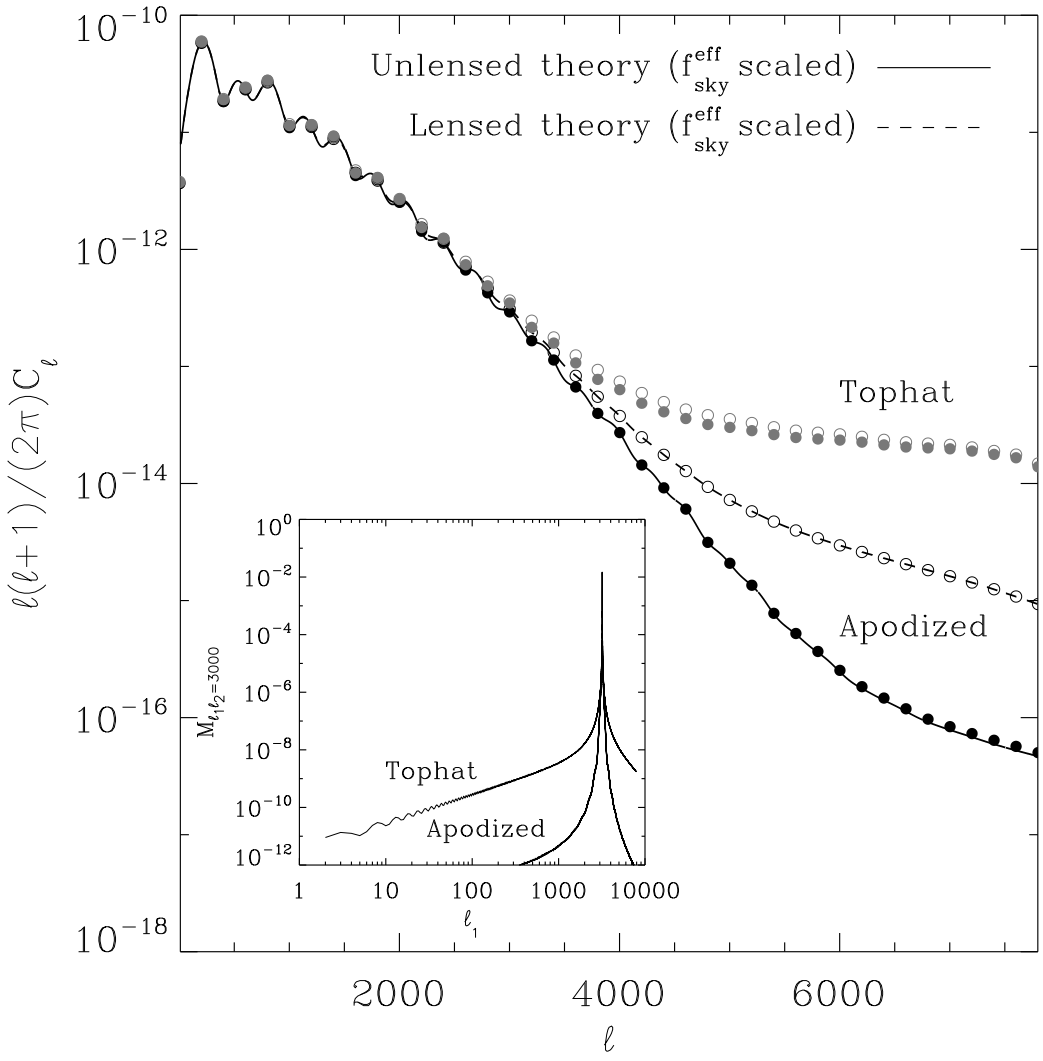

Figure 1.4: Effect of apodization of the window function. The continuous line is the unlensed CMB power spectrum and the dashed line is the lensed one. Both have been scaled by $f_{\rm sky}^{\rm eff}$, the effective fractional sky coverage (see text). The gray filled and open circles labeled "Tophat", represent, respectively, the theoretical unlensed and lensed power spectra convolved with a window function that is unity inside the polar cap and zero outside. The black filled and open circles represent the same quantities, but in the case of a window which is apodized at the edge of the polar cap, as discussed in the text. Aliasing of power to higher multipoles due to mode coupling is significantly reduced in the latter case. We use the apodized window to mask the polar cap maps for computing various power spectra, and use the corresponding theory power spectrum convolved with the same window for comparing our results with theory. (*Inset:* The mode coupling matrix $M_{\ell_1\ell_2}$ as a function of ℓ_1, for $\ell_2 = 3000$, showing the reduction in the power in off-diagonal elements as a result of apodization.)

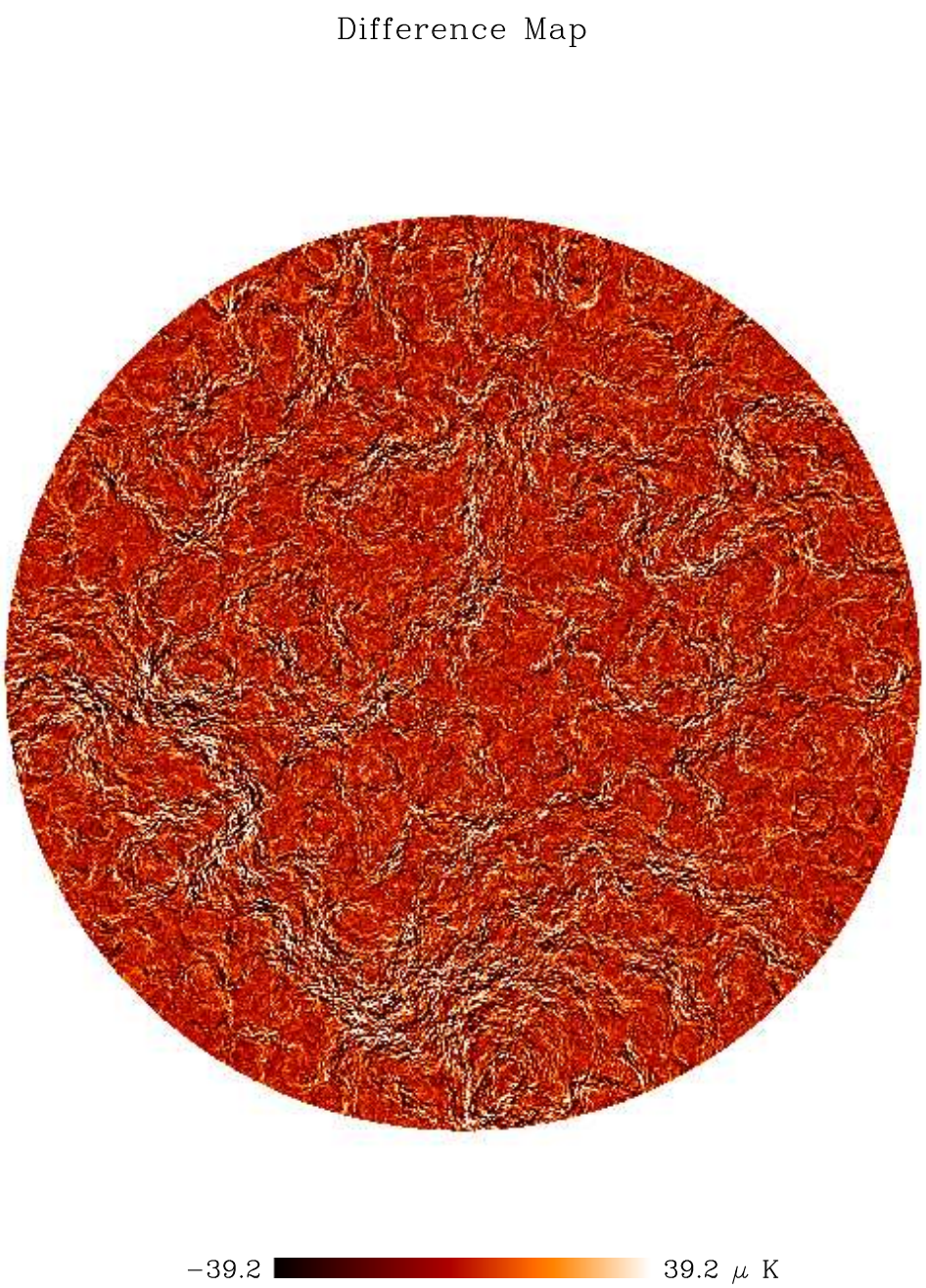

Figure 1.5: The Polar Cap map obtained after subtracting the unlensed CMB map from the lensed CMB map. To enhance the contrast, we have remapped the color scale to the range $(-2\sigma, 2\sigma)$, σ being the standard deviation of the map.

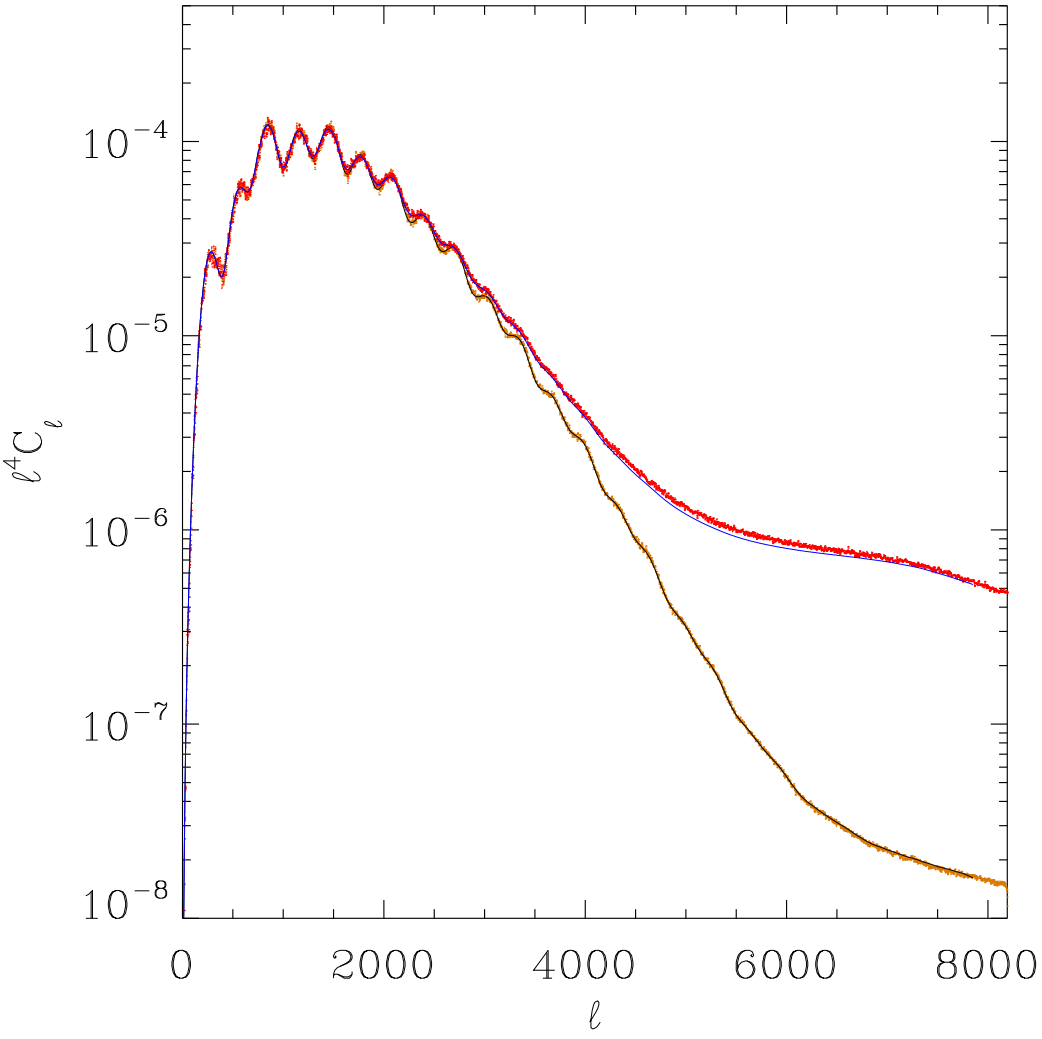

Figure 1.6: The lensed and unlensed CMB angular power spectra obtained from the simulation compared with the theoretical models. The red and orange dots represent, respectively, the lensed and unlensed angular power spectra obtained from the polar cap using the methods described in §1.4. The solid black curve signifies the theoretical unlensed power spectrum taking into account the mode coupling due to the apodized polar cap window function. The blue solid curve represents the same for the lensed power spectrum.

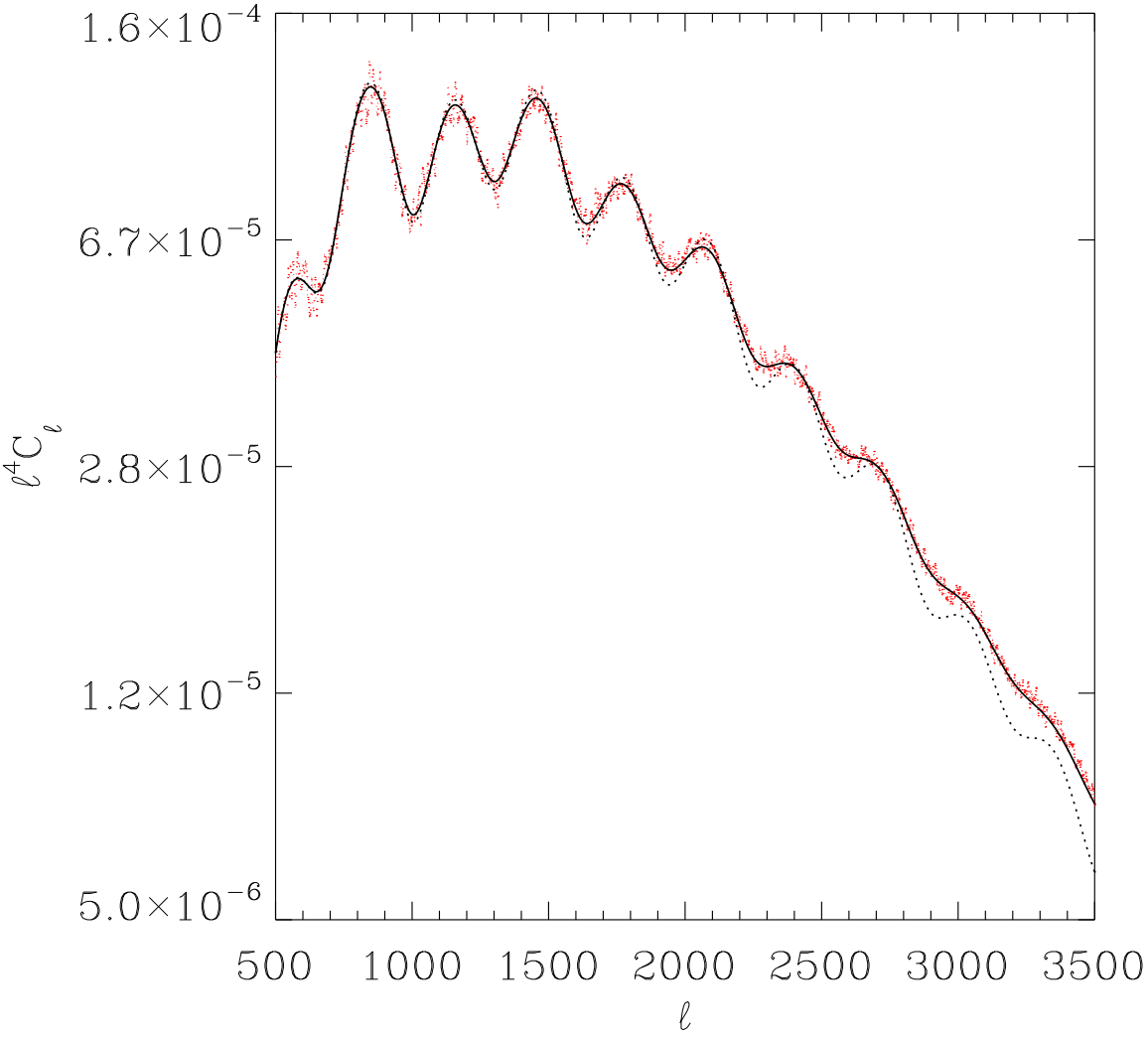

Figure 1.7: Lensed CMB angular power spectrum in the multipole range $500 < \ell < 3500$ obtained from the simulation compared with the theoretical model. The red dots represent the lensed angular power spectrum obtained from the polar cap using the methods described in §1.4. The solid black curve signifies the theoretical lensed CMB power spectrum taking into account the mode coupling due to the apodized polar cap window function. The dotted black curve represents the same for the theoretical unlensed power spectrum and is shown here for contrast to the lensed case.

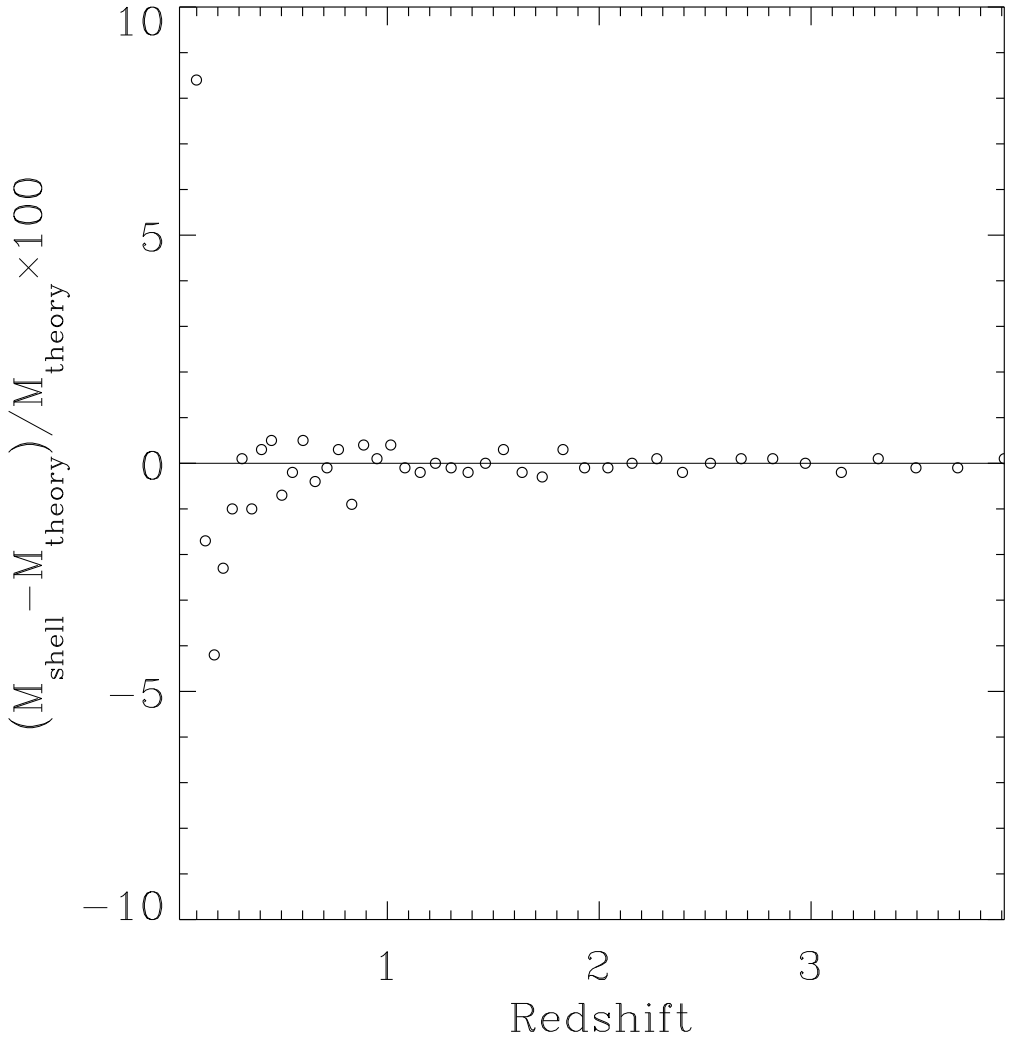

Figure 1.8: The mass in the lensing-slices compared with that expected from theory.

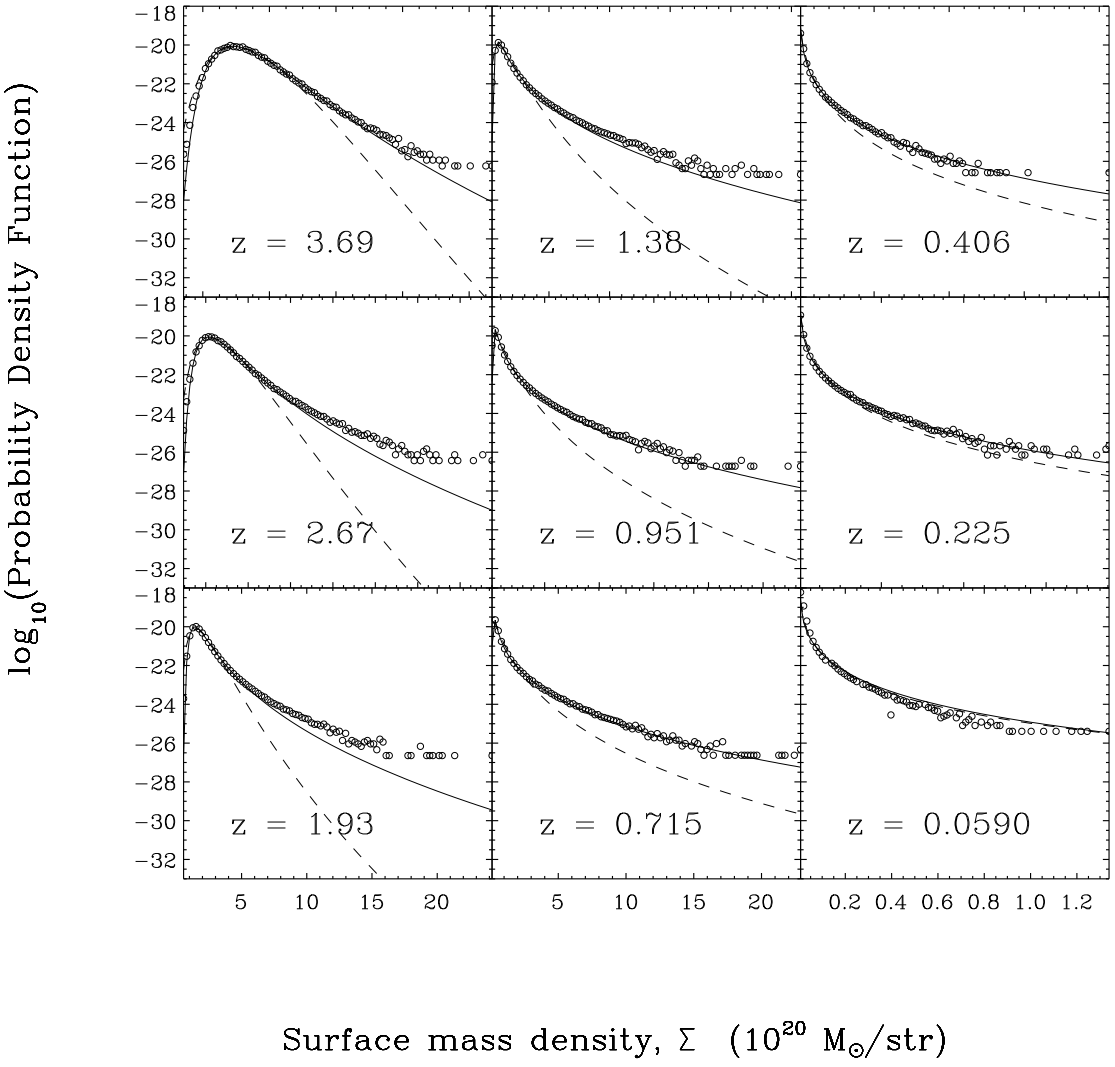

Figure 1.9: The probability density function (PDF) of the surface mass density in the lensing-planes (circles) compared with the lognormal (dashed line) and the Das & Ostriker (2006) model (solid line).

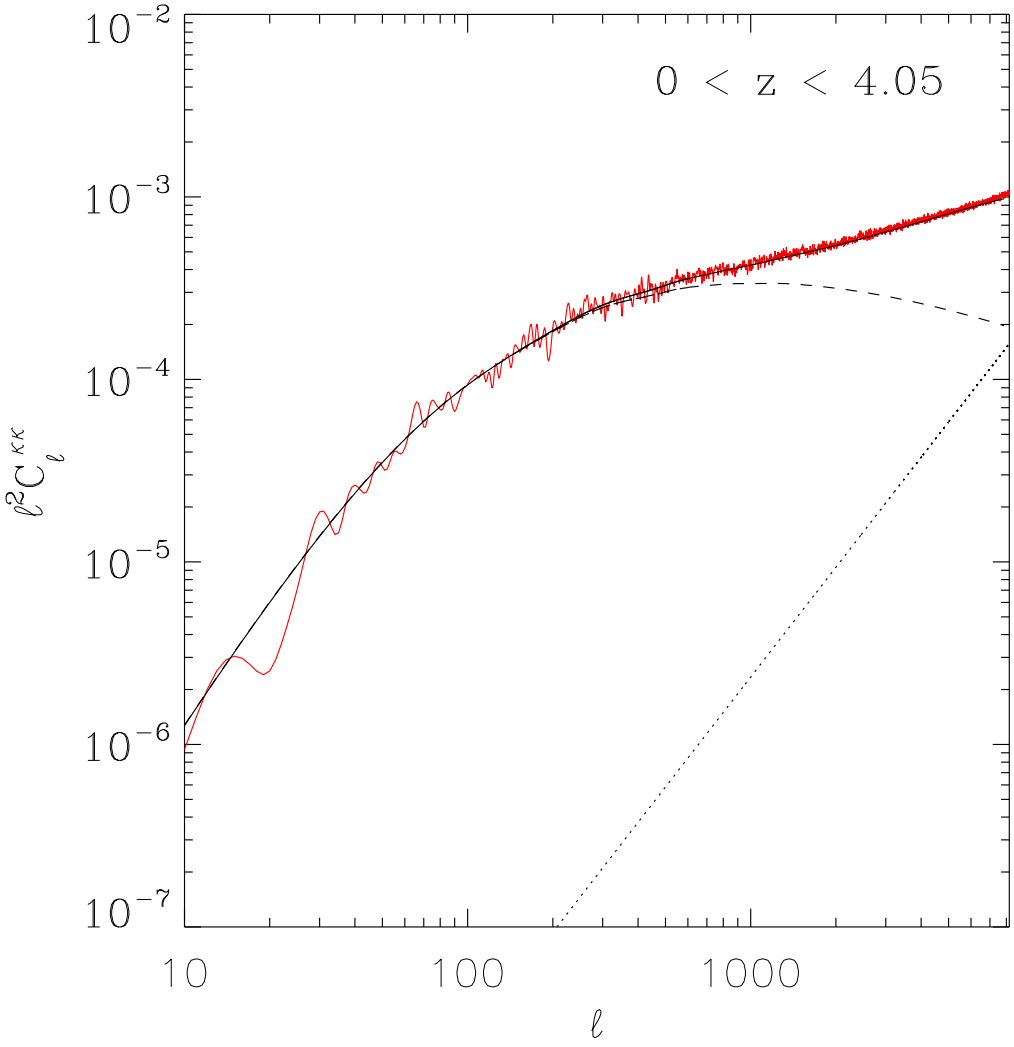

Figure 1.10: Power spectrum of the effective convergence map $\mathbf{M}_1$ produced from the simulated lensing planes alone. The red line shows the power spectrum computed from the convergence map and the black solid line represents the theoretical power spectrum with non-linear corrections. The power spectrum is corrected for the shot noise contribution (see text) which is displayed as the dotted line. The black dashed line corresponds to the linear theory power spectrum. All theory power spectra are mode-coupled with the apodizing window.

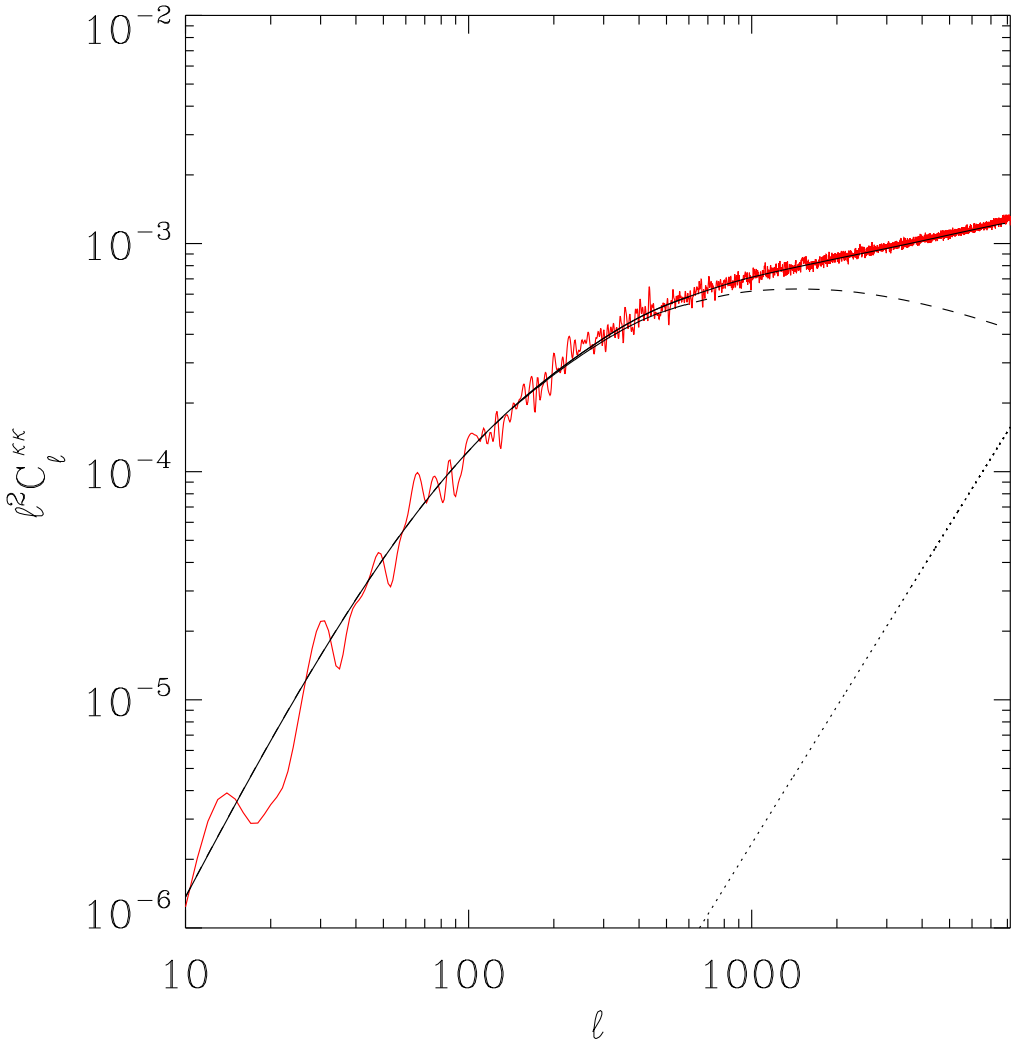

Figure 1.11: Power spectrum of the effective convergence map ($\mathbf{M}_1 + \mathbf{M}_2$) after adding in high redshift contribution. The red line shows the power spectrum computed from the convergence map and the black solid line represents the theoretical power spectrum with non-linear corrections. The power spectrum is corrected for the shot noise contribution (see text) which is displayed as the dotted line. The black dashed line corresponds to the linear theory power spectrum. All theory power spectra are mode-coupled with the apodizing window.

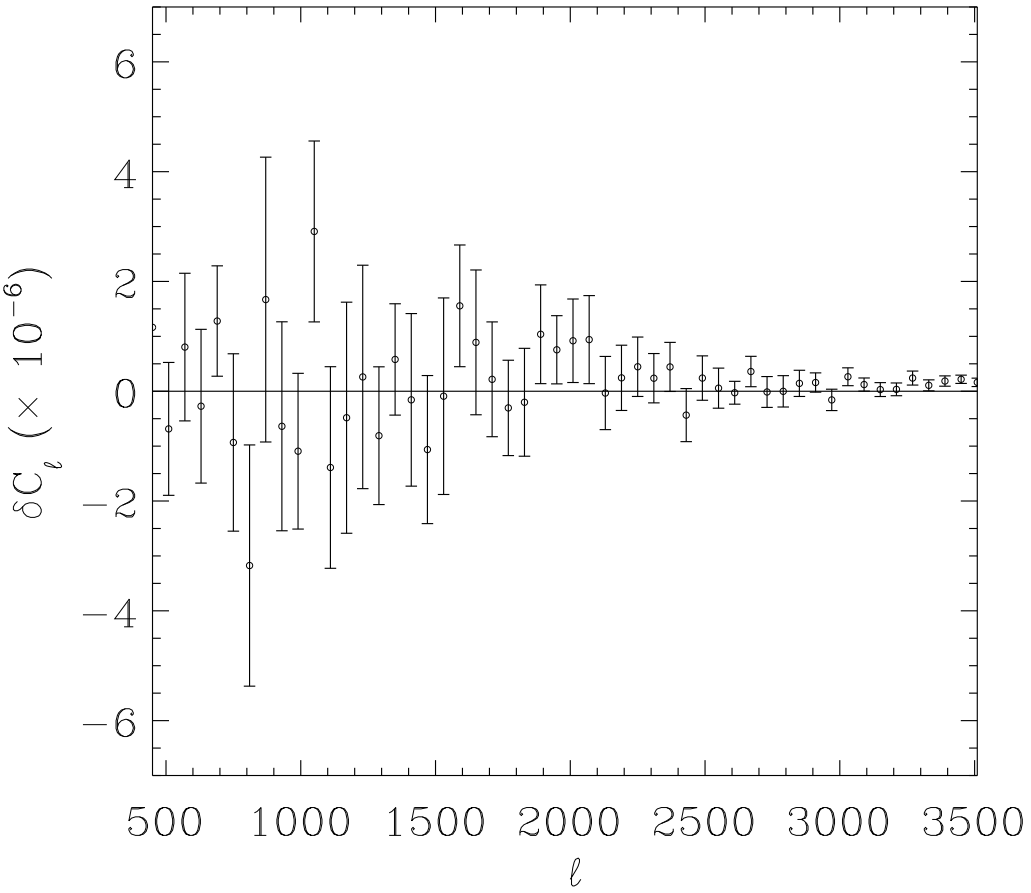

Figure 1.12: Difference between the simulated and the theoretical binned power spectrum for lensed CMB.

Acknowledgements

SD would sincerely like to thank his advisor, David Spergel for suggesting the key ideas of the project and for his continuous guidance and encouragement throughout its development. SD is specially grateful to Chris Hirata for generously providing the NISHT code and for numerous useful discussions. We thank Joanna Dunkley for careful reading of the manuscript and thoughtful suggestions. SD acknowledges the support from the NASA Theory Program NNG04GK55G and the NSF grant AST-0707731. This research was facilitated by allocations of advanced computing resources from the Pittsburgh Supercomputing Center and the National Center for Supercomputing Applications. In addition, computational facilities at Princeton supported by NSF grant AST-0216105 were used, as well as high performance computational facilities supported by Princeton University under the auspices of the Princeton Institute for Computational Science and Engineering (PICSciE) and the Office of Information Technology (OIT). Some of the results in this paper have been derived using the HEALPix (Gorski et al., 2005) package.

References

Akima, H. 1996, ACM Trans. Math. Softw., 22, 357

Bode, P. & Ostriker, J. P. 2003, ApJS, 145, 1

Bode, P., Ostriker, J. P., Weller, J., & Shaw, L. 2007, ApJ, 663, 139

Bode, P., Ostriker, J. P., & Xu, G. 2000, ApJS, 128, 561

Carbone, C., Springel, V., Baccigalupi, C., Bartelmann, M., & Matarrese, S. 2007, ArXiv e-prints, 711

Challinor, A., & Chon, G. 2002, Phys. Rev. D, 66, 127301

Challinor, A. & Lewis, A. 2005, Phys. Rev. D, 71, 103010

Dahlen, F. A. & Simons, F. J. 2007, ArXiv e-prints, 705

Das, S. & Ostriker, J. P. 2006, ApJ, 645, 1

Fosalba, P., Gaztanaga, E., Castander, F., & Manera, M. 2007, ArXiv e-prints, 711, arXiv:0711.1540

Gorski, K. M., Hivon, E., Banday, A. J., Wandelt, B. D., Hansen, F. K., Reinecke, M., & Bartelmann, M. 2005, The Astrophysical Journal, 622, 759

Hirata, C. M., Ho, S., Padmanabhan, N., Seljak, U., & Bahcall, N. 2008, ArXiv e-prints, 801, arXiv:0801.0644

Hirata, C. M., Padmanabhan, N., Seljak, U., Schlegel, D., & Brinkmann, J. 2004, Phys. Rev. D, 70, 103501

Hirata, C. M. & Seljak, U. 2003, Phys. Rev. D, 67, 043001

Hivon, E., Górski, K. M., Netterfield, C. B., Crill, B. P., Prunet, S., & Hansen, F. 2002, ApJ, 567, 2

Hu, W. 2000, Phys. Rev. D, 62, 043007

Hu, W., Holz, D. E., & Vale, C. 2007, ArXiv e-prints, 708

Hu, W., Huterer, D., & Smith, K. M. 2006, ApJ, 650, L13

Hu, W. & Okamoto, T. 2002, ApJ, 574, 566

Jain, B., Seljak, U., & White, S. 2000, ApJ, 530, 547

Kayo, I., Taruya, A., & Suto, Y. 2001, ApJ, 561, 22

Komatsu, E., Kogut, A., Nolta, M. R., Bennett, C. L., Halpern, M., Hinshaw, G., Jarosik, N., Limon, M., Meyer, S. S., Page, L., Spergel, D. N., Tucker, G. S., Verde, L., Wollack, E., & Wright, E. L. 2003, ApJS, 148, 119

Lesgourgues, J., Perotto, L., Pastor, S., & Piat, M. 2006, Phys. Rev. D, 73, 045021

Lewis, A. 2005, Phys. Rev. D, 71, 083008

Lewis, A. & Challinor, A. 2006, Phys. Rep., 429, 1

Marian, L. & Bernstein, G. M. 2007, ArXiv e-prints, 710

Okamoto, T. & Hu, W. 2003, Phys. Rev. D, 67, 083002

Peiris, H. V. & Spergel, D. N. 2000, ApJ, 540, 605

Sehgal, N., Trac, H., Huffenberger, K., & Bode, P. 2007, ApJ, 664, 149

Seljak, U. 1996, ApJ, 463, 1

Smith, K. M., Hu, W., & Kaplinghat, M. 2006a, Phys. Rev. D, 74, 123002

Smith, K. M., Zahn, O., & Doré, O. 2007, Phys. Rev. D, 76, 043510

Smith, R. E., Peacock, J. A., Jenkins, A., White, S. D. M., Frenk, C. S., Pearce, F. R., Thomas, P. A., Efstathiou, G., & Couchman, H. M. P. 2003, MNRAS, 341, 1311

Smith, S., Challinor, A., & Rocha, G. 2006b, Phys. Rev. D, 73, 023517

Spergel, D. N., Bean, R., Doré, O., Nolta, M. R., Bennett, C. L., Dunkley, J., Hinshaw, G., Jarosik, N., Komatsu, E., Page, L., Peiris, H. V., Verde, L., Halpern, M., Hill, R. S., Kogut, A., Limon, M., Meyer, S. S., Odegard, N., Tucker, G. S., Weiland, J. L., Wollack, E., & Wright, E. L. 2007, ApJS, 170, 377

Spergel, D. N., Verde, L., Peiris, H. V., Komatsu, E., Nolta, M. R., Bennett, C. L., Halpern, M., Hinshaw, G., Jarosik, N., Kogut, A., Limon, M., Meyer, S. S., Page, L., Tucker, G. S., Weiland, J. L., Wollack, E., & Wright, E. L. 2003, ApJS, 148, 175

Taruya, A., Takada, M., Hamana, T., Kayo, I., & Futamase, T. 2002, ApJ, 571, 638

Vale, C., & White, M. 2003, ApJ, 592, 699

Zaldarriaga, M. 2000, Phys. Rev. D, 62, 063510

Zaldarriaga, M. & Seljak, U. 1999, Phys. Rev. D, 59, 123507

Chapter 2

Efficient Power Spectrum Estimation for High Resolution CMB Maps

Abstract

Estimation of the angular power spectrum of the Cosmic Microwave Background (CMB) on a small patch of sky is usually plagued by serious spectral leakage, specially when the map has a hard edge. Even on a full sky map, point source masks can alias power from large scales to small scales producing excess variance at high multipoles. We describe a new fast, simple and local method for estimation of power spectra on small patches of the sky that minimizes spectral leakage and reduces the variance of the spectral estimate. For example, when compared with the standard uniform sampling approach on a 8 degree $\times$ 8 degree patch of the sky with 2% area masked due to point sources, our estimator halves the errorbars at $\ell = 2000$ and achieves a more than fourfold reduction in errorbars at $\ell = 3500$. Thus, a properly analyzed experiment will have errorbars at $\ell = 3500$ equivalent to those of an experiment analyzed with the now standard technique with $\sim 16 - 25$ times the integration time.

2.1 Introduction

Cosmic Microwave Background (CMB) is a statistically isotropic (Hajian & Souradeep, 2006) and Gaussian (Komatsu et al., 2003) random field. If we ignore secondary effects, all of the information in high resolution CMB maps is encoded in the angular correlation function or equivalently, in the angular power spectrum, C_ℓ. The angular power spectrum is widely used to estimate the cosmological parameters. Accurate measurements of angular power spectrum are needed for precise estimation of cosmological parameters.

Over the past decade, CMB power spectrum has been measured over a large range of multipoles, ℓ, by various groups (Gorski et al., 1996; Nolta et al., 2008; Hinshaw et al., 2008; Reichardt et al., 2008; QUaD collaboration: C. Pryke et al., 2008). And more experiments are under way to measure the C_ℓ on smaller scales with high accuracy .e.g. the Atacama Cosmology Telescope (ACT)[1] , South Pole Telescope (SPT)[2] and Planck[3] . Most power spectrum analyses use uniform or noise weighted maps. This performs reasonably well for power spectra that have nearly equal power in equal logarithmic intervals of multipoles, *i.e.* $\ell \leq 1000$ for the CMB. For smaller scales, (larger ℓ) this method is non-optimal, as we show in section 2.5. CMB power spectrum estimated from an incomplete sky map is the underlying full-sky power spectrum convolved with the power spectrum of the mask. This leads to coupling of modes in the estimated power spectrum. For high resolution experiments such as ACT and SPT which will map the small scale anisotropies of the CMB on small patches of the sky, this mode-mode coupling will be a serious problem. The reason is that CMB power spectrum is very red on those scales (it falls off as ℓ^{-4} at large ℓ) and hence is highly vulnerable to the leakage of power due to mode-mode coupling. There are two methods to remedy this: to taper the map near the sharp edges, and to pre-whiten the CMB power spectrum. In order to minimize the loss of information due to applying a taper to the map, we use the multitaper method (Percival & Walden, 1993). This method involves weighting the map with a set of orthonormal functions which are space limited but

[1] http://www.physics.princeton.edu/act
[2] http://pole.uchicago.edu
[3] http://www.rssd.esa.int/Planck/

maximally concentrated in the frequency domain. Power spectrum of each of these tapered maps is a measurement of the power spectrum of that map with a different amount of mode coupling. Final power spectrum is obtained from a particular linear combination of these tapered power spectra that minimizes the bias in the estimated power spectrum. The use of multiple tapers also reduces the error-bars in the measured power spectrum.

Mode coupling is less harmful if the map has a nearly white power spectrum. Traditionally, an inverse covariance matrix weighting is used in analysis to prewhiten the maps (Tegmark, 1997). This method works well, but is a computationally expensive, non-local operation and may be complicated to implement, specially for high resolution experiments (Doré et al., 2001; Smith et al., 2007). We propose a simple and local prewhitening operator in real space (§ 2.4) that is fast to implement and reduces the bias due to the leakage of power. This method prevents the unnecessarily large error bars at $\ell \gtrsim 1500$ due to the point source masks. Usually masks have sharp edges and holes at the positions of point sources. This leads to a mode-coupled power spectrum that is highly biased at large ℓ. Deconvolution of the mode-coupled power spectrum is a well-studied problem in the CMB data analysis literature (Hivon et al., 2002) and has been applied to many experiments. But deconvolution of a highly biased power spectrum leads to large error bars in the final power spectrum at large ℓ. The mode coupling problem will be worse for the upcoming set of CMB experiments as bright point sources will be much more of a limiting foreground at high resolution.

As we show in § 2.5, prewhitening followed by the multitaper method for power spectrum estimation reduces the error-bars (specially at large ℓ) in the decoupled power spectrum (cf. Figs. 2.14 & 2.15).

We begin with a review of the multitaper method in one-dimension in § 2.2 and discuss the salient features of the method, generalizing it to the two-dimensional case. Next, we discuss the statistical properties of multitaper spectrum estimators. As a simple application, we demonstrate the method in context of CMB power spectrum estimation in § 2.3. Next, we formulate the prewhitening method (§ 2.4) and apply it to the case of CMB power spectrum

estimation in presence of masks. In § 2.5, we describe the algorithm for deconvolving the power spectrum and the implications of the multitaper method and prewhitening in its context. We summarize and conclude in § 2.6.

2.2 A Brief Review of the Multitaper Method

The problem of estimating the power spectrum of a stationary, ergodic process, sampled at discrete intervals and observed over a finite segment of its duration of occurrence, is an old and well-studied one (for an extensive treatise, see Percival & Walden (1993)). Several methods have been traditionally used for power spectrum estimation in one-dimension. These include non-parametric methods like the periodogram, the lag-window estimators, Welch's overlapped segment averaging (Welch, 1967) and the Multitaper method (Thomson, 1982), and parametric methods like the maximum likelihood estimation. In this paper, we generalize the one-dimensional Multitaper method to two-dimensions and adapt it to handle real data with noise and masks on a two-dimensional flat Euclidean patch. We discuss its applications specifically in the case of CMB power spectrum estimation.

The most basic spectral estimation method is to take the square of the Fourier Transform (FT) of the observed data. Taking the FT of a finite segment of data is equivalent to convolving the underlying power spectrum with the power spectrum of a top-hat function. As the latter has substantial sidelobe power, it leads to spectra leakage and the resulting spectrum is highly biased. Most of the non-parametric methods for power spectrum estimation utilize some kind of a data taper (a smooth function that goes smoothly to zero at the edges of the observed segment) to minimize the effect of spectral leakage. Such smoothing reduces the bias in the estimator at the cost of lower spectral resolution. As the taper down-weights a fraction of the data, one is left with an effectively lower sample size. Since tapering also smooths in frequency space, it essentially leads to a loss of information which is reflected in the increased variance of the final estimate. The first attempt at ameliorating these disadvantages of using a data taper was addressed in a seminal paper by Thomson (1982) which laid down the basis of the Multitaper Method (MTM). The basic idea of MTM

is to apply multiple orthogonal tapers with optimal spectral concentration to minimize the loss of information due to tapering.

2.2.1 Notations

Throughout this paper, we will refer to spatial coordinates as the $\mathbf{x}$ space (this may be an angular coordinate in radians on the sky, or a comoving distance in h^{-1}Mpc, etc.) and the reciprocal space as the $\mathbf{k}$ space (which would be the multipole space ℓ, or the Fourier modes in h^{-1}Mpc, etc). The continuous Fourier Transform conventions adopted here are,

$$\tilde{F}(\mathbf{k}) = \int d^n\mathbf{x}\ F(\mathbf{x})\ \exp(-i\mathbf{k}\cdot\mathbf{x})\ \text{(forward)} \tag{2.1}$$

$$F(\mathbf{x}) = \int \frac{d^n\mathbf{k}}{(2\pi)^n}\ \tilde{F}(\mathbf{k})\ \exp(i\mathbf{k}\cdot\mathbf{x})\ \text{(inverse)}, \tag{2.2}$$

where n is the dimensionality of the space.

For a stationary process, $F(\mathbf{x})$ the power spectrum is defined as,

$$(2\pi)^n P(k) = \left\langle \tilde{F}^*(\mathbf{k})\tilde{F}(\mathbf{k}) \right\rangle . \tag{2.3}$$

2.2.2 1-D Multitaper Theory

Although power spectrum estimation for the CMB is an inherently two-dimensional problem, we will begin by discussing the multitaper theory in one dimension. This is because the essential features of the theory are easier to understand in one dimension and can be trivially generalized to higher dimensions.

We consider a stationary, stochastic, zero mean process $F(x)$ sampled at N discrete points, x_j sampled at regular intervals of size Δx. Let $P(k)$ be the true underlying power spectrum of the process. Our problem is to estimate $P(k)$ using the sample of size N.

The Nyquist frequency for the problem is given by $f_N = k_N/(2\pi) = 1/(2\Delta x)$ and the fundamental frequency by $f_0 = k_0/(2\pi) = 1/(N\Delta x)$. In the following, we will assume $\Delta x = 1$ for simplicity.

Let us contemplate windowing our data by some function $G(x)$, generating the product,

$$y(x_j) = G(x_j)F(x_j) \tag{2.4}$$

and taking the power spectrum of the windowed data as,

$$(2\pi)\hat{P}(k) \equiv \tilde{y}^*(k)\tilde{y}(k) = \left| \sum_{j=1}^{N} G(x_j)F(x_j)e^{-ikx} \right|^2 , \tag{2.5}$$

where $\tilde{y}$ is the Fourier transform of $y(x)$. The quantity $\hat{P}$ can be thought of as an estimator of $P(k)$, such that its ensemble average is related to $P(k)$ through

$$\left\langle \hat{P}(k) \right\rangle = \int_{-k_N}^{k_N} \frac{dk'}{(2\pi)} \Gamma(k-k')P(k'). \tag{2.6}$$

This means that $\hat{P}$ is an estimator of the true power spectrum convolved with a *spectral window function*,

$$\Gamma(k) = \left| \tilde{G}(k) \right|^2 . \tag{2.7}$$

If Γ could be designed such that $\Gamma(k) = (2\pi)\delta(k)$ then $\hat{P}$ would be an exact unbiased estimator of P. However, a function like G which is spatially limited in extent cannot be arbitrarily concentrated in the frequency space. If the window function is a top-hat, its power spectrum will be a sinc^2 function[4] with substantial sidelobes. This will lead to the aliasing of power on various scales, an effect known as spectral leakage or mode coupling. Mode coupling is specially damaging for a spectrum which is highly colored or structured.

The multitaper method (MTM) consists of finding a set of orthogonal window functions or tapers, which are maximally concentrated in some predetermined frequency interval. With the set of tapers, one can generate several approximately uncorrelated estimates of the power spectrum. This is superior to the plain Fourier Transform (Periodogram) because it not only attempts at remedying mode coupling errors but also helps decrease the uncertainty in the estimated power spectrum by generating independent realizations of the same power spectrum with information from different section of the data. We formulate the method below.

We desire a set of tapers, such that each of them is spatially limited, G_j $(j = 1, ..., N)$ and has its power $\Gamma(k)$ optimally concentrated in some frequency interval, $k \in [-2\pi W, 2\pi W]$,

[4]sinc refers to the *sinus cardinus* i.e. $\sin x/x$. Power spectrum of a two-dimensional top-hat window is a product of two sinc^2 functions.

with $W < f_N \equiv k_N/(2\pi)$. Here we have introduced the shorthand notation G_j for $G(x_j)$. Concentration is quantified by the following quantity,

$$\beta^2(W) = \frac{\int_{-2\pi W}^{2\pi W} \Gamma(k)dk}{\int_{-k_N}^{k_N} \Gamma(k)dk}. \tag{2.8}$$

which is basically the fractional power of the taper inside the desired interval. Remembering that,

$$\tilde{G}_k = \sum_{j=1}^{N} G_j e^{-ikx_j}, \tag{2.9}$$

the above equation can be re-written as,

$$\beta^2(W) = \sum_{j'=1}^{N}\sum_{j=1}^{N} G_j^* \frac{\sin[2\pi W(j-j')]}{\pi(j-j')} G_{j'} \Bigg/ \sum_{j=1}^{N} |G_j|^2 \tag{2.10}$$

It is easy to see that the sequence G_j that will maximize $\beta(W)$ must satisfy,

$$\sum_{j'=1}^{N} \frac{\sin[2\pi W(j-j')]}{\pi(j-j')} G_{j'} = \lambda_\alpha(N,W) G_j, \tag{2.11}$$

for $j = 1, ..., N$. This can be immediately recognized as an eigenvalue problem,

$$\mathbb{A}\mathbf{G} = \lambda_\alpha(N,W)\mathbf{G} \tag{2.12}$$

where $\mathbb{A}$ is the $N \times N$ Toeplitz matrix,

$$\mathbb{A}_{jj'} = \frac{\sin[2\pi W(j-j')]}{\pi(j-j')} \tag{2.13}$$

and $\mathbf{G}$ is the vector, index limited from $j = 1$ to $j = N$ which has the highest concentration in the frequency interval $[-W, W]$. Here α denotes the indices of the different eigenvalues of the problem. The solution to this eigenvalue problem is well known (Slepian, 1978). There are N nonzero eigenvalues of the problem denoted by λ_α ($\alpha = 0, 1, ..., (N-1)$) with corresponding eigenvectors $\mathbf{v}^\alpha$. The elements of each of the N eigenvectors consist of a finite subset of the discrete prolate spheroidal sequence (DPSS). The zeroth eigenvector $\mathbf{v}^0(N,W)$ which has the highest eigenvalue λ_0 is composed of the zeroth order DPSS, the eigenvector $\mathbf{v}^1(N,W)$ having eigenvalue $\lambda_1 < \lambda_0$ is composed of first order DPSS sequence and so on.

Some salient properties of the N eigenvectors and eigenvalues are as follows,

1. The eigenvalues are bounded by 0 and 1:

$$0 < \mathbf{v}^{\alpha} < 1.$$

2. The eigenvectors are orthogonal and can be standardized so that they are orthonormal,

$$\mathbf{v}^{\alpha} \cdot \mathbf{v}^{\beta} = \delta_{\alpha\beta}$$

3. The eigenvectors form a basis for an N-dimensional Euclidean space.

4. Usually the eigenvectors are ordered according to decreasing eigenvalues. The first $2NW-1$ eigenvalues are close to unity (most concentrated) and the eigenvalues rapidly fall to zero thereafter. This behavior is illustrated in Fig. 2.1. The number $2NW-1$ is often referred to in the MTM literature as the *Shanon Number*.

One-dimensional DPSS taper generation algorithms are usually included in standard signal processing softwares (e.g. the `dpss` module of Matlab). For the purpose of this paper, we used a Fortran 90 implementation of the original algorithm by Bell et al. (1993). Examples of DPSS tapers and their corresponding spectral window functions are displayed in Fig 2.2, where the gradual worsening of the leakage properties of the tapers are apparent.

The Fourier transforms of the tapers,

$$\tilde{v}^{\alpha}(k) = \sum_{j} v^{\alpha}(x_j) e^{-ikx_j} \tag{2.14}$$

also have the interesting properties:

1. They are orthonormal over the frequency range $-k_N < k < k_N$,

$$\int_{-k_N}^{k_N} \frac{dk}{2\pi} \tilde{v}^{\alpha *}(k) \tilde{v}^{\beta}(k) = \delta_{\alpha\beta}.$$

2. They are also orthogonal over the frequency domain $-2\pi W < k < 2\pi W$,

$$\int_{-2\pi W}^{2\pi W} \frac{dk}{2\pi} \tilde{v}^{\alpha *}(k) \tilde{v}^{\beta}(k) = \lambda_{\alpha} \delta_{\alpha\beta}. \tag{2.15}$$

This means that the functions $\tilde{\mathbf{v}}^{\alpha}/\sqrt{\lambda_{\alpha}}$ form an orthonormal set on the inner interval $-2\pi W < k < 2\pi W$.

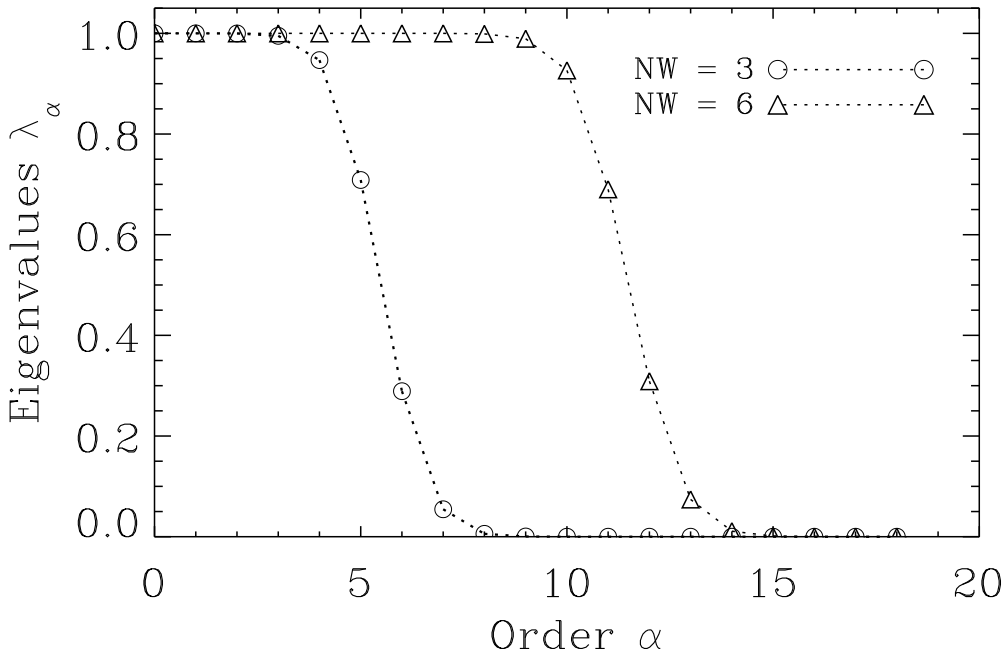

Figure 2.1: Eigenvalues corresponding the different orders of DPSS tapers. Two cases with $NW = 3$ and 6 are shown for $N = 50$. Spectral concentration of the tapers rapidly worsen beyond $\alpha = 2NW - 1$.

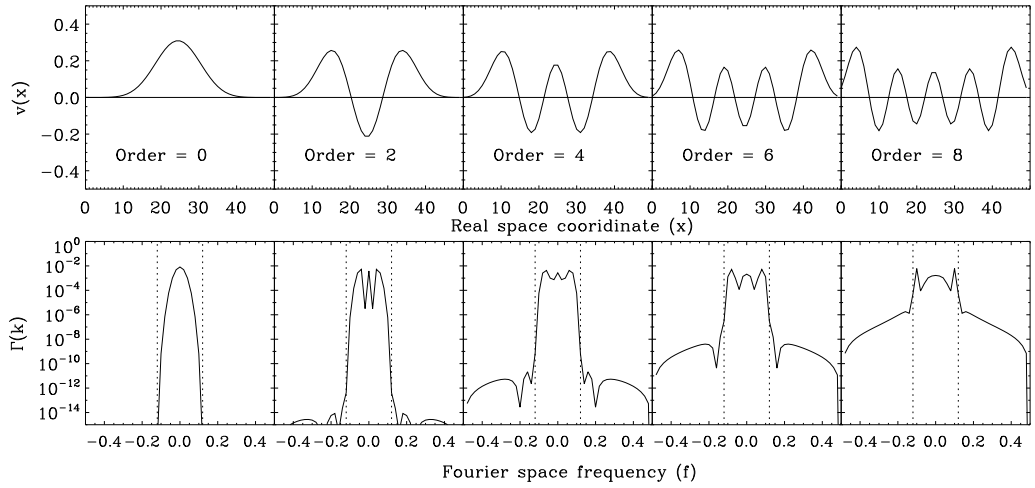

Figure 2.2: Examples of DPSS tapers and the corresponding spectral window functions for the case $N = 50$ and $NW = 6$. *Upper panel:* Real space form of the tapers of orders 0, 4, 6 and 8. *Lower panel:* The spectral window functions corresponding to the tapers in the upper panel. For simplicity, the window functions are shown only in the range $-3W < f < 3W$ of frequency. The vertical dotted lines denote the edges of the bandwidth $(-W, W)$ within which the tapers are designed to be optimally concentrated. Tapers are ordered such that spectral leakage progressively increases for tapers of higher order.

Having generated the *eigentapers*, we can form M approximately uncorrelated estimators of the power spectrum with the first M eigenvectors having the best concentration,

$$(2\pi)\hat{P}^{\alpha}(k) = \left| \sum_{j=1}^{N} v_j^{\alpha} F_j e^{-ikx_j} \right|^2 \tag{2.16}$$

where $\alpha = 0, ..., M-1$.

Then we can form a weighted mean of the tapered power spectra, often called the *eigenspectra*, to generate the final estimate of $P(k)$, the simplest form of which is,

$$P^{\mathrm{MTM}}(k) = \frac{\sum_{\alpha=0}^{M-1} \lambda_{\alpha} \hat{P}^{\alpha}(k)}{\sum_{\alpha=0}^{M-1} \lambda_{\alpha}} \tag{2.17}$$

It can be shown that this is the optimal way of estimating P in the case where the process is white noise. For colored spectra, a more sophisticated approach is required, which leads to the adaptive multitaper method (AMTM) to be discussed in the following section.

The important point to note here is that the MTM or variants of it, aim to restore the information lost to a single taper algorithm by weighting different parts of the data by an

orthogonal set of tapers, thereby reducing the variance in the final estimate. Lower variance comes at the cost of decreased spectral resolution. One should bear in mind that the choice of the resolution W is completely dependent on the analyst. Remembering that the number of useful tapers is $(2NW - 1)$ and a better spectral resolution, i.e. smaller W means that there will be fewer tapers to work with. The choice of W will in most cases be dictated by the type of and the features in the power spectrum being estimated.

2.2.3 Adaptive MTM

As noted above, if the underlying spectrum is white and only modest spectral resolution is needed in the analysis, many eigenspectra can be simply combined with scalar weights to get a good estimate of the true spectrum. However, this is not the case for spectra which are colored and have large dynamic range. For example, the Cosmic Microwave Background (CMB) power spectrum C_ℓ falls like ℓ^{-4} beyond $\ell \sim 1000$. In cases such as this, only the first few tapers are good at avoiding aliasing of power due to mode coupling. As more and more tapers are used, the estimated power spectrum gets more and more biased.

The adaptive multitaper method (AMTM) aims at mitigating this problem, thereby allowing the use of a larger number of tapers even for a colored spectrum. In the following we briefly sketch the AMTM method.

According to the Cramer spectral representation of a stationary process (Cramer, 1940), a stationary zero mean process can be represented as,

$$F(x) = \int_{-k_N}^{k_N} e^{ikx} dZ(k) \tag{2.18}$$

for all x, where dZ is an orthogonal incremental process (Doob, 1963; Priestly, 1988). The random orthogonal measure $dZ(k)$ has the properties,

$$\langle dZ(k) \rangle = 0; \ \left\langle |dZ(k)|^2 \right\rangle = P(k)dk. \tag{2.19}$$

where $P(k)$, as before, is the true underlying spectrum.

The Fourier transform of the data weighted by an eigentaper can be written as,

$$\tilde{y}^{\alpha}(k) = \sum_{j=1}^{N} v^{\alpha}(x_j) F(x_j) e^{-ik\,x_j} \tag{2.20}$$

$$= \int_{-k_N}^{k_N} \tilde{v}^{\alpha}(k-k') dZ(k') \tag{2.21}$$

using equation (2.18). Note that this contains information from the entire Nyquist range.

Now consider the case where the signal $F(x)$ is convolved with a perfect bandpass filter from $k - 2\pi W$ to $k + 2\pi W$ to yield the unobservable yet perfect eigencomponent,

$$\tilde{\mathcal{Y}}^{\alpha}(k) = \int_{k'=k-2\pi W}^{k+2\pi W} \frac{\tilde{v}^{\alpha}(k-k')}{\sqrt{\lambda_k}} dZ(k') \tag{2.22}$$

which contains information only from the interval $(-2\pi W, 2\pi W)$. Note that in accordance with equation (2.15) we have used the correct orthonormal form for FT of the tapers inside this interval.

The quantity $\tilde{\mathcal{Y}}(k)$, although fictitious in the sense that it cannot be computed from the data, has the desirable property that,

$$\left\langle \left| \tilde{\mathcal{Y}}(k) \right|^2 \right\rangle = \int_{k'=k-2\pi W}^{k+2\pi W} \left[\frac{|\tilde{v}^{\alpha}(k-k')|}{\sqrt{\lambda_\alpha}} \right]^2 P(k') dk' \tag{2.23}$$

i.e. it is the unbiased estimator of the true power spectrum smoothed by a strict bandpass filter of width $4\pi W$. Therefore, in a multitaper setting, when combining different tapers with weights, the weights should be chosen such that the eigenspectrum obtained by each of the weighted tapers is as close as possible to this ideal estimate. This forms the basis of the AMTM, where one replaces the scalar weights by frequency dependent weight functions $b_\alpha(k)$ which minimize the mean squared error,

$$\mathrm{MSE}^{\alpha}(k) = \left\langle \left| \tilde{\mathcal{Y}}^{\alpha}(k) - b_\alpha(k) \tilde{y}^{\alpha}(k) \right|^2 \right\rangle . \tag{2.24}$$

The minimization leads to the following expression for b_α,

$$b_\alpha(k) = \frac{\sqrt{\lambda_\alpha} P(k)}{\lambda_\alpha P(k) + (1-\lambda_\alpha)\sigma^2} \tag{2.25}$$

where, $\sigma^2 = \int_{-k_N}^{k_N} \frac{dk}{2\pi} P(k) = \mathrm{var}\{x_k\}$, the variance of the map, using Parseval's theorem.

With this the minimum mean square error becomes,

$$\mathrm{MSE}^{\alpha}(k) \simeq \frac{P(k)(1-\lambda_{\alpha})\sigma^2}{\lambda_{\alpha}P(k)+(1-\lambda_{\alpha})\sigma^2}, \tag{2.26}$$

and the best estimate of the power spectrum has the form,

$$\hat{P}^{\mathrm{AMTM}}(k) = \frac{\sum_{\alpha=0}^{M-1} b_{\alpha}^2(k)\hat{P}^{\alpha}(k)}{\sum_{\alpha=0}^{K-1} b_{\alpha}^2(k)} \tag{2.27}$$

where $\hat{P}^{\alpha}$ is the single taper power spectrum estimate with the α^{th} taper i.e. the eigenspectrum of order α. In case of a white noise spectrum $P(k)=\sigma^2$, and therefore $b_{\alpha}(k)=\sqrt{\lambda_{\alpha}}$, which gives us the formula equation (2.17) for the simple MTM. Also, in this case $\mathrm{MSE}^{\alpha} = (1-\lambda_{\alpha})\sigma^2$. This shows again that for white noise, for which the first $2NW-1$ tapers have eigenvalues close to unity, the mean squared error is negligible.

Note that the estimation of the power spectrum requires the evaluation of the optimal value for the weights $b^{\alpha}(k)$, which assumes knowledge of the true power spectrum. But the latter is precisely what we are trying to estimate. Therefore, this method has to be implemented iteratively according to the following steps,

1. We use the first one or two tapers (having the least spectral leakage) to form a first estimate of the power spectrum $P(k)$ via equation (2.17).

2. We use equation (2.25) to estimate the weights $b_{\alpha}(k)$.

3. With the b_{α}'s estimated, we use equation (2.27) with $M \lesssim 2NW-1$ tapers to get the second estimate of the power spectrum.

4. Using this new estimate, re-evaluate the weights $b_{\alpha}(k)$ and repeat steps 2-4.

In the following, we will generalize the AMTM to two dimensions.

2.2.4 AMTM in two dimensions

So far we have only considered one-dimensional tapers. In the signal processing literature, generalizations of the multitaper method to higher dimensions have not been widely discussed. Some of the early works include Barr, D. L. et al. (1988); Bronez (1988); Liu & van

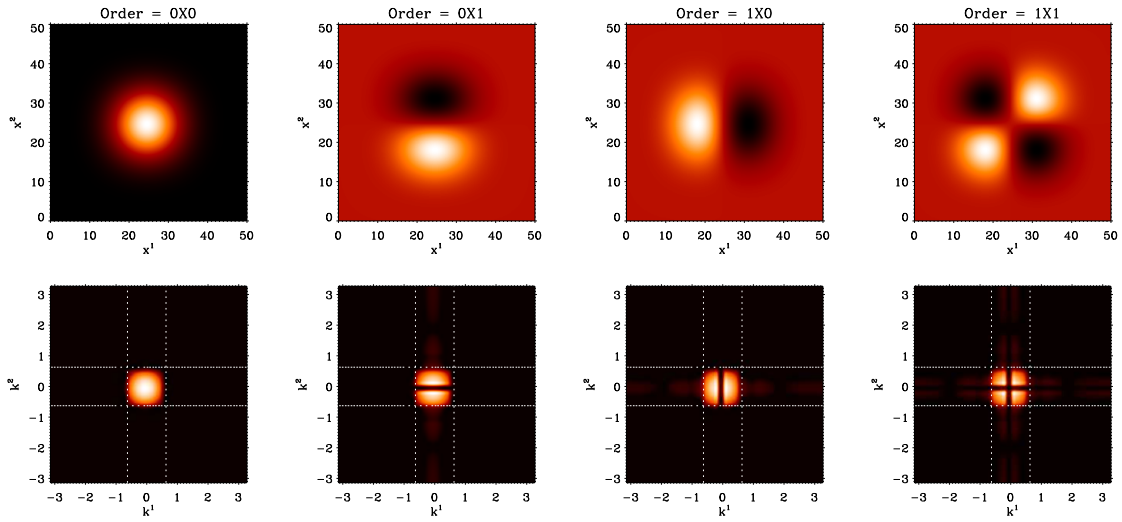

Figure 2.3: *Top panel*: The first 4 two-dimensional tapers on a N×N grid with $N = 50$ and $NW = 5$. The order of the one-dimensional tapers corresponding to each taper is indicated on the top. *Bottom panel*: The logarithm of the spectral window functions $\Gamma(k^1, k^2)$, corresponding to the tapers on the upper panel. The color scale on the lower panel are standardized to be $(10^{-30}, 1)$ times the maximum in each plot. The white dotted lines represent the location of $\pm 2\pi W$ wavenumbers.

Veen (1992). Relatively recently, straightforward generalizations of the method to higher dimensional euclidean spaces (Hanssen, 1997) and to patches on the surface of the sphere (Wieczorek & Simons, 2005; Dahlen & Simons, 2007; Simons et al., 2004) have been formulated. In view of the upcoming CMB experiments (that will map the sky on small scales at high resolution), we will be mostly interested in the power spectrum estimation on regularly sampled two-dimensional flat spaces like a projection of a small patch on the sky. As such we will discuss the 2-D extension of the multitaper method as discussed in Hanssen (1997).

Two-dimensional tapers are constructed from outer products of one-dimensional tapers. We assume a two-dimensional map spanned by the coordinates (x^1, x^2) . The data should be sampled regularly, but the sampling intervals (pixel sizes), Δx^i, and the number of pixels in each direction, N_i, can be different $(i = 1, 2)$. Let us relabel the one-dimensional taper of the previous section as $\mathbf{v}^{\alpha;N}$ where the extra superscript denotes the number of pixels in a given direction. Then a two-dimensional taper of order $(\alpha_1; \alpha_2)$ and size $N_1 \times N_2$ can be

constructed out of the outer product of two one-dimensional tapers:

$$\mathbb{V}^{(\alpha_1\alpha_2;N_1N_2)} = \mathbf{v}^{(\alpha_1,N_1)} \left[\mathbf{v}^{(\alpha_2,N_2)}\right]^T, \tag{2.28}$$

where we have treated $\mathbf{v}$ as a column vector. The spectral concentration eigenvalue of a two-dimensional taper, is easily shown to be the product of the eigenvalues of the one-dimensional tapers out of which the former is constructed:

$$\lambda_{(\alpha_1\alpha_2;N_1N_2)} = \lambda_{\alpha_1,N_1}\lambda_{\alpha_2,N_2}. \tag{2.29}$$

Two-dimensional tapers constructed in this way inherit most of the properties of one-dimensional tapers such as orthogonality on the sample plane, and optimal spectral concentration and orthonormality in the frequency plane. The two-dimensional power spectrum estimator corresponding to these tapers is defined, similar to the one-dimensional case, as a weighted sum of approximately independent tapered power spectra

$$P^{\mathrm{AMTM}}(k_1,k_2) = \frac{\sum_{\alpha_1,\alpha_2} b^2_{(\alpha_1\alpha_2)}(k_1,k_2)\hat{P}^{(\alpha_1\alpha_2)}(k_1,k_2)}{\sum_{\alpha_1,\alpha_2} b^2_{(\alpha_1\alpha_2)}}, \tag{2.30}$$

where we have dropped the N_1N_2 portion of the labels for simplicity. Note that in the above formula the weights $b_{(\alpha_1\alpha_2)}$ depend on the eigenvalues $\lambda_{(\alpha_1\alpha_2)}$ and are given by an equation analogous to equation (2.25) and are to be estimated iteratively. The quantity $(2\pi)^2\hat{P}^{(\alpha_1\alpha_2)}(k_1,k_2)$ is the eigenspectrum of order $(\alpha_1\alpha_2)$ and is given by

$$\hat{\mathbb{P}}^{(\alpha_1\alpha_2)} = \left|\mathrm{FT}\left[\mathbb{V}^{(\alpha_1\alpha_2;N_1N_2)}\mathbb{M}^T\right]\right|^2, \tag{2.31}$$

where $\mathbb{M} = \{M(x_i,x_j)\}$ is the two-dimensional map, the power spectrum of which is being estimated.

We will introduce a bit of notation at this point. We will designate the two parameters that control the multitaper method as:

- N_{tap}: The number of tapers used. Its value will be written in the form M^2, where M denote the number of one-dimensional tapers. For example if 2 one-dimensional tapers are used to create 4 two-dimensional tapers via outer products, then we will quote $N_{tap} = 2^2$.

- N_{res}: We will use this as the shorthand for the resolution parameter NW. For example, $N_{res} = 3$ will mean that the half-bandpass chosen for generating the tapers is three times the fundamental frequency.

2.2.5 Statistical Properties

Statistical distribution of the power spectra of a Gaussian random field realized on a map with periodic boundary conditions, such as a full sky CMB field, can be described in terms of the simple analytic distributions. This property stems from the fact that each Fourier-mode (or spherical harmonic component) of such a map is a statically independent quantity. On a finite patch of the sky or for any map with a non-periodic boundary condition, these modes get entangled due to the convolution with the window, and are no longer amenable to such simple descriptions. As we will discuss in this subsection, the multitaper method approximately restores many of these nice properties of random fields on a finite patch, and makes the statistical properties of the spectral estimators describable via simple and intuitive analytic expressions.

Most of the statistical properties of the different spectral estimators that we have discussed so far stem from the basic result that for most stationary processes with a power spectrum $P(k)$ that is continuous over the interval $[-k_N,\ k_N]$, the simple FFT power spectrum (periodogram) $P^{PM}(k)$ is distributed as,

$$\hat{P}^{PM}(k) \stackrel{\mathbf{d}}{=} \begin{cases} P(k)\chi^2_2/2, & \text{for } 0 < k < k_N; \\ P(k)\chi^2_1, & \text{for } k = 0 \text{ or } k = k_N, \end{cases} \tag{2.32}$$

asymptotically as $N \to \infty$. Here $\stackrel{\mathbf{d}}{=}$ means "equal in distribution", which means that the statement "$X \stackrel{\mathbf{d}}{=} a\chi^2_\nu$" is equivalent to saying that the random variable X has the same distribution as a chi-square random variable with ν degrees-of-freedom (dof) that has been multiplied by a constant a. For a Gaussian white noise process the above result is exact for any N. Also, for the asymptotic case, the power spectra for two different frequencies k and k' are uncorrelated. Although these results are true for asymptotically large N, in

a finite N case, they approximately hold for the $N/2+1$ independent Fourier frequencies $k_j = (2\pi j)/(N\Delta x)$, if N is large enough.

Using the above result, it is possible to predict the approximate distribution of an AMTM spectrum estimator equation (2.30). Using an equivalent degrees-of-freedom argument (see appendix 2.A for details), it can be shown that for $N \to \infty$,

$$P^{\mathrm{AMTM}}(\mathbf{k}) \overset{\mathbf{d}}{=} \frac{\left\langle P^{\mathrm{AMTM}}(\mathbf{k}) \right\rangle}{\nu(\mathbf{k})} \chi^2_\nu \tag{2.33}$$

where,

$$\nu(\mathbf{k}) = \frac{2\left(\sum_{\alpha_1,\alpha_2} b^2_{(\alpha_1\alpha_2)}(\mathbf{k})\right)^2}{\sum_{\alpha_1,\alpha_2} b^4_{(\alpha_1\alpha_2)}(\mathbf{k})}. \tag{2.34}$$

Therefore, for finite N, it is reasonable to expect that the AMTM power spectrum at each pixel is approximately distributed as $\left\langle P^{\mathrm{AMTM}} \right\rangle \chi^2_\nu/\nu$ with ν given by the above equation. Note that in the case of MTM, $b^2_{\alpha_1\alpha_2} = \lambda_{\alpha_1\alpha_2}$. If we are only using tapers with eigenvalues close to unity, then $\nu(\mathbf{k}) \simeq 2M$, M being the total number of tapers used.

Now we turn to the approximate form of the distribution for the power spectrum after it is binned in annular rings in $\mathbf{k}$ space, which we denote by $P^B(k_b)$,

$$P^B(k_b) = \frac{1}{N_b} \sum_{i,j \in b} P^{\mathrm{AMTM}}(k_i, k_j) \tag{2.35}$$

where the sum is over all pixels that fall inside bin b and N_b is the number of observations in that bin. Using a similar argument as before, it can be shown (see appendix 2.A) that,

$$P^B(k_b) \overset{\mathbf{d}}{=} \frac{\left\langle P^B(k_b) \right\rangle}{\nu_b} \chi^2_{\nu_b} \tag{2.36}$$

where the degree-of-freedom, ν_b is given by,

$$\frac{1}{\nu_b} \simeq \frac{2N^2_{res}}{N^2_b} \sum_{i,j \in b} \frac{1}{\nu(k_i, k_j)}, \tag{2.37}$$

with $\nu(\mathbf{k})$ given by equation (2.34). If the degree-of-freedom variable is also slowly varying, then this implies $\nu_b = N_b/(2N^2_{res})\ \nu(|\mathbf{k}| \simeq k_b)$, which is the expected result for the sum of $N_b/(2N^2_{res})$ independent identically distributed χ^2_ν variables. Note that the appearance of the N^2_{res} factor essentially arises from the fact that AMTM significantly correlates N^2_{res}

nearby pixels, and therefore only $N_b/(2N_{res}^2)$ "super-pixels" are approximately statistically independent.

In case of the periodogram, $\nu = 2$ and $N_{res} = 1$, so that $\nu_b \simeq N_b$. In case of MTM with M tapers with good leakage properties, $\nu \simeq 2M$ and therefore, $\nu_b \simeq N_b M/N_{res}^2$.

2.3 Application to the ideal CMB map

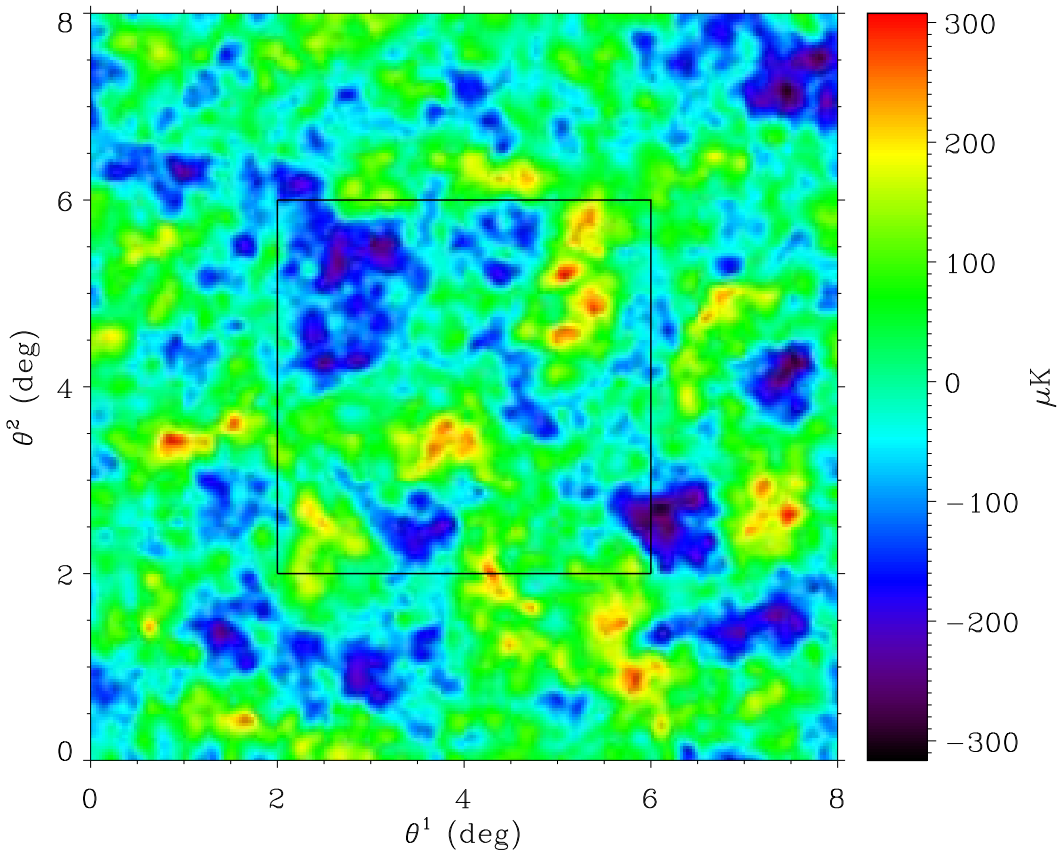

Figure 2.4: One realization of the CMB map on a 192×192 pixel grid. The physical size is 8 degrees on a side. Estimation of the power spectrum is done on the 4 degree $\times$ 4 degree subarea indicated by the rectangle. The color scale represents temperature fluctuations in micro-Kelvin.

In this section, we will illustrate the multitaper method by applying it to flat-sky cosmic microwave background (CMB) maps. We shall assume the maps to be pure CMB without noise or masks and with uniform weight. We also assume a square map with square pixels for simplicity, although all the results shown hold for non-square maps and/or non-square pixels.

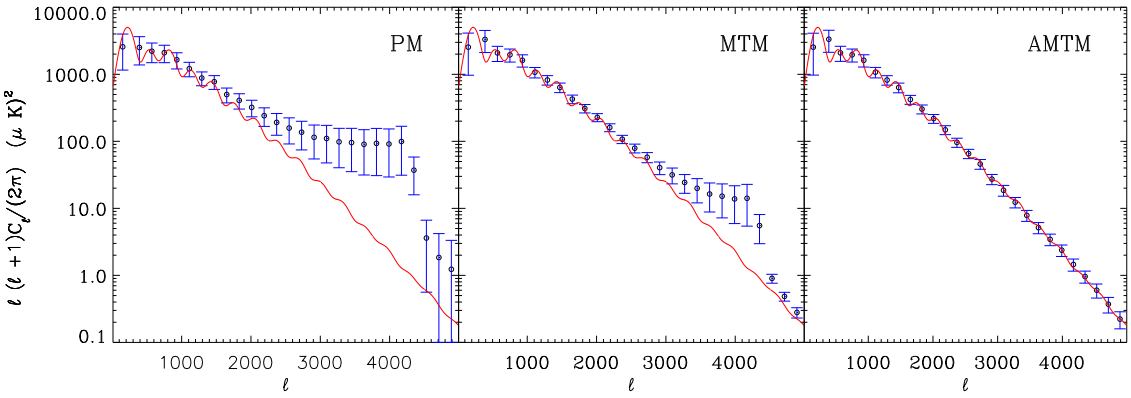

Figure 2.5: Comparison of the simple periodogram method (labeled PM), the eigenvalue weighted multitaper (labeled MTM) and the adaptive multitaper (labeled AMTM) methods for estimating the power spectrum of a CMB map. In each plot, the continuous line represents the theory power spectrum used as an input for the Monte Carlo simulations. The open circles represent the mean values in each ℓ bin, averaged over 5000 realizations, while the vertical lines represent the 2σ spread. The bin width for this figure was $\Delta\ell = 180$. For the MTM and AMTM methods $N_{tap} = 3^2$ tapers with $N_{res} = 2$ were used (see text for details). Note that the power spectra for the multitaper methods appear smoothed because they are convolved with the window function of an effective taper. Standard decorrelation techniques, like the MASTER algorithm (Hivon et al., 2002) can be employed to de-bias and deconvolve all the above power spectra, but in the first two cases, where the mode-coupled power spectra are biased, decorrelation leads to bigger uncertainties in the deconvolved power spectra (see § 2.5).

We adopt a deliberate change of notation at this point to make the following sections more compatible with existing CMB literature. Since we will dealing with angular coordinates on the sky, we call the real space variable $\boldsymbol{\theta}$ rather than $\mathbf{x}$. We also call the dual Fourier space, the $\boldsymbol{\ell}$ space, instead of the $\mathbf{k}$ space. The latter is motivated by the fact that the full sky CMB power spectra are expressed in terms of multipole moments, which are denoted by ℓ, and the $\mathbf{k}$ vector is the correct generalization of the ℓ modes in the flat-sky

case. We will also denote the power spectrum $P(k)$ by C_ℓ.

We generate the CMB maps as Gaussian random realizations from a theoretical power spectrum C_ℓ. In order to simulate the effect of non-periodic boundary conditions we first generate larger maps from which the desired region is extracted. In the present example, we generated 5000 realizations of 192×192 pixel CMB map having a physical size of 8 degrees on a side. This implies that the sampling intervals (i.e. pixel scales) along either axes is $\delta\theta = 2.5'$. We extract a 96×96 pixel 4 degree square sub-map from the center of each such realization and perform the power spectral estimation on this sub-area (see Fig. 2.4). Given the physical size and the number of pixels, one finds the Nyquist and fundamental values of ℓ to be $\ell_{Nyq} = \pi/(\Delta\theta) = 4320$ and $\ell_{fund} = (2\pi)/4^\circ = 90$. Therefore, if we choose a resolution parameter of $N_{res} = 2$ the half-bandwidth outside which spectral leakage is minimized is $W_\ell = 180$.

We perform the straight FFT or periodogram (labeled PM), MTM and AMTM power spectrum estimation on 5000 random realizations of the CMB map. The results are shown in Fig 2.5. These plots show the mean power spectrum binned uniformly in ℓ in bins of $\Delta\ell = 180$. The error bars correspond to the 2σ spread in the distribution of their values. Two features are immediately apparent from this figure. First, it shows that the PM has significant spectral leakage and produces a power spectrum which is highly biased. Although the eigenvalue weighted MTM is better in this respect, it still suffers from significant bias at high ℓ's because the higher order tapers cannot guard efficiently against spectral leakage. The AMTM seems to do very well in minimizing spectral leakage and producing an approximately unbiased estimate of the input power spectrum. Second, the 2σ spread in the uncertainty of the binned value in the PM case is much higher than the corresponding spread for the AMTM. This is one of the main reasons for performing tapered power spectrum estimation with multiple tapers, as has been stressed before. As discussed in § 2.5 this property becomes extremely important when the tapered power spectra are decorrelated via a MASTER-like (Hivon et al., 2002) algorithm. The nearly unbiased nature of the AMTM power spectrum translates to errorbars in the deconvolved spectrum which are

several factors smaller than those obtained from a periodogram in the large ℓ regime.

Now, we will compare the distributions of the various power spectrum estimators with the theoretical expectations of section 2.2.5. For this purpose, we choose three multipoles $\ell \sim 1000, 2000, 3000$ at which we study both the single pixel and the binned probability distributions. The reason for choosing these three numbers is that the first multipole is an example where all three methods are approximately unbiased, the second multipole is a case where the PM is biased but the MTM and AMTM are almost unbiased, while the third multipole represents a regime where only the AMTM is close to an unbiased estimate.

For the single pixel case, we choose three pixels (ℓ^i, ℓ^j) on the $\boldsymbol{\ell}$-space map, such that values of $|\boldsymbol{\ell}|$ are close to the three multipoles as described above. We store the values of C_ℓ realized in the 5000 Monte Carlo simulations in these pixels, and draw up the probability distribution of the quantity $\ell(\ell+1)C_\ell/(2\pi)$ from these values, for each of the three methods. The results are shown in Fig 2.6. In the top panel, we show the results of the same experiment that was used to generate Fig. 2.5, i.e. with $N_{res} = 2.0$ and $N_{tap} = 3^2$. For the leftmost plot, all three methods of power spectrum estimation are approximately unbiased. The MTM and AMTM methods are almost identical here, because the spectrum does not have a large local slope at this multipole so that even in the adaptive method, the higher order tapers do not need to be down-weighted to reduce spectral leakage. Therefore, the equivalent degrees-of-freedom come out to be the same and $\simeq 2N_{tap} = 2 \times 3^2 = 18$, as expected for a white spectrum from equation (2.34). For the middle plot, the multipole ℓ is such that the local spectrum is moderately colored and spectral leakage for a periodogram becomes apparent in the biased estimate of the mean power spectrum it generates, as indicated by the dashed vertical line. The AMTM remains approximately unbiased while the MTM is only slightly biased, but the equivalent degrees-of-freedom for AMTM is now lower than that of the MTM method. This is expected because to reduce spectral leakage the weights associated with the higher order tapers have been reduced in the AMTM spectrum, thereby lowering the degrees-of-freedom. This trend continues to higher multipoles, and as shown in the rightmost plot of in the figure, the spectral leakage is kept at a minimum only

in the AMTM power spectrum by heavily down-weighting the higher order tapers, while both MTM and PM become highly biased. An important point to note here is that not only does AMTM minimize the spectral leakage (and hence bias) but it also takes advantage of multiple tapers by reducing the error in the estimate. This is most easily seen by comparing the width of the distributions of AMTM spectra against that of the PM spectra. The lower panel of Fig. 2.6 essentially shows the same features but for $N_{res} = 3.0$ and $N_{tap} = 5^2$. A comparison of the upper and lower panels also illustrate how by using more tapers the uncertainty in the power spectrum can be reduced. We would like to remind the reader once again here that the number of usable tapers depend on the spectral resolution chosen - poorer spectral resolution (in this example $N_{res} = 3$ vs. 2) allows the use of more tapers ($N_{tap} = 5$ vs. 3) and consequently an estimate with lower error.

Now, we turn to the distribution of the bandpowers C_b, i.e. the mean power spectrum in annular bands in the $\boldsymbol{\ell}$ space. This is illustrated in Fig. 2.7. The top two panels correspond to the same multitaper parameters as in Fig. 2.6, binned uniformly in $\boldsymbol{\ell}$ space with bins of width $\Delta\ell = 180$, while in the third panel we show the case for another experiment with $N_{res} = 4.0$ and $N_{tap} = 4$ binned at $\Delta\ell = 360$. The curves plotted over the points are the approximate theoretical distributions expected from equation (2.37). We note that the theoretical curves are always a good fit for the AMTM method. This is mainly because of the fact that the AMTM is approximately unbiased at all multipoles, while the MTM or PM become biased except at the lowest multipoles. Since near-unbiasedness was an assumption adopted in deriving the binned distributions, the latter two methods suffer from mismatch with theory wherever they are highly biased. For the $N_{res} = 4.0$ case, we chose a bin width of 360 so as to make it large enough to avoid splitting a super-pixel between bins. Also, note that the distribution of the binned power spectra are close to Gaussian, an expected result, as binning essentially involves combining many variables with almost identical distributions.

Next, we investigate the covariance between different bins, in order to study how the bandpowers are correlated with each other. We define the scaled covariance matrix,

$$\mathcal{C}_{ab} = \frac{C_{ab}}{\sqrt{C_{aa}C_{bb}}} \tag{2.38}$$

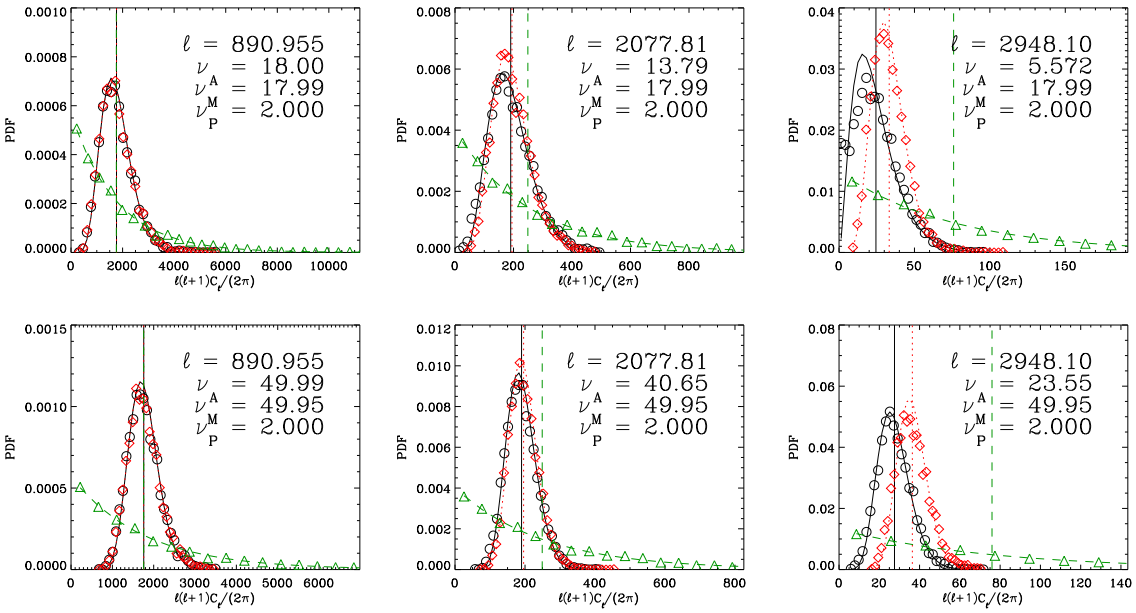

Figure 2.6: Comparison of the probability distributions of the estimated power spectrum at three points (pixels) in the two-dimensional Fourier ($\boldsymbol{\ell}$) space. From left to right, these points are $(\ell^1, \ell^2) = (630, 630)$, $(1980, 630)$ and $(2880, 630)$, for which the modulus ℓ has been indicated in each figure. *Upper Panel:* Power spectrum estimation with $N_{res} = 2.0$ and $N_{tap} = 3^2$. The open circles (black), the diamonds (red) and the triangles (green) indicate the probability distribution of the quantity $\ell(\ell+1)C_\ell/(2\pi)$ as estimated via the AMTM, MTM and PM methods from 5000 Monte Carlo simulations, respectively. The respective approximate theoretical forms as discussed in § 2.2.5 are over-plotted as the continuous curve (black), the dotted curve (red) and the dashed curve (green) for each of the methods. The mean degree of freedom of the chi-square for each method is also indicated as ν_A for AMTM, ν_M for MTM and ν_P for the periodogram, PM. Each curve is also accompanied by a vertical line of the same style (and color) representing the mean value obtained from the Monte Carlo simulations. In each figure, the continuous (black) vertical line corresponding to the mean of the AMTM method, is also the value closest to the true power spectrum. It is actually the unbiased value of the pseudo power spectrum (see § 2.5). *Lower Panel:* Same as above but with $N_{res} = 3.0$ and $Ntap = 5^2$.

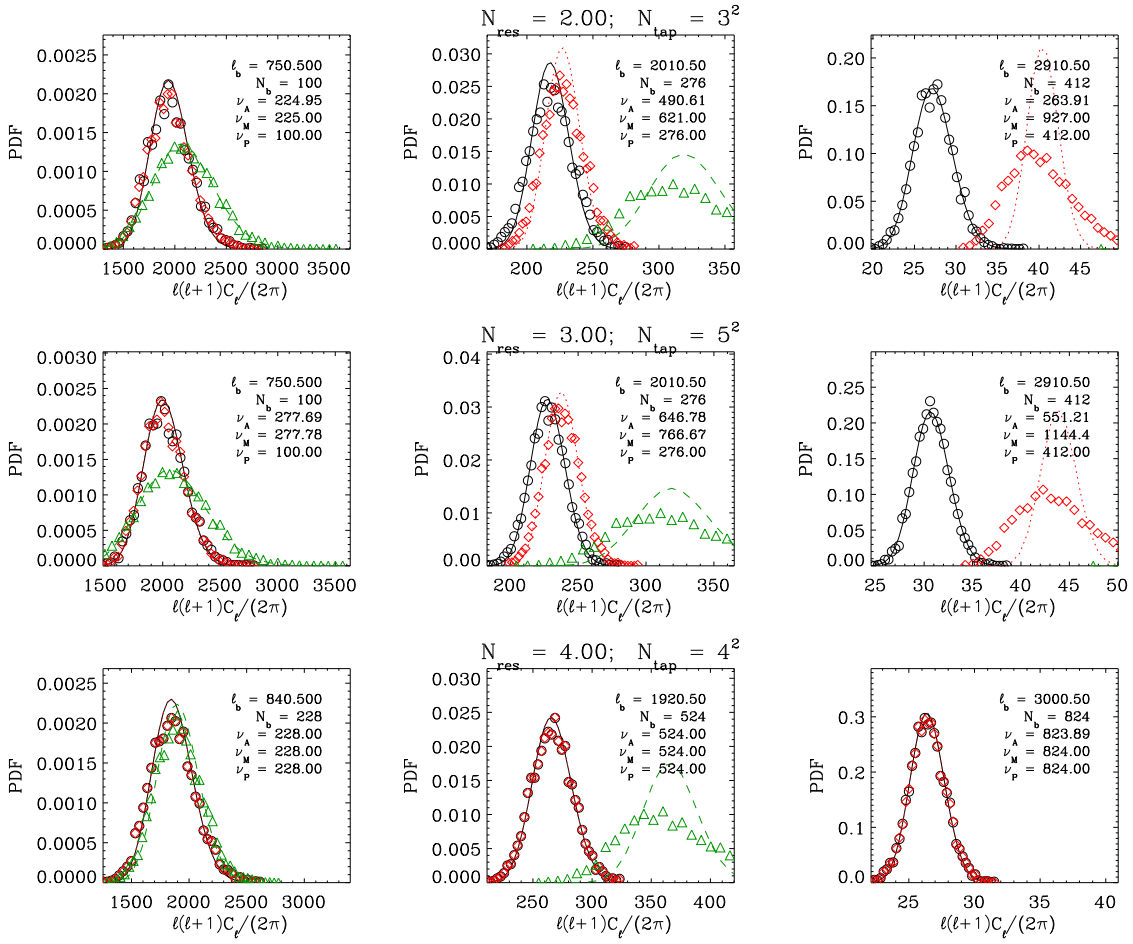

Figure 2.7: Comparison of the probability distributions of the estimated power spectrum in bins. Each panel is for a different combination of the N_{res} and N_{tap} as indicated on the top of the middle figure. The open circles (black), the diamonds (red) and the triangles (green) indicate the probability distribution of the quantity $\ell(\ell+1)C_\ell/(2\pi)$ in each bin as estimated via the AMTM, MTM and PM methods from 5000 Monte Carlo simulations, respectively. The respective approximate theoretical forms as discussed in § 2.2.5 (see eq. equation (2.37)) are over-plotted as the continuous curve (black), the dotted curve (red) and the dashed curve (green) for each of the methods. The mean degree of freedom of the chi-square for each method is also indicated as ν_A for AMTM, ν_M for MTM and ν_P for the periodogram, PM. The number of pixels in each bin is also indicated as N_b. Note that the periodogram is absent in each of the rightmost plots, as it is highly biased and lies outside the range plotted.

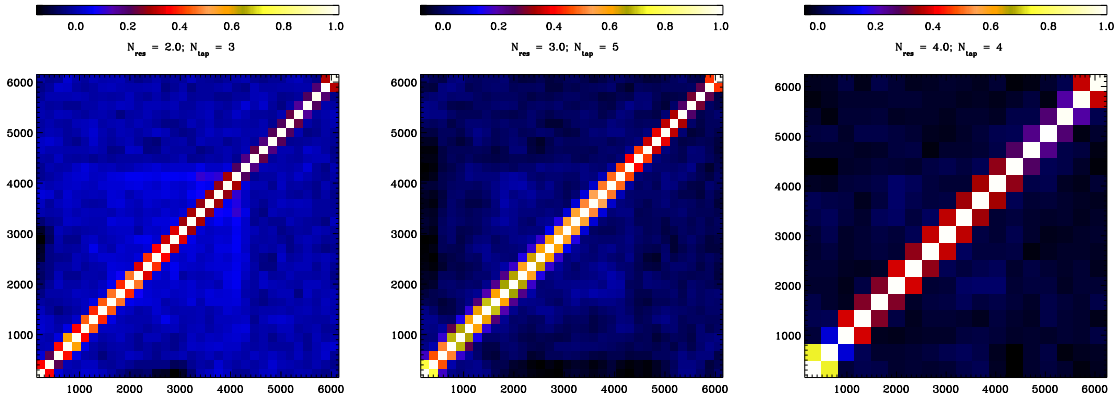

Figure 2.8: Covariance matrix of the bandpowers estimated via AMTM for three different parameter settings; from left to right these are: $N_{res} = 2.0$, $N_{tap} = 3$; $N_{res} = 3.0$, $N_{tap} = 5$ and $N_{res} = 4.0$, $N_{tap} = 4$. Each square in the image represents a bin in ℓ. For the $N_{res} = 2.0$ and $N_{res} = 3.0$ cases, we chose the bin-widths to be twice the fundamental resolution element, i.e. $\Delta\ell = 2\ell_{fund} = 180$, while for the $N_{res} = 4.0$ case it was taken to be $4\ell_{fund} = 360$. There is appreciable covariance only between bins inside the resolution $\Delta\ell_W = 2\ N_{res}\ \ell_{fund}$ set by the taper, and the covariance drops drastically beyond that frequency.

where,

$$C_{ab} = \left\langle (C_a - \langle C_a \rangle)^2 (C_b - \langle C_b \rangle)^2 \right\rangle . \tag{2.39}$$

We use our Monte Carlo simulations to estimate the quantity above. The results are displayed in Fig. 2.8. These figures illustrate an extremely desirable feature of the AMTM estimator i.e. the bandpowers are essentially uncorrelated beyond the spectral resolution $\Delta\ell_W = 2\ N_{res}\ \ell_{fund}$ set by the taper parameters. This implies that if we set the bin widths to be same as $\Delta\ell_W$ then adjacent bins will be uncorrelated. If our bins are smaller, they will be correlated through a mode coupling matrix which is fairly diagonal, and hence can be easily inverted to decouple them, an issue we will briefly touch upon in § 2.5.

In the following section, we turn to the more practical issue of dealing with CMB maps with noise and point source masks in them.

2.4 Prewhitening for CMB Maps with mask and noise

The maps of the cosmic microwave background produced by any experiment will invariably contain instrumental noise and regions, like bright point sources, that are usually masked out before estimating the power spectrum. The raw sky map also contains other astrophysical contaminants which we will neglect for the purpose of this discussion.

Application of point source mask to a map is essentially replacing the pixel values in an area containing each point source with zeros. Masking is therefore equivalent to multiplying the map with a function which is unity everywhere except inside discs of varying sizes, where it is zero. This can also be thought of as successively multiplying the map with a mask for each point source. Taking power spectrum of the final masked map is therefore equivalent to successively convolving the true power spectrum with power spectra of a series of such single-point-source masks. As the size of the discs will in general vary for each such function, the true power spectrum will be convolved with functions that have power over various ranges of multipoles. Although the multiplication with tapers will guard against aliasing of power due to sharp edge of the map, they will be ineffective against the mixing of power due to a point source mask. We propose here a method for dealing with such issues, which in essence is the following:

1. Perform local real space convolution of the map with designed kernels so as to make its power spectrum as flat (white) as possible, at least over the range of multipoles which is affected most by aliasing of power due to the point source mask. We refer to this procedure as "Prewhitening".

2. Perform an AMTM power spectrum estimation of this prewhitened map in order to minimize any additional aliasing of power due to sharp edges of the map.

3. As the prewhitening operation was a convolution whose Fourier space form is (preferably analytically) known, divide the power spectrum of the prewhitened map with the Fourier space form of the prewhitening function to recover the power spectrum.

Note that the design of the prewhitening function will be specific to the type of signal being considered. In the following, we will demonstrate the prewhitening of CMB maps, with forms of the prewhitening function specific to the features in the CMB power spectrum. We will first consider a noiseless map, in order to motivate the basic form of the prewhitening operation and then generalize to maps with white noise.

2.4.1 Prewhitening of noiseless CMB maps

Let us denote the pure CMB temperature map as $T(\boldsymbol{\theta})$. An important feature of the power spectrum of the CMB C_ℓ is that beyond a multipole of ~ 1000, it is approximately proportional to ℓ^{-4}. Such sharp fall in the power makes it extremely prone to aliasing of power across multipoles due to a point source mask. If we perform an operation akin to taking the Laplacian of this map, then we would effectively multiply the power spectrum by ℓ^4 on all scales, thereby making the processed power spectrum nearly white over the large ℓ tail. This would thereby minimize aliasing of power. In the following we propose a method of achieving this, by a combination of two operations which we call "disc-differencing" and "self-injection".

Disc-differencing

If we convolve the map with a circular disc of radius R, generating,

$$T_R(\boldsymbol{\theta}) = \int d^2\boldsymbol{\theta}' W_R(\boldsymbol{\theta}' - \boldsymbol{\theta}) T(\boldsymbol{\theta}') \tag{2.40}$$

where W_R is the top-hat filter,

$$W_R(\boldsymbol{\theta}) = \begin{cases} \frac{1}{\pi R^2} & \text{if } |\boldsymbol{\theta}| \leq R, \\ 0 & \text{otherwise,} \end{cases} \tag{2.41}$$

then in Fourier space, we will have

$$T_R(\boldsymbol{\ell}) = W_R(\boldsymbol{\ell}) T(\boldsymbol{\ell}) \tag{2.42}$$

where the Fourier space window, $W(\boldsymbol{\ell})$ is given by,

$$W_R(\boldsymbol{\ell}) = 2\frac{J_1(\ell R)}{\ell R}. \tag{2.43}$$

Now let us consider smoothing the map with another top-hat window of radius $3R$, giving,

$$T_{3R}(\boldsymbol{\theta}) = \int d^2\boldsymbol{\theta}' W_{3R}(\boldsymbol{\theta}' - \boldsymbol{\theta}) T(\boldsymbol{\theta}'). \tag{2.44}$$

We then take the difference map,

$$T_{R-3R} = T_R - T_{3R}, \tag{2.45}$$

which in Fourier space reads,

$$\begin{aligned} T_{R-3R}(\boldsymbol{\ell}) &= W_{R-3R}(\ell) T(\ell) & (2.46)\\ &\equiv 2\left(\frac{J_1(\ell R)}{\ell R} - \frac{J_1(3\ell R)}{3\ell R}\right) T(\ell). & (2.47) \end{aligned}$$

Remembering the asymptotic expansion of $J_1(x)$ for $x << \sqrt{2}$,

$$2\frac{J_1(x)}{x} \simeq 1 - \frac{x^2}{8}, \tag{2.48}$$

which shows that for values of ℓ such that $\ell R < \sqrt{2}$, we have,

$$T_{R-3R}(\boldsymbol{\ell}) \simeq (\ell R)^2 T(\ell), \tag{2.49}$$

which implies that the power spectrum is now,

$$(2\pi)^2 C_\ell^{R-3R} \simeq \langle T_{R-3R}(\boldsymbol{\ell})^* T_{R-3R}(\boldsymbol{\ell}) \rangle = (2\pi)^2 \ell^4 R^4 C_\ell, \tag{2.50}$$

which is the desired form. The disc-difference window, $W_{R-3R}(\ell R)$ is shown in Fig. 2.9. Beyond $\ell = \sqrt{2}/R$, the function starts falling again. Thus by choosing the radius R judiciously, one can prewhiten a desired range of the power spectrum.

An important aspect of this method is that it is an effective $\mathbb{C}^{-1/2}$ operation on the map ($\mathbb{C}$ is the covariance matrix), which is manifestly local, and therefore does not suffer from effects due to edges, which is a common problem in case of the full Fourier space operation. Maximum likelihood methods of estimation of power spectra naturally involve the $\mathbb{C}^{-1}$

operation (Tegmark, 1997; Oh et al., 1999). However, for high resolution experiments, the numerical costs for computing the $\mathbb{C}^{-1}$ matrix can be prohibitively large. Also, such an operation is non-local and mixes modes from masks with the map in a non-trivial way. The method proposed here is approximate but is simple to implement as it involves only convolutions in real space: as such, its effect can be quantified, propagated or undone very easily.

Figure 2.10 illustrates the effect of the disc-differencing operation on the CMB power spectrum, for a radius $R = 1'$. This means that the prewhitening window turns around at $\ell \simeq \sqrt{2}/R \simeq 5000$. The application of the disc-differencing produces the processed power spectrum shown by the dashed curve in the figure, which has much smaller dynamic range than the original one shown by the dotted curve.

Self-injection

One undesirable effect of the application of the disc-differencing function is that it makes the lower multipole part of the CMB power spectrum ($\ell \lesssim 1000$) a steeply rising function, which may aggravate aliasing of power. A simple way to deal with this problem, is to add a small fraction of the original map back into the disc-differences map, a process we call "self-injection". If a fraction $\alpha \ll 1$ of the map is self-injected after the disc-differencing, the processed power spectrum looks flat at all multipoles, and is conveniently given by a multiplication of the true power spectrum with an analytic function,

$$C_\ell^{PW} = (W_{R-3R}(\ell R) + \alpha)^2 C_\ell. \tag{2.51}$$

This is illustrated for $\alpha = 0.02$ in Fig. 2.10.

Having laid out the basic theory of prewhitening, we will now describe a concrete example of power spectrum estimation of a CMB map with a point source mask to judge the effectiveness of this method in recovering the true power spectrum. To this end we simulate a $8^\circ \times 8^\circ$ map as a Gaussian random realization from a theory power spectrum. The map has 768 pixels on a side, making the pixel scale $\Delta\theta = 0.625'$. We cut out a $4^\circ \times 4^\circ$ section from this map to impose non-periodic boundary conditions. We then simulate a

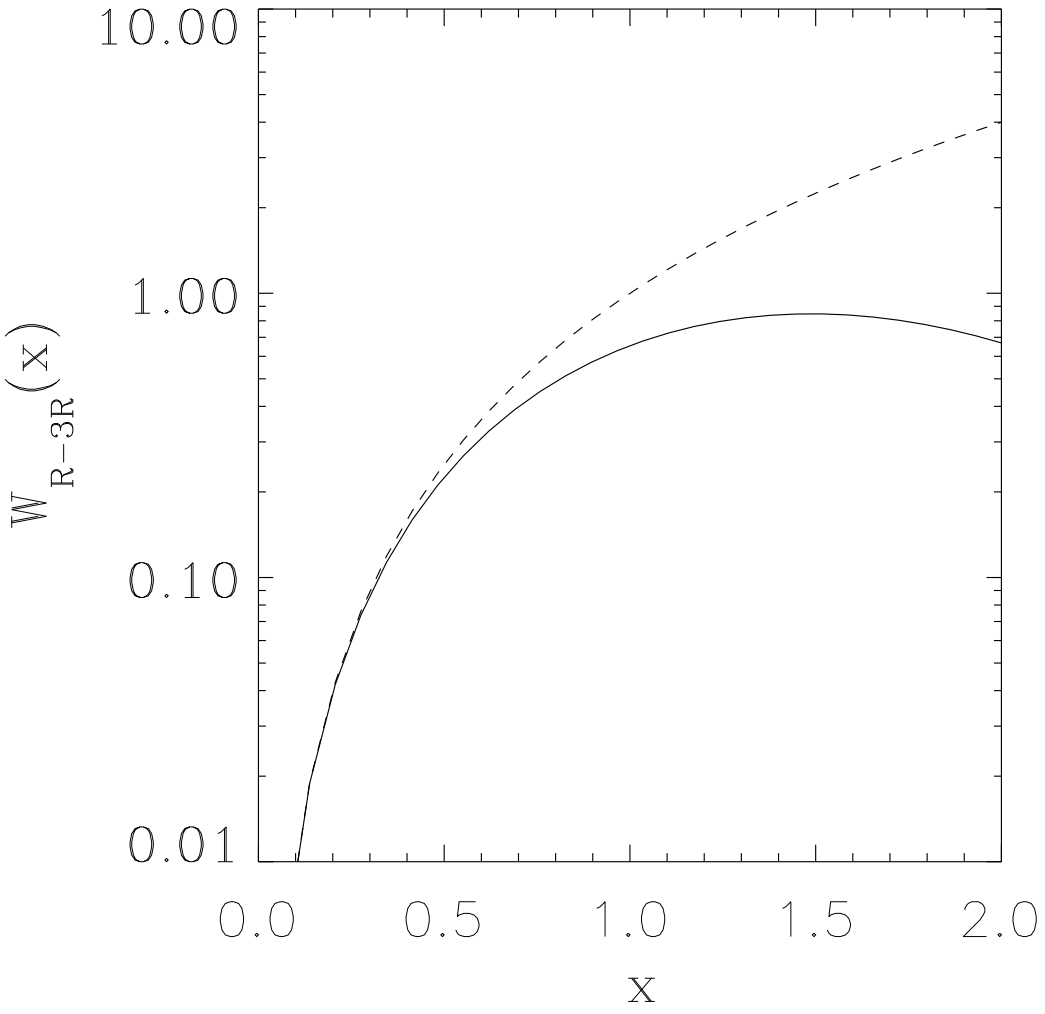

Figure 2.9: "Disc-difference" function W_{R-3R} discussed in the text (solid line). The dashed line represents the function x^4.

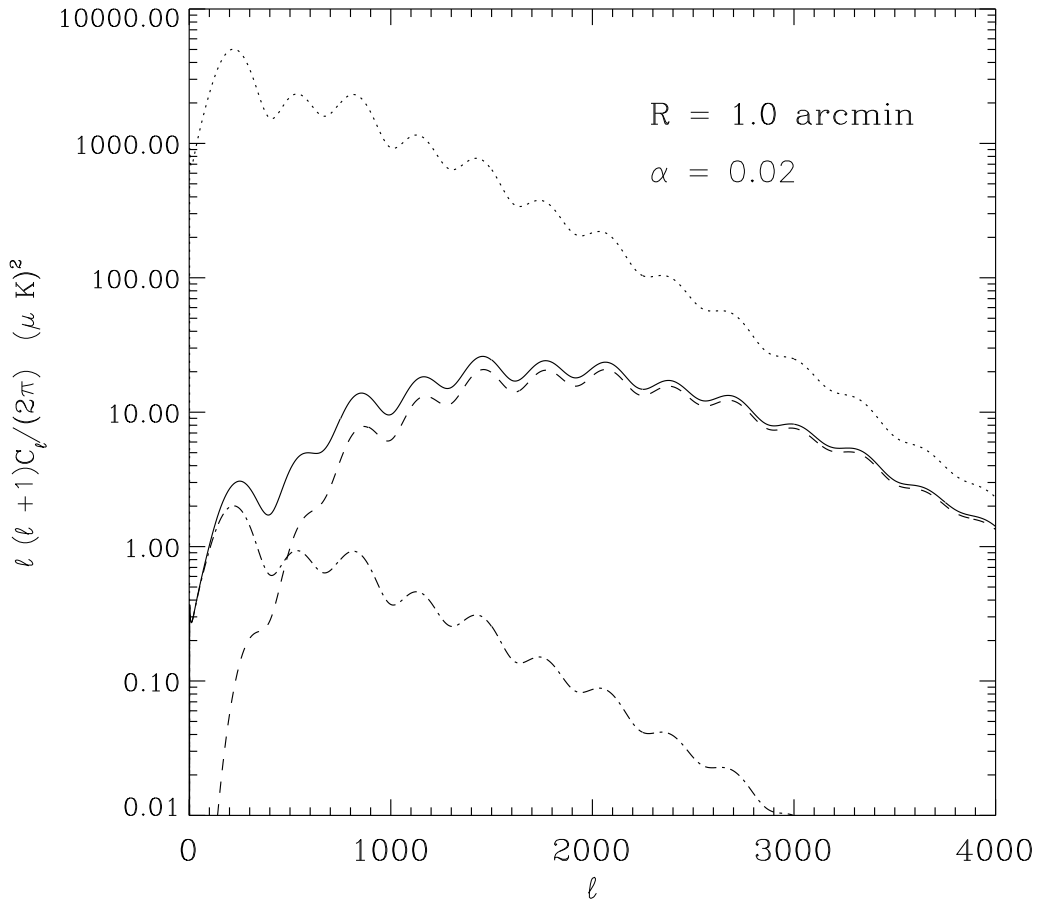

Figure 2.10: Effect of disc-differencing and self-injection on the power spectrum. The dotted line is the true power spectrum with a large dynamic range. The disc-differencing operation alone produces the dashed curve which has a much smaller dynamic range, but is steeply rising at low multipoles. The disc radius used is $R = 1'$. The dot-dashed curve shows the true power spectrum multiplied by a constant α^2 where $\alpha = 0.02$. If we disc-difference the map followed by self-injection of a fraction α of the map, then the power spectrum of the processed map is the solid curve (given by equation (2.51)) which is conveniently flat over the range of multipoles.

point source mask for this smaller map, which is unity everywhere except inside randomly positioned discs of various radii, where it is zero.

To motivate the necessity of prewhitening, we first apply the mask directly to the map and take its AMTM power spectrum with $N_{res} = 3.0$ and $N_{tap} = 3^2$. The result is shown in Fig 2.11. Note that we expressly use only the first few tapers with least leakage to ensure that mode coupling is minimized due to sharp edges of the map. However, this choice has no bearing against the aliasing of power due to holes in the map and as expected, we find a lot of power aliased from the low to the high multipoles. Next we perform a disc-difference operation on the original map with $R = 1'$, followed by a self-injection with $\alpha = 0.02$. Then, we apply the mask on this prewhitened map and perform AMTM power spectrum estimation on it. By comparing with the expected theoretical power spectrum, we find that aliasing is almost non-existent in the power spectrum of the prewhitened and masked map. Then we simply divide this power spectrum by the analytical transfer function for the prewhitening operation equation (2.51), to obtain a nearly unbiased estimate of the true power spectrum.

2.4.2 Prewhitening of Noisy Maps

In a real experiment, the map will be convolved with the instrument beam and will contain noise from the instrument as well as other astrophysical signals. To simulate the simplest of such situations, we convolve the map from the previous step with a Gaussian beam of full-width-at-half-maximum (FWHM) of $5'$. Next, we add Gaussian white noise at a level of 3 μK per sky pixel (defined as an area of FWHM^2 on the sky). The power spectrum of the map so generated has the usual initial sharp fall with multipole ℓ, but then flattens out beyond the multipole where white noise starts to dominate. One immediate consequence of this is that the disc differencing operation that multiplies the power spectrum by ℓ^4 will make the white noise part rise with ℓ instead of remaining flat. One can try to minimize this effect by judiciously choosing the disc radius R so that the disc-differencing window function turns over at the value of ℓ where white noise starts to dominate. However, there

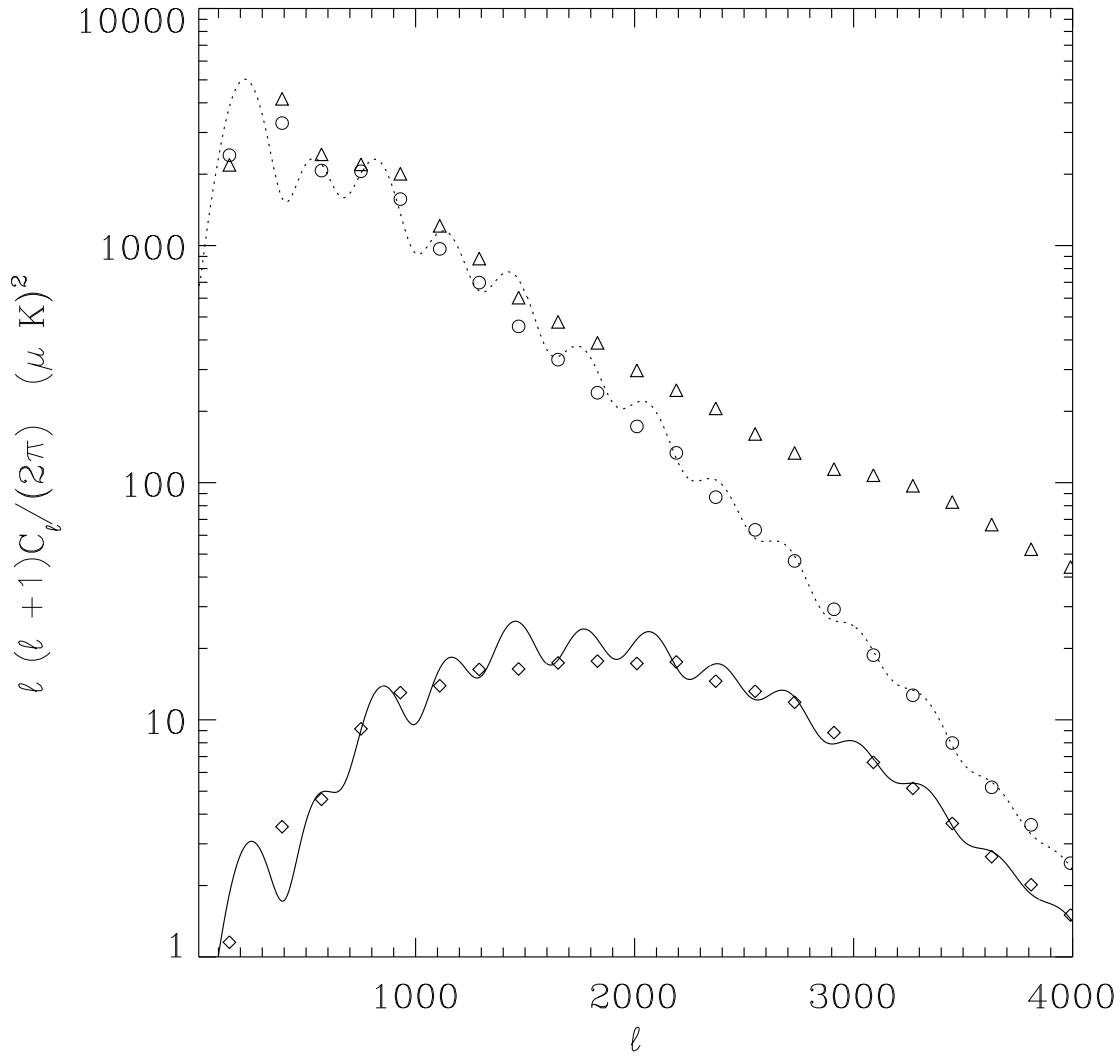

Figure 2.11: Prewhitening and AMTM as a remedy to aliasing of power due to point source mask. The dotted curve represents the input power spectrum from which the map is generated. The triangles represent the recovered AMTM power spectrum ($N_{res} = 3.0$, $N_{tap} = 3^2$) of the map after a point source mask is applied directly to it. If, on the other hand, the map is first prewhitened (see text) and the mask is subsequently applied, one obtains the diamonds as the AMTM power spectrum. The solid curve is the theoretical prediction for the prewhitened power spectrum. Thereafter, one divides the spectrum by the prewhitening transfer function (see equation (2.51), obtaining a nearly unbiased estimate, denoted by the open circles. Note that the AMTM power spectra appear smoother than the true spectra as the former is convolved with the window function of the taper.

may be components to the power spectrum other than white noise which may rise faster than the fall of the disc-differencing window. All these cases can be effectively dealt with by introducing another component to the prewhitening operation: namely a convolution with a Gaussian window after the disc-differencing and the self-injection steps. If we convolve the map with a Gaussian of FWHM θ_s then after evaluating the power spectrum we can remove its effect by dividing it by the multipole space form $\exp(\ell(\ell+1)\theta_s/(8\log 2))$. In Fig. 2.12 we illustrate the prewhitening in presence of white noise.

2.5 Mode-mode coupling and deconvolution

As discussed earlier, an undesirable feature of the Multitaper method is the loss of spectral resolution. For any $N_{res} > 1$, a Multitaper estimator smooths the power spectrum with a frequency-space window which is wider than the fundamental resolution set by the size of the map. For power spectra which are highly structured, this poses the problem of diluting interesting features which may render the power spectrum less useful as a direct probe of the underlying phenomenon. For example, in case of the CMB, (A)MTM leads to the smoothing of acoustic features.

In CMB analyses, the problem of recovering the true power spectrum from one that has been convolved with a window function is a well studied problem. It arises naturally in full-sky CMB experiments because of the application of point source and galactic masks. A detailed account of the procedure to deal with mode-mode coupling in the spherical harmonic space can be found in Hivon et al. (2002). In what follows, we will discuss the mode-mode coupling in flat space and develop the method of deconvolving the effective tapering window function from the power spectrum.

Consider a homogeneous, isotropic and zero-mean Gaussian random process realized on a map, $T(\mathbf{x})$, with a power spectrum $P(k)$,

$$\left\langle T(\mathbf{k})^* T(\mathbf{k}') \right\rangle = (2\pi)^2 \delta(\mathbf{k}-\mathbf{k}') P(k). \tag{2.52}$$

If the map is multiplied by a window $W(\mathbf{x})$, then the Fourier transform of the resulting

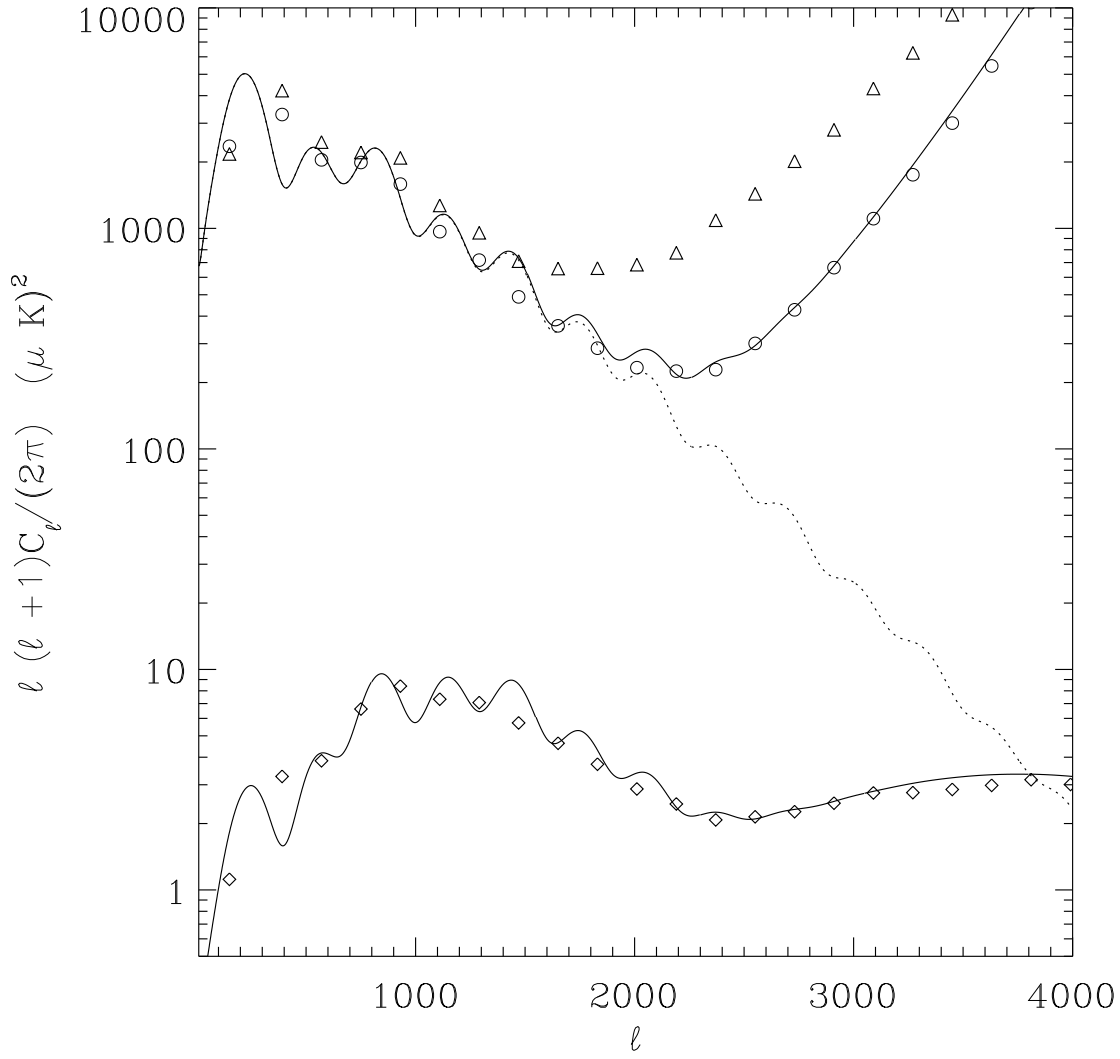

Figure 2.12: Same as in Fig. 2.11, but for a map with white noise. In addition to the standard prewhitening operation, a Gaussian smoothing has been applied to flatten the tail of the prewhitened map.

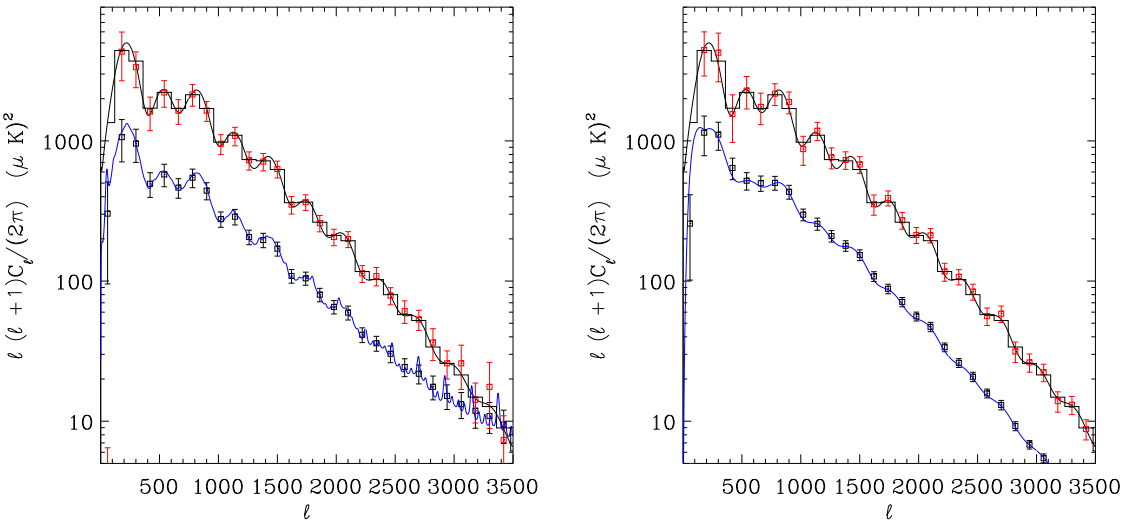

Figure 2.13: Deconvolution of the power spectrum. *Left panel*: Deconvolution of the periodogram with top-hat weighting. The black squares represent the binned power spectrum obtained directly from the map using the periodogram (straight FFT) method. As discussed in the text, this power spectrum is the true power spectrum convolved with the mode-mode coupling matrix due to the top-hat, the theoretical expectation for which is displayed as the blue line. The red points represent the binned power spectrum deconvolved via equation (2.60). The black line is the input power spectrum. The deconvolved binned power spectrum is to be compared with the binned input power spectrum which is displayed as the black histogram. All points displayed are the mean of 800 Monte Carlo simulations and the error bars correspond to the 2σ spread in their values. *Right Panel:* Same as above, but for the AMTM method. The mode-coupled power spectrum and the corresponding theoretical curve in this case have been artificially shifted below the deconvolved power spectra for easy viewing. As discussed in the text, the mode-coupled power spectrum produced by the AMTM method is a nearly unbiased estimate of the true power spectrum, while the mode-coupled periodogram (left panel) is highly biased at large multipoles. This bias causes the error bars in the deconvolved periodogram to be much larger than those in the deconvolved AMTM power spectrum at large ℓ, as shown in Fig. 2.14.

map is given by the convolution,

$$T^W(\mathbf{k}) = \int \frac{d^2\mathbf{k}'}{(2\pi)^2} T(\mathbf{k}')W(\mathbf{k}-\mathbf{k}'). \tag{2.53}$$

In the ensemble average sense, we therefore have,

$$\left\langle \hat{P}_W(\mathbf{k}) \right\rangle \equiv \frac{1}{(2\pi)^2} \left\langle T^{W*}(\mathbf{k}) T^W(\mathbf{k}) \right\rangle \tag{2.54}$$

$$= \int \frac{d^2\mathbf{k}'}{(2\pi)^2} \frac{|W(\mathbf{k}-\mathbf{k}')|^2}{(2\pi)^2} P(k'), \tag{2.55}$$

which is often referred to as the pseudo power spectrum in CMB literature. All the multitapered power spectra discussed so far are pseudo-power spectra in this sense, and comparing with equation (2.30), it is easily seen that for AMTM, the power spectrum of effective window that couples to the true power spectrum is given by,

$$W^{AMTM}(\mathbf{k}) = \frac{\sum_{\alpha_1,\alpha_2} b^2_{(\alpha_1\alpha_2)}(\mathbf{k}) \tilde{V}^{(\alpha_1\alpha_2;N_1N_2)}(\mathbf{k})}{\sum_{\alpha_1,\alpha_2} b^2_{(\alpha_1\alpha_2)}(\mathbf{k})}. \tag{2.56}$$

One is obviously interested in the angle averaged pseudo power spectrum,

$$\hat{P}^W(k) = \int \frac{d\theta}{(2\pi)} P^W(\mathbf{k}) \tag{2.57}$$

and as demonstrated in appendix 2.B, this can be expressed in terms of the true power spectrum as,

$$\left\langle \hat{P}^W(k) \right\rangle = \int dk' M(k,k') P(k') \tag{2.58}$$

where M is the mode-mode coupling kernel and depends on the power spectrum of the window W. After the power spectrum is binned, the above relation can be conveniently expressed as a matrix multiplication (see appendix 2.B,),

$$\left\langle \hat{P}^W_b \right\rangle = \sum_{b'} \tilde{M}_{bb'} P_{b'} \tag{2.59}$$

where b are the indices for the bins and $\tilde{\mathbb{M}}$ is the binned mode -mode coupling matrix. The binned mode-mode coupling matrix is more stable to inversion than the un-binned one which tends to be nearly singular, and therefore an estimate of the true power spectrum can be obtained by inverting the above relation,

$$\hat{P}_b = (\tilde{\mathbb{M}}^{-1})_{bb'} \hat{P}^W_{b'}. \tag{2.60}$$

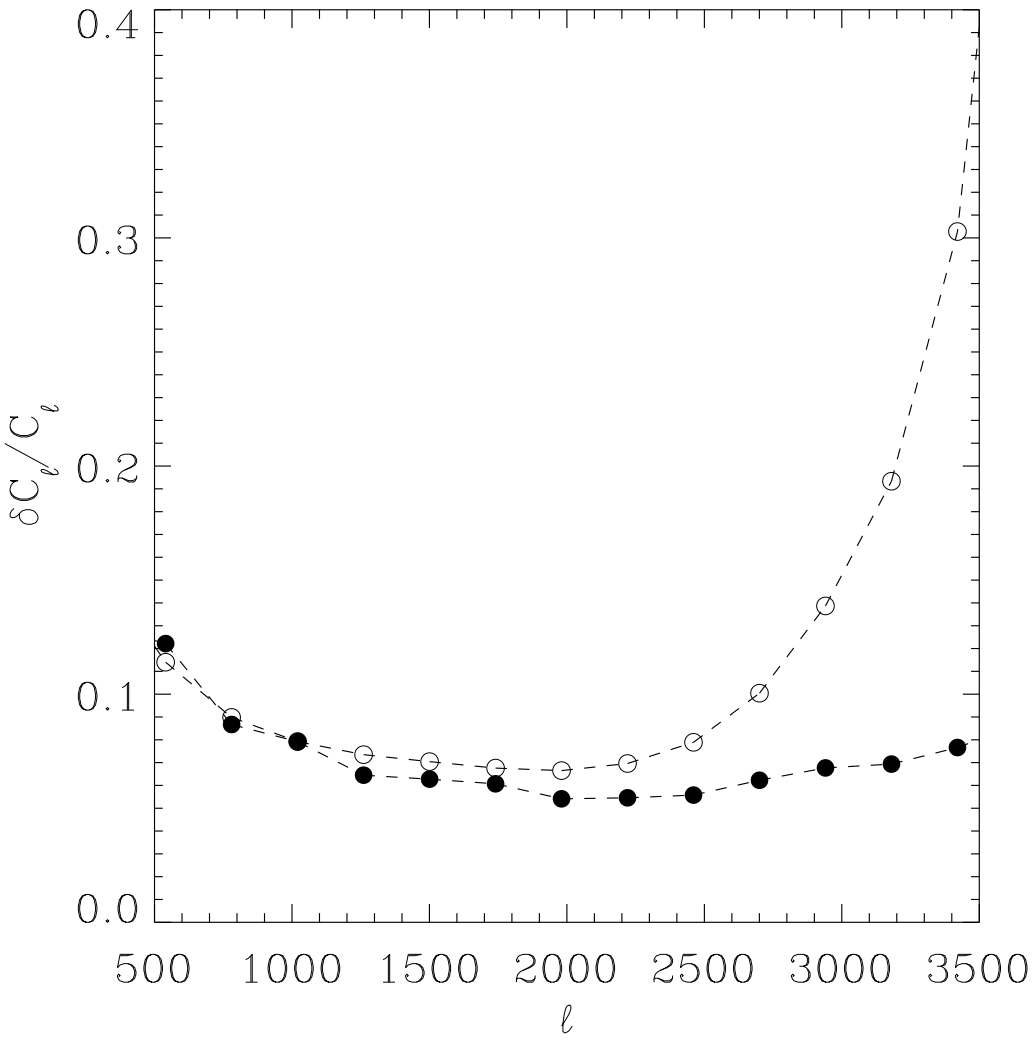

Figure 2.14: Fractional errors in the deconvolved binned power spectrum. The open circles represent the fractional errors for the periodogram method (left panel of Fig. 2.13). The filled circles represent the same for the AMTM method (right panel of Fig. 2.13). Although the deconvolved power spectrum obtained from either method is an unbiased estimate of the true power spectrum, the errors from the periodogram method are much larger at high ℓ because of the highly biased nature of the mode-coupled periodogram at those multipoles.

We first illustrate the deconvolution of the power spectrum without a point source mask. For this purpose, we simulate a large 16 degree square map, with 768 pixels on a side, using a theoretical power spectrum. We then perform power spectrum analysis of the central 8 degree square portion of it. For the periodogram, we simply zero out the portion of the larger map outside the central 8 degree square, so that the mask becomes a zero-padded top-hat. For the AMTM, we discard the outer regions and perform the adaptive multitaper analysis with $N_{res} = 3$, $N_{tap} = 5^2$ on the central 8 degree square. We generate the mode coupled power spectrum with each method and then deconvolve it using equation (2.60). The results from 800 Monte Carlo experiments are shown in Fig. 2.13.

Firstly, we note that the construction of the mode-mode coupling matrix, as delineated in appendix 2.B, enables us to accurately predict the mode-mode coupled theoretical power spectrum. As such, likelihood analyses for cosmological parameters can potentially be performed with the mode-coupled AMTM power spectrum, and this is specially appealing because the statistical properties of the mode-coupled binned power spectra can be precisely predicted (see § 2.2.5).

Secondly, we find that the deconvolution of the periodogram as well as the AMTM power spectrum produces an unbiased estimate of the input power spectrum, but with a very important difference: the uncertainty in the deconvolved periodogram at $\ell \gtrsim 1500$ is larger than that in the deconvolved AMTM spectrum, and the difference continues to grow to factors of several for higher multipoles. This is seen clearly in Fig. 2.14, where we have plotted the fractional errors in the deconvolved binned power spectrum against the bin centers. For instance, at $\ell \sim 3000$ the periodogram method produces ~ 3 times larger error bars. This owes to the fact that due to spectral leakage, the periodogram produces a pseudo power spectrum that is highly biased relative to the input theory over these higher order multipoles. This bias adds to the uncertainty in the deconvolved power spectrum. On the other hand, AMTM produces a nearly unbiased, albeit smoothed, pseudo power spectrum which, when deconvolved, does not incur any excess uncertainties. Ignoring point source masks for the moment, which are very specific to the CMB, this result alone immediately

elevates the multitaper method to a far superior status than the periodogram, as a power spectrum estimation method for highly colored spectrum measured from finite maps.

One must bear in mind, that over the range of multipoles where leakage is not a serious problem, and the periodogram is essentially unbiased, the errors bars obtained from the periodogram are the smallest. This is because the periodogram makes use of all the modes that are available from the entire map, while each taper in a MTM process makes use of a certain fraction of the map. By using several tapers, one can compete with the periodogram error bars over the nearly white part of the spectrum. This is essentially seen in the convergence of the fractional error bars from the two methods in the low ℓ portion of Fig. 2.14. This, however, is not in contradiction to the fact, as shown in § 2.2.5 that it is possible to have lower uncertainties in any bin for the pseudo power spectrum with AMTM than with the periodogram, by choosing a high enough N_{res} (and consequently high N_{tap}). Unfortunately, this advantage goes away when the power spectrum is deconvolved.

Next we turn to the practical issue of dealing with a point source mask for a CMB map. As already discussed in § 2.4, the holes in the mask couple power over various scales, and neither the periodogram nor the AMTM remain an unbiased method at large multipoles, necessitating the prewhitening of the map. To study the effect of the mask and prewhitening on the deconvolved power spectrum, we multiply our map with a point source mask and repeat the Monte Carlo exercise with and without prewhitening. The mask has a covering fraction of 98% and the holes are of random sizes. For the prewhitening operation we use the parameters $R = 1'$ and $\alpha = 0.02$. The results on the fractional errors for this case are displayed in Fig. 2.15. This figure shows the power of prewhitening approach. Prewhitening significantly reduces the errors. It is obvious that like the periodogram, AMTM is defenseless against the point source holes in the mask. This is expected because a taper with holes no longer retains the nice property of being a band-limited function. For both the top-hat and the effective tapered window, the sidelobes become dominated by the power produced by the holes. In such a situation, prewhitening the map becomes a necessity to reduce the uncertainties in the deconvolved power spectrum. With proper prewhitening both the

periodogram and the AMTM method can produce nearly unbiased pseudo power spectra and consequently small error bars at the high multipoles, as evident from Fig. 2.15. It is important to note here that the power spectrum of a top-hat has greater sidelobe power than the effective taper in the intermediate range of multipoles between the regions where the central lobe is falling and where the point source power starts to dominate. Therefore, depending on the quality of prewhitening that can be performed on a map, AMTM may be a more reliable method to apply on the prewhitened and masked map, rather than the periodogram.

2.6 Conclusion

Power spectrum estimation on small sections of the CMB sky is a non-trivial problem due to spectral leakage from the finite nature of the patch, which is further compounded by the application of point source masks. The direct application of standard decorrelation techniques, like the MASTER algorithm (Hivon et al., 2002), to obtain an unbiased estimate of the power spectrum leads to unnecessarily large uncertainties at high multipoles due to the highly biased nature of the pseudo power spectrum at those multipoles. We have put forward two techniques to reduce the uncertainties in the deconvolved power spectrum. First, we have formulated a two-dimensional adaptive multitaper method (AMTM) which produces nearly unbiased pseudo power spectra for maps without point source masks, by minimizing the leakage of power due to the finite size of the patch. This is achieved at the cost of lowered spectral resolution. The deconvolution of the pseudo power spectrum so produced, leads to an unbiased estimate of the true power spectrum that has several times smaller error bars at high multipoles than the deconvolved periodogram. In presence of point source masks, however, this method becomes non-optimal because the pseudo power spectrum estimated even by AMTM is no longer unbiased. To deal with the point source mask, we have put forward a novel way of prewhitening a CMB map, with manifestly local operations which has simple representations in the Fourier space. This operation produces a map, the power spectrum of which has several orders of magnitude lower dynamic range

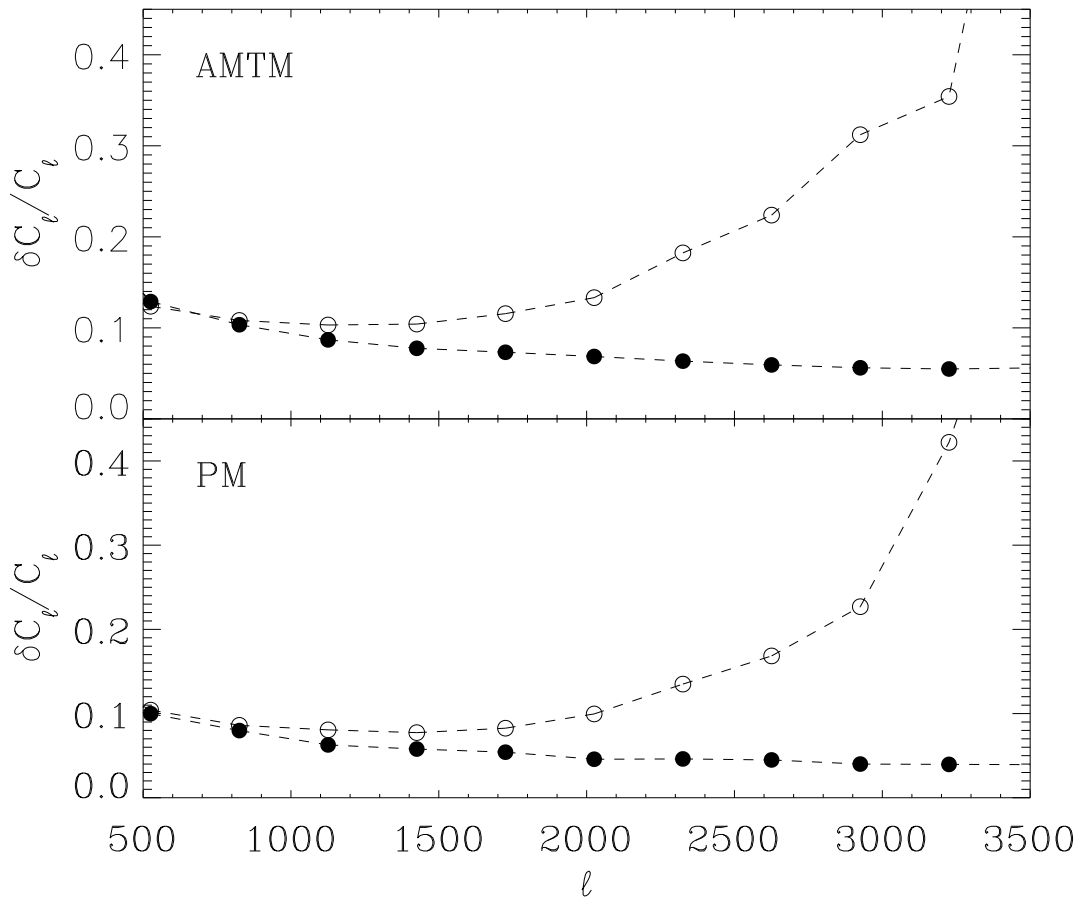

Figure 2.15: Effect of prewhitening on the errors in the deconvolved power spectrum in presence of a point source mask. *Top Panel:* For the AMTM method: The open circles represent the fractional 1σ error bars on the deconvolved power spectrum when prewhitening is not performed, showing that holes in the point source mask render the AMTM method biased at high multipoles and lead to large error bars. The filled circles represent the same after prewhitening has been performed, showing that prewhitening remedies the leakage of power and makes the power spectrum estimator nearly unbiased. *Bottom Panel:* The same as above, but for the periodogram or straight FFT. Note that prewhitening, if performed properly, makes the periodogram as good a power spectrum tool as the AMTM.

than the original map. This renders the leakage of power due to holes and edges a relatively benign issue for the prewhitened map. If the prewhitening operation can be tuned to make the power spectrum of the map nearly white, a pseudo power spectrum obtained via a simple periodogram may be nearly unbiased and therefore, can be deconvolved to give a precisely unbiased estimate of the power spectrum, thereby avoiding unnecessarily large error bars at large multipoles. If the map cannot be made sufficiently white for a periodogram, an AMTM method can be applied to the prewhitened map to guard against leakage and achieve the same result. We have shown that by applying these methods, one can reduce the error bar in the small scale power spectrum by a factor of ~ 4 at $\ell \sim 3500$. This can be translated into a many-fold reduction in the required integration time of a CMB experiment to achieve some target uncertainty on the small scale power spectrum than that dictated by standard techniques.

2.A Appendix: Statistical properties of multitaper estimators

The statistical properties of the multitaper spectral estimators follow from the basic result equation (2.32) for the distribution of the periodogram. In the following, we will use the equivalent degrees of freedom argument to derive the distribution functions for the MTM estimators. The first result we will use is that the probability distribution of an eigenspectrum $\hat{P}^{(\alpha_1\alpha_2)}(\mathbf{k})$ at each frequency-space point $\mathbf{k}$ (i.e. at each pixel) will have the same form as equation (2.32) for asymptotically large N. Since the final spectral estimate is a weighted sum of these eigenspectra, it is reasonable to assume that the former is distributed also as a scaled χ^2 variable. Let us hypothesize,

$$P^{\mathrm{AMTM}}(\mathbf{k}) \stackrel{\mathbf{d}}{=} a\chi^2_\nu \tag{2.A.1}$$

where both ν and a are unknown. Now, we will make use of the facts that $\left\langle P^{\mathrm{AMTM}} \right\rangle = \left\langle a\chi^2_\nu \right\rangle = a\nu$ and $\mathrm{var}(P^{\mathrm{AMTM}}) = \mathrm{var}(a\chi^2_\nu) = 2a^2\nu$. Therefore,

$$\nu = \frac{2\left\langle P^{\mathrm{AMTM}} \right\rangle^2}{\mathrm{var}(P^{\mathrm{AMTM}})}\,;\;\; a = \frac{\left\langle P^{\mathrm{AMTM}} \right\rangle}{\nu}. \tag{2.A.2}$$

Since the eigenspectra $\hat{P}^{\alpha_1\alpha_2}$ are asymptotically uncorrelated and are also unbiased estimators of $P(\mathbf{k})$, we obtain, using the definition of the AMTM estimator equation (2.30),

$$\left\langle P^{\mathrm{AMTM}} \right\rangle = P(\mathbf{k}), \tag{2.A.3}$$

$$\mathrm{var}(P^{\mathrm{AMTM}}) = P^2(\mathbf{k}) \frac{\sum_{\alpha_1,\alpha_2} b^4_{(\alpha_1\alpha_2)}(\mathbf{k})}{\left(\sum_{\alpha_1,\alpha_2} b^2_{(\alpha_1\alpha_2)}(\mathbf{k})\right)^2} \tag{2.A.4}$$

for $N \to \infty$, which immediately gives us

$$\nu(\mathbf{k}) = \frac{2\left(\sum_{\alpha_1,\alpha_2} b^2_{(\alpha_1\alpha_2)}(\mathbf{k})\right)^2}{\sum_{\alpha_1,\alpha_2} b^4_{(\alpha_1\alpha_2)}(\mathbf{k})}. \tag{2.A.5}$$

which is equation equation (2.34).

Now we turn to the approximate form of the distribution for the binned power spectrum, P^B equation (2.35). We again postulate that P^B is distributed as $c\chi^2_{\nu_b}$, so that,

$$\nu_b = \frac{2\left\langle P^B \right\rangle^2}{\mathrm{var}(P^B)}\,;\;\; c = \frac{\left\langle P^{\mathrm{B}} \right\rangle}{\nu_b}. \tag{2.A.6}$$

Now note that because the images or maps we will be concerned with are real, only the half-plane in the $\mathbf{k}$ space are independent because of reflection symmetry i.e $P(\mathbf{k}) = P(-\mathbf{k})$. For the time being, let us assume that all $\mathbf{k}$ space pixels are uncorrelated, so that all pixels in one half of the $\mathbf{k}$ plane are independent of each other. Later, we will correct this for the fact the tapers highly correlate adjacent pixels in each resolution element. With these assumptions, equation (2.35) can be re-written as,

$$P^B(k_b) = \frac{2}{N_b} \sum_{i,j \in b; k_j > 0} P^{\rm AMTM}(k_i, k_j). \tag{2.A.7}$$

Therefore, the variance is given by,

$$\begin{aligned} {\rm var}(P^B(k_b)) &= \frac{4}{N_b^2} \sum_{i,j \in b; k_j > 0} \frac{2}{\nu(k_i, k_j)} \left\langle P^{\rm AMTM}(k_i, k_j) \right\rangle^2 \\ &= \frac{4}{N_b^2} \left\langle P^{\rm AMTM}(|\mathbf{k}| = k_b) \right\rangle^2 \\ &\quad \times \sum_{i,j \in b} \frac{1}{\nu(k_i, k_j)} \end{aligned} \tag{2.A.8}$$

where in the last step we have assumed that the power spectrum is slowly varying inside a bin. The factor of 2 inside the summation goes away because we have extended the summation to include the lower half plane. Using equation (2.A.6), we therefore get

$$\frac{1}{\nu_b} = \frac{2}{N_b^2} \sum_{i,j \in b} \frac{1}{\nu(k_i, k_j)}. \tag{2.A.9}$$

Now, we will correct for the fact that all pixels in the upper half plane are not independent. In fact for a taper with a given N_{res}, approximately N_{res}^2 pixels get highly correlated. Therefore we can think of "super-pixels" of dimension $N_{res} \times N_{res}$, which are independent of each other. If we repeat the calculation above with this assumption, then we obtain the result,

$$\frac{1}{\nu_b} \simeq \frac{2N_{res}^2}{N_b^2} \sum_{i,j \in b} \frac{1}{\nu(k_i, k_j)}, \tag{2.A.10}$$

which essentially reduces the degrees-of-freedom by the number of pixels that fall in each super-pixel. This is equation equation (2.37).

2.B Appendix: Mode-mode coupling matrix

In the following, we derive the form of the mode-mode coupling kernel. For the sake of completeness, we repeat and expand upon some of the calculations from appendix A.1 of Hivon et al. (2002). Note that the symbol k (frequency) in the said appendix of that paper is smaller by a factor of 2π than the k (angular frequency) used in the present section. In other words, the k used here is readily identified with the multipole ℓ in the flat-sky approximation, while it would stand for $\ell/(2\pi)$ in the aforementioned appendix.

We start with the definition equation (2.57) of the angle averaged pseudo power spectrum and with the aid of equation (2.54) express it as,

$$\left\langle \hat{P}^W(k_1) \right\rangle = \int \frac{d\theta_1}{(2\pi)} \int \frac{d^2\mathbf{k}_2}{(2\pi)^2} \frac{\left|W(\mathbf{k}_1 - \mathbf{k}_2)\right|^2}{(2\pi)^2} P(k_2). \tag{2.B.1}$$

We can express the Fourier mode of the window appearing above as

$$W(\mathbf{k}_1 - \mathbf{k}_2) = \int d^2\mathbf{k}_3 W(\mathbf{k}_3) \delta^2(\mathbf{k}_3 - \mathbf{k}_1 + \mathbf{k}_2) \tag{2.B.2}$$

which immediately gives,

$$\frac{\left|W(\mathbf{k}_1 - \mathbf{k}_2)\right|^2}{(2\pi)^2} = 2\pi \int dk_3 \; k_3 \mathcal{W}(k_3) \delta^2(\mathbf{k}_3 - \mathbf{k}_1 + \mathbf{k}_2) \tag{2.B.3}$$

where we have introduced the power spectrum of the window,

$$(2\pi)^2 \mathcal{W}(k) = \int \frac{d\theta}{(2\pi)} W^*(\mathbf{k}) W(\mathbf{k}). \tag{2.B.4}$$

Substituting in equation (2.B.1), we get,

$$\left\langle \hat{P}^W(k_1) \right\rangle = \int \frac{d\theta_1}{(2\pi)} \int \frac{dk_2 \; k_2}{(2\pi)} \int d\theta_2 P(k_2) \int dk_3 \; k_3 \mathcal{W}(k_3) \delta^2(\mathbf{k}_3 - \mathbf{k}_1 + \mathbf{k}_2) \tag{2.B.5}$$

$$= \int dk_2 M_{k_1 k_2} P(k_2), \tag{2.B.6}$$

where we have introduced the mode-mode coupling matrix,

$$M_{k_1 k_2} = \frac{k_2}{(2\pi)} \int dk_3 \; k_3 \mathcal{W}(k_3) J(k_1, k_2, k_3) \tag{2.B.7}$$

with,

$$J(k_1, k_2, k_3) = \int \frac{d\theta_1}{(2\pi)} \int d\theta_2 \delta^2(\mathbf{k}_3 - \mathbf{k}_1 + \mathbf{k}_2) \tag{2.B.8}$$

It is instructive to compare equation (2.B.7) with the full-sky result from appendix A.2 of Hivon et al. (2002),

$$M_{\ell_1\ell_2} = \frac{2\ell_2+1}{4\pi}\sum_{\ell_3}(2\ell_3+1)\mathcal{W}_{\ell_3}\begin{pmatrix}\ell_1 & \ell_2 & \ell_3\\ 0 & 0 & 0\end{pmatrix}^2. \tag{2.B.9}$$

It can be shown that for large ℓ,

$$\begin{pmatrix}\ell_1 & \ell_2 & \ell_3\\ 0 & 0 & 0\end{pmatrix}^2 \to J(\ell_1,\ell_2,\ell_3) \tag{2.B.10}$$

so that if we identify k_i with ℓ_i, the large ℓ limit of the spherical mode-mode coupling matrix goes correctly to the flat-sky expression equation (2.B.7). Note that the appearance of an extra factor of 2 in the large ℓ limit of the summand in equation (2.B.9) over the integrand in equation (2.B.7) is fine because the sum is restricted to values ℓ_3 which make $(\ell_1+\ell_2+\ell_3)$ even, while the integral over k spans the entire allowed range for each (k_1,k_2) pair.

We now turn to the evaluation of the J function. Using the factorized form of the delta function in plane polar coordinates, $\delta(\mathbf{r}-\mathbf{r}') = \delta(r-r')\delta(\theta-\theta')/r$, we can write,

$$J(k_1,k_2,k_3) = \frac{1}{(2\pi)}\int d\theta_2\delta^2(k_1-|\mathbf{k}_3+\mathbf{k}_2|)/k_1. \tag{2.B.11}$$

The integral over θ_2 can be performed by using the following property of the delta function,

$$\delta(g(x)) = \sum_i \frac{\delta(x-x_i)}{|g'(x_i)|} \tag{2.B.12}$$

where x_i are the roots of $g(x)=0$. In our case there are two roots and the integral finally yields

$$J(k_1,k_2,k_3) = \frac{2}{\pi}\frac{1}{\sqrt{-K(K-2k_1)(K-2k_2)(K-2k_3)}} \tag{2.B.13}$$

for $|k_2-k_3| < k_1 < k_1+k_2$, and zero outside the interval, where $K = k_1+k_2+k_3$. As a word of caution against using this form directly into the integral equation (2.B.7), we would like to point out that due to the diverging nature of the integrand near the edges of the allowed interval, numerical integration schemes that span the entire range will be unreliable. Instead we find, drawing parallels with the spherical harmonic case, that approximating the

integration in equation (2.B.7) by a sum over integral values of k, by interpolating $\mathcal{W}(k)$ onto integers, provides a very stable and reliable way of computing the mode coupling matrix. In fact, the boundaries of interval can be included in the sum by using the large ℓ limit of the $3-j$ functions at those points,

$$\begin{pmatrix} \ell_1 & \ell_2 & \ell_3 \\ 0 & 0 & 0 \end{pmatrix}^2 \rightarrow \begin{cases} \frac{1}{2\sqrt{\pi \ell_1 \ell_2 \ell_3}} & \text{for } \ell_3 \rightarrow \ell_1 + \ell_2 \text{ or } \ell_3 \rightarrow |\ell_1 - \ell_2| \\ \frac{\delta_{\ell_1 \ell_2}}{2\ell_1} & \text{for } \ell_3 = 0 \end{cases} . \tag{2.B.14}$$

At the end of the exercise, we therefore generate the mode-coupling matrix at integer subscripts, which by abusing notation a bit, we will denote by $M_{\ell\ell'}$.

Next, we consider the binning of the pseudo power spectrum. In order to construct the mode-mode coupling kernel relevant to a binned power spectrum, we first define the binning operator B, which performs the binning of the integral indexed quantities to binned values and its reciprocal operation U. Given the lower and upper boundaries,$\ell^b_{\rm low}$ and $\ell^b_{\rm high}$ of a bin b, a simple form of these operators can be written as,

$$B_{b\ell} = \begin{cases} \frac{\ell^\alpha}{(\ell^b_{\rm high} - \ell^b_{\rm low})}, & \text{if } 2 \leq \ell^b_{\rm low} \leq \ell < \ell^b_{\rm high} \\ 0, & \text{otherwise,} \end{cases} \tag{2.B.15}$$

and

$$U_{\ell b} = \begin{cases} \frac{1}{\ell^\alpha}, & \text{if } 2 \leq \ell^b_{\rm low} \leq \ell < \ell^b_{\rm high} \\ 0, & \text{otherwise.} \end{cases} \tag{2.B.16}$$

Here, α is chosen to make the power spectrum "flatter" and for the damping tail of the CMB, a suitable value is $\alpha = 4$.

Note that the pseudo power spectrum realized on the two-dimensional **k**-space may be directly binned into the bins b, by averaging the value in the pixels that fall inside the annuli demarcated by the bin boundaries, without having to go through an intermediate step of interpolating the power spectrum onto integers. The binned pseudo power spectrum

is, therefore related to the binned true power spectrum as

$$\begin{aligned} \left\langle P_b^W \right\rangle &= B_{b\ell} M_{\ell\ell'} P_{\ell'} \\ &= B_{b\ell} M_{\ell\ell'} U_{\ell' b'} B_{b'\ell'} P_{\ell'} \\ &= \tilde{M}_{bb'} P_{b'}, \end{aligned} \tag{2.B.17}$$

where we have defined the binned mode-mode coupling matrix as $\tilde{\mathbb{M}} = \mathbb{B}^T \mathbb{M} \mathbb{U}$.

Acknowledgements

We dedicate this paper to the memory of eminent geophysicist F. Anthony Dahlen (1942-2007), who had suggested to us the idea of multitapering for the CMB. We would like to thank Frederick J. Simons, Mark A. Wieczorek, Neelima Sehgal and Tobias A. Marriage for enlightening discussions and Viviana Acquaviva for useful comments on the manuscript. SD would like to acknowledge the warm hospitality extended by the mentors and colleagues at Jadwin hall, specially Lyman Page and Jo Dunkley, while the Department of Astrophysics was under renovation. AH would like to thank Eric Hivon for useful discussions. AH is supported by the LTSA program. SD is supported by the Charlotte Elizabeth Procter Honorific Fellowship from Princeton University and NSF grant 0707731. DNS acknowledges support from NASA ATP grant NNX 08AH30G.

References

Barr, D. L., Brown, W. L., & Thompson, D. J. 1988, Le Journal de Physique Colloques, 49, C6

Bell, B., Percival, D. B., & Walden, A. T. 1993, Journal of Computational and Graphical Statistics, 2, 119

Bronez, T. 1988, Acoustics, Speech and Signal Processing, IEEE Transactions on, 36, 1862

Cramer, H. 1940, The Annals of Mathematics, 41, 215

Dahlen, F. A. & Simons, F. J. 2007, ArXiv e-prints, 705

Doob, J. L. 1963, SIAM Review, 5, 172

Doré, O., Teyssier, R., Bouchet, F. R., Vibert, D., & Prunet, S. 2001, A&A, 374, 358

Gorski, K. M., Banday, A. J., Bennett, C. L., Hinshaw, G., Kogut, A., Smoot, G. F., & Wright, E. L. 1996, ApJ, 464, L11+

Hajian, A. & Souradeep, T. 2006, Phys. Rev. D, 74, 123521

Hanssen, A. 1997, Signal Process., 58, 327

Hinshaw, G., Weiland, J. L., Hill, R. S., Odegard, N., Larson, D., Bennett, C. L., Dunkley, J., Gold, B., Greason, M. R., Jarosik, N., Komatsu, E., Nolta, M. R., Page, L., Spergel, D. N., Wollack, E., Halpern, M., Kogut, A., Limon, M., Meyer, S. S., Tucker, G. S., & Wright, E. L. 2008, ArXiv e-prints, 803

Hivon, E., Górski, K. M., Netterfield, C. B., Crill, B. P., Prunet, S., & Hansen, F. 2002, ApJ, 567, 2

Komatsu, E., Kogut, A., Nolta, M. R., Bennett, C. L., Halpern, M., Hinshaw, G., Jarosik, N., Limon, M., Meyer, S. S., Page, L., Spergel, D. N., Tucker, G. S., Verde, L., Wollack, E., & Wright, E. L. 2003, Apjs, 148, 119

Liu, T.-C. & van Veen, B. 1992, Signal Processing, IEEE Transactions on, 40, 578

Nolta, M. R., Dunkley, J., Hill, R. S., Hinshaw, G., Komatsu, E., Larson, D., Page, L., Spergel, D. N., Bennett, C. L., Gold, B., Jarosik, N., Odegard, N., Weiland, J. L., Wollack, E., Halpern, M., Kogut, A., Limon, M., Meyer, S. S., Tucker, G. S., & Wright, E. L. 2008, ArXiv e-prints, 803

Oh, S. P., Spergel, D. N., & Hinshaw, G. 1999, ApJ, 510, 551

Percival, D. B. & Walden, A. T. 1993, Spectral Analysis for Physical Applications, Multitaper and Conventional Univariate Techniques (New York: Cambridge Univ. Press)

Priestly, M. B. 1988, Journal of the Royal Statistical Society. Series A (Statistics in Society), 151, 573

QUaD collaboration: C. Pryke, Ade, P., Bock, J., Bowden, M., Brown, M. L., Cahill, G., Castro, P. G., Church, S., Culverhouse, T., Friedman, R., Ganga, K., Gear, W. K., Gupta, S., Hinderks, J., Kovac, J., Lange, A. E., Leitch, E., Melhuish, S. J., Memari, Y., Murphy, J. A., Orlando, A., Schwarz, R., O'Sullivan, C., Piccirillo, L., Rajguru, N., Rusholme, B., Taylor, A. N., Thompson, K. L., Turner, A. H., Wu, E. Y. S., & Zemcov, M. 2008, ArXiv e-prints, 805

Reichardt, C. L. et al. 2008

Simons, F. J., Dahlen, F. A., & Wieczorek, M. A. 2004, ArXiv Mathematics e-prints

Slepian, D. 1978, AT T Technical Journal, 57, 1371

Smith, K. M., Zahn, O., & Doré, O. 2007, Phys. Rev. D, 76, 043510

Tegmark, M. 1997, Phys. Rev. D, 56, 4514

Tegmark, M. 1997, Phys. Rev. D, 55, 5895

Thomson, D. 1982, Proceedings of the IEEE, 70, 1055

Welch, P. 1967, Audio and Electroacoustics, IEEE Transactions on, 15, 70

Wieczorek, M. A. & Simons, F. J. 2005, Geophysical Journal International, 162, 655

Chapter 3

Measuring Distance-ratios with CMB-galaxy Lensing Cross-Correlations

Abstract

We propose a method for cosmographic measurements by combining gravitational lensing of the cosmic microwave background (CMB) with cosmic shear surveys. We cross-correlate the galaxy counts in the lens plane with two different source planes: the CMB at $z \sim 1100$ and galaxies at an intermediate redshift. The ratio of the galaxy count/CMB lensing cross-correlation to the galaxy count/galaxy lensing cross correlation is shown to be a purely geometric quantity, depending only on the distribution function of the source galaxies. By combining Planck, ADEPT and LSST the ratio can be measured to $\sim 4\%$ accuracy, whereas a future polarization based experiment like CMBPOL can make a more precise ($\sim 1\%$) measurement. For cosmological models where the curvature and the equation of state parameter are allowed to vary, the direction of degeneracy defined by the measurement of this ratio is different from that traced out by Baryon Acoustic Oscillation (BAO) measurements. Combining this method with the stacked cluster mass reconstruction cosmography technique as

proposed by Hu, Holz and Vale (2007), the uncertainty in the ratio can be further reduced, improving the constraints on cosmological parameters. We also study the implications of the lensing-ratio measurement for early dark energy models, in context of the parametrization proposed by Doran and Robbers (2006). For models which are degenerate with respect to the CMB, we find both BAO and lensing-ratio measurements to be insensitive to the early component of the dark energy density.

3.1 Introduction

Weak gravitational lensing of the cosmic microwave background (CMB) (see Lewis & Challinor (2006) for a review) provides us with a unique opportunity to study the large scale distribution of dark matter in the universe out to much greater distances than accessible through conventional galaxy-lensing studies. It has been shown (Jain & Taylor, 2003) that by studying the gravitational lensing of galaxies in different redshift slices by the same foreground structures, the geometry of the universe and eventually, dark energy evolution may be constrained — a method known as cross-correlation cosmography. In this paper, we propose a similar method in which we treat the CMB as one of the background slices. This not only provides an extremely well standardized distance to compare other distances to, but also incorporates the longest possible distance in the ratio of distances probed by this method, making it a more sensitive probe of cosmological parameters than ratios involving distances restricted to galaxy surveys. Recently, Hu et al. (2007) have proposed a method for measuring the same lensing-ratio by comparing the convergence profile of the a cluster reconstructed via background galaxy shear with that reconstructed via CMB lensing, and then stacking several clusters to improve the precision of the measurement. The method we propose here depend on cross-correlations rather than reconstruction of convergence of individual objects, and will have different systematics. As such, this method is a powerful complement to the cluster-lensing based method and the two may be combined to obtain more precise measurements of the ratio.

3.2 Lensing Ratio: The key observable

Cosmological weak lensing effects are conveniently encoded in the effective convergence field, which is defined as a weighted projection of the matter overdensities δ (Bartelmann & Schneider, 2001),

$$\kappa(\hat{\mathbf{n}}) = \frac{3}{2}\Omega_{\rm m}H_0^2 \int d\eta d_A^2(\eta)\frac{g(\eta)}{a(\eta)}\delta(d_A(\eta)\hat{\mathbf{n}},\eta), \tag{3.1}$$

with

$$g(\eta) = \frac{1}{d_A(\eta)}\int_\eta^\infty d\eta' W_b(\eta')\frac{d_A(\eta'-\eta)}{d_A(\eta')} \tag{3.2}$$

where $d_A(\eta)$ is the comoving angular diameter distance corresponding to the comoving distance η. Here, $a(\eta)$ is the scale factor, while $\Omega_{\rm m}$ and H_0 represent the present values of the matter density parameter and the Hubble parameter, respectively. The quantity $g(\eta)$ represents the fact that sources are distributed in comoving distance with a normalized distribution function W_b. Since the CMB photons all come from nearly the same cosmological distance, we can approximate the source distribution function as, $W_b(\eta) \simeq \delta(\eta-\eta_0)$, giving

$$g_{\rm CMB}(\eta) = \frac{d_A(\eta_0-\eta)}{d_A(\eta_0)d_A(\eta)}, \tag{3.3}$$

where η_0 is the comoving distance to the last scattering surface. We will denote the same quantity for a background galaxy population with redshift distribution $p_g(z)dz = W_b(\eta)d\eta$, with the symbol $g_{\rm gal}(\eta)$.

We also consider a suitable foreground population as a tracer of large-scale structure. The projected fractional overdensity of the tracers can be written as,

$$\Sigma(\hat{\mathbf{n}}) = \int d\eta W_f(\eta)\delta_g(\eta\hat{\mathbf{n}},\eta), \tag{3.4}$$

where δ_g represents the fractional tracer overdensity and W_f is the normalized tracer distribution function in comoving distance. We assume that the Fourier modes of the tracer overdensity field are related to those of the underlying matter density field via a scale and redshift dependent bias factor, so that $\delta_g(\mathbf{k},\eta) = b(k,\eta)\delta(\mathbf{k},\eta)$. If we cross-correlate the tracer overdensity map with the convergence field, we obtain the cross power spectrum,

$$C_\ell^{\kappa\Sigma} = \frac{3}{2}\Omega_m H_0^2 \int d\eta b_\ell(\eta) W_f(\eta)\frac{g(\eta)}{a(\eta)}P(\frac{\ell}{d_A},\eta), \tag{3.5}$$

where we have used the Limber approximation and the orthogonality of spherical harmonics. We have also introduced the shorthand notation, $b_\ell(\eta) \equiv b(\frac{\ell}{d_A}, \eta)$.

Now, we will introduce two separate cross-correlation measures involving the foreground tracer population. First, we consider the case for the CMB as the background source. By constructing estimators out of quadratic combinations of CMB fields (temperature and polarization), it possible to obtain a noisy reconstruction of the convergence field (note that the actual observable in this case is the deflection field) out to the last scattering surface (Hu & Okamoto, 2002; Hirata & Seljak, 2003), which we denote as $\kappa_{\rm CMB}$. The power spectrum of the noise in the reconstruction, $N_\ell^{\kappa_{\rm CMB}\kappa_{\rm CMB}}$, can be estimated knowing the specifications for the CMB experiment. The cross-correlation of the reconstructed convergence field from the lensed CMB with the foreground tracer, gives the signal,

$$C_\ell^{\kappa_{\rm CMB}\Sigma} = \frac{3}{2}\Omega_m H_0^2 \int d\eta b_\ell(\eta) W_f(\eta) \frac{g_{\rm CMB}(\eta)}{a(\eta)} P(\frac{\ell}{d_A}, \eta), \tag{3.6}$$

where we have used the source distribution kernel $g_{\rm CMB}$ appropriate for the CMB being the background source.

Next, we consider the case for the weak lensing of background galaxies. The relevant observable in this case is the traceless symmetric shear field on the sky, the measurement of which allows a noisy reconstruction of the convergence field appropriate to the background galaxy distribution, $\kappa_{\rm gal}$. In this case, the noise is primarily due to intrinsic ellipticity of the background galaxies and has the spectrum, $N_l^{\kappa_{\rm gal}\kappa_{\rm gal}} = \left\langle \gamma_{\rm int}^2 \right\rangle / \bar{n}$ where $\left\langle \gamma_{\rm int}^2 \right\rangle^{1/2} \sim 0.3$ and $\bar{n}$ is the number of background galaxies per steradian (Kaiser, 1992). If we cross correlate this convergence field with the foreground tracers, we find the signal,

$$C_\ell^{\kappa_{\rm gal}\Sigma} = \frac{3}{2}\Omega_m H_0^2 \int d\eta b_\ell(\eta) W_f(\eta) \frac{g_{\rm gal}(\eta)}{a(\eta)} P(\frac{\ell}{d_A}, \eta), \tag{3.7}$$

where we have used the source distribution kernel, $g_{\rm gal}$ appropriate for background galaxies.

If the foreground distribution is narrow in redshift so that it can be approximated by a delta function, $W_f(\eta) \simeq \delta(\eta - \eta_f)$, then the ratio of the above two cross-correlation measures, which we call the lensing-ratio, reduces to,

$$r \equiv \frac{C_\ell^{\kappa_{\rm CMB}\Sigma}}{C_\ell^{\kappa_{\rm gal}\Sigma}} = \frac{g_{\rm CMB}(\eta_f)}{g_{\rm gal}(\eta_f)} \tag{3.8}$$

which is simply the geometrical ratio of the source distribution kernels. If the background galaxy distribution, too, is sufficiently narrow in redshift around $z = z_{gal}$, this becomes,

$$r = \frac{d_A(\eta_0 - \eta_f) d_A(\eta_{\rm gal})}{d_A(\eta_{\rm gal} - \eta_f) d_A(\eta_0)}. \tag{3.9}$$

Note that this is independent of the angular scale, tracer bias and the power spectrum. Therefore, measurements at several multipoles can be combined to constrain the lensing-ratio. Since the distance ratios depend on the cosmology and specifically on the dark energy model, this can be used to constrain dark energy parameters.

3.3 Upcoming surveys and a new probe of dark energy and curvature

Large scale structure surveys, together with precision measurements of the CMB anisotropies have already provided us with a wealth of knowledge about the geometry, evolution and composition of the Universe. In the coming decade, Cosmologists will carry out even larger scale galaxy and lensing surveys and produce higher resolution CMB maps. We consider a combination of three experiments in order to assess how well the lensing-ratio can be measured in such future surveys. We consider the redshift slice of foreground tracers (lenses) to be drawn from an ADEPT-like [1] large scale structure survey and the background (source) galaxies taken from an LSST-like [2] weak lensing experiment. For the CMB lensing measurements, we consider the upcoming Planck mission as well as a prospective polarization-based mission like CMBPOL.

The foreground galaxy slice is taken as a step function in the redshift range $(0.8, 0.9)$ with 350 galaxies per square degree. The source galaxies are also assumed to be distributed uniformly in redshift, between $z = 1.2$ and 1.6 with a number density of 40 galaxies per square arcmin. We model Planck to be a $7'$ FWHM instrument with temperature and polarization sensitivities of 28 and 57 μK-arcmin, respectively. For CMBPOL, we adopt

[1] Advanced Dark Energy Physics Telescope; http://universe.nasa.gov/program/probes/adept.html
[2] Large Synoptic Survey Telescope; http://www.lsst.org

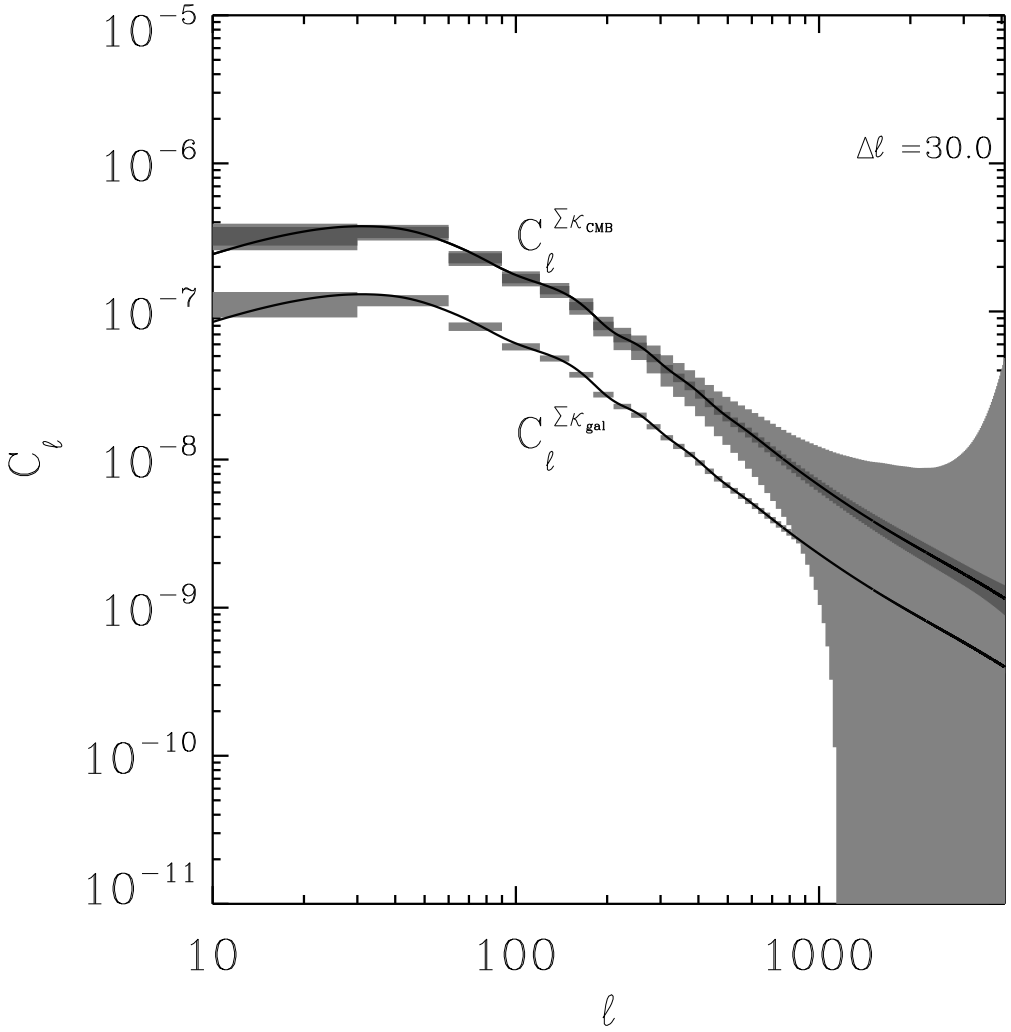

Figure 3.1: Cross power spectra, the ratio of which is being studied (cf. equation 3.8). Also shown are predicted 1σ errors in uniform bins of size $\Delta\ell = 30$. For the $C_\ell^{\Sigma\kappa_{\rm CMB}}$ case, the outer (lighter) errors correspond to lensing reconstruction using temperature and polarization with Planck, while the inner (darker) ones correspond to the same for CMBPOL.

a $3'$ beam FWHM and temperature and polarization sensitivities of 1 and 1.4 μK-arcmin, respectively. We assume that both CMB experiments cover 65% of the sky and all cross-correlations are performed over the same area. For calculations performed here we assumed a WMAP 5-year normalized ΛCDM cosmology with $\Omega_{\rm b}h^2 = 0.0227$, $\Omega_{\rm CDM}h^2 = 0.1099$, $\Omega_\Lambda = 0.742$, $\tau = 0.087$, $n_s = 0.963$ and $A_s = 2.41 \times 10^{-9}$.

In Fig. 3.1, we display the two cross power spectra appearing in the defining equation (3.8) of the lensing ratio along with binned uncertainties predicted from the experimental specifications.

The error on the ratio can be obtained as follows. We begin by defining the log-likelihood,

$$\chi^2(r) = \sum_\ell \frac{Z_\ell^2}{\sigma^2(Z_\ell)} \tag{3.10}$$

where, $Z_\ell = C_\ell^{\kappa_{\rm CMB}\Sigma} - rC_\ell^{\kappa_{\rm gal}\Sigma}$. We compute the variance of Z_l at the value r_0 of r computed in the fiducial cosmology,

$$\begin{aligned}\sigma^2(Z_\ell) &= \frac{1}{(2\ell+1)f_{\rm sky}}\Big[\tilde{C}_\ell^{\,\kappa_{\rm CMB}\kappa_{\rm CMB}}\tilde{C}_\ell^{\,\Sigma\Sigma} + (C_\ell^{\kappa_{\rm CMB}\Sigma})^2 \\ &\quad + r_o^2\left(\tilde{C}_\ell^{\,\kappa_{\rm gal}\kappa_{\rm gal}}\tilde{C}_\ell^{\,\Sigma\Sigma} + (C_\ell^{\kappa_{\rm gal}\Sigma})^2\right) \\ &\quad -2r_0\left(C_\ell^{\kappa_{\rm CMB}\kappa_{\rm gal}}\tilde{C}_\ell^{\,\Sigma\Sigma} + C_\ell^{\kappa_{\rm CMB}\Sigma}C_\ell^{\kappa_{\rm gal}\Sigma}\right)\Big]\end{aligned} \tag{3.11}$$

where,

$$\tilde{C}_\ell^{\,XX} = C_\ell^{XX} + N_\ell^{XX}$$

include the noise power spectra. The Poisson noise for the foreground tracer is taken as $N_\ell^{\Sigma\Sigma} = 1/\bar{n}_f$. Then maximum likelihood estimate for the ratio is then obtained by solving $\partial\chi^2(r)/\partial r = 0$ to be,

$$\hat{r} = \frac{\sum_\ell C_\ell^{\kappa_{\rm CMB}\Sigma}C_\ell^{\kappa_{\rm gal}\Sigma}/\sigma^2(Z_\ell)}{\sum_\ell (C_\ell^{\kappa_{\rm gal}\Sigma})^2/\sigma^2(Z_\ell)} \tag{3.12}$$

Now, we can estimate the error on r as,

$$\frac{1}{\sigma^2(\hat{r})} = \frac{1}{2}\frac{\partial^2\chi^2(r)}{\partial r^2} = \sum_\ell \frac{(C_\ell^{\kappa_{\rm gal}\Sigma})^2}{\sigma^2(Z_\ell)}. \tag{3.13}$$

Various auto, cross and noise power spectra that enter the calculation of the error on r are shown in Fig. 3.2. The above figures borne out the expected feature that the noise power

Experiment	Type	$(S/N)^{cross}$	$\Delta r/r(\%)$
Planck	POL	25.8	3.8
	TT	23.3	4.2
CMBPOL	POL	102.6	1.0
	TT	84.5	1.2

Table 3.1: Predictions for the cross-correlation studies described in the text with foreground galaxies from ADEPT, background galaxies from LSST and different CMB experiments. The quantity $(S/N)^{cross}$ represents the signal-to-noise ratio in the estimation of the cross correlation between the foreground tracer density with CMB lensing. The last column shows percentage error in the lensing-ratio estimator, r of equation (3.8). We show the prediction for both temperature based (TT) and polarization based (POL) reconstruction of the deflection field from the lensed CMB.

spectrum in the lensing reconstruction is the largest source of uncertainty that propagates into the error on r.

The estimated errors on r are shown in Table 3.1. For Planck, we find that the lensing-ratio can be estimated to $\sim 4\%$ while with CMBPOL a $\sim 1\%$ measurement is possible.

3.4 Parameter constraints

For Planck priors, improvements on cosmological parameter constraints upon adding the lensing-ratio to the primary CMB observables become appreciable when the error on the ratio decreases below 10% (Hu et al., 2007). It is interesting to note here that the method for estimating the lensing-ratio proposed by Hu et al. (2007), which relies on cluster mass reconstruction can be further improved with the maximum likelihood based estimator proposed by Yoo & Zaldarriaga (2008) and can complement the method proposed here. By combining the two methods for the same redshift slices, it may be possible to reduce the uncertainty in the lensing-ratio to percent or sub-percent levels.

In order to assess how a percent-level measurement of the ratio will help constrain a set of cosmological parameters $\{p_i\}$ in conjunction with the CMB experiments, we define a

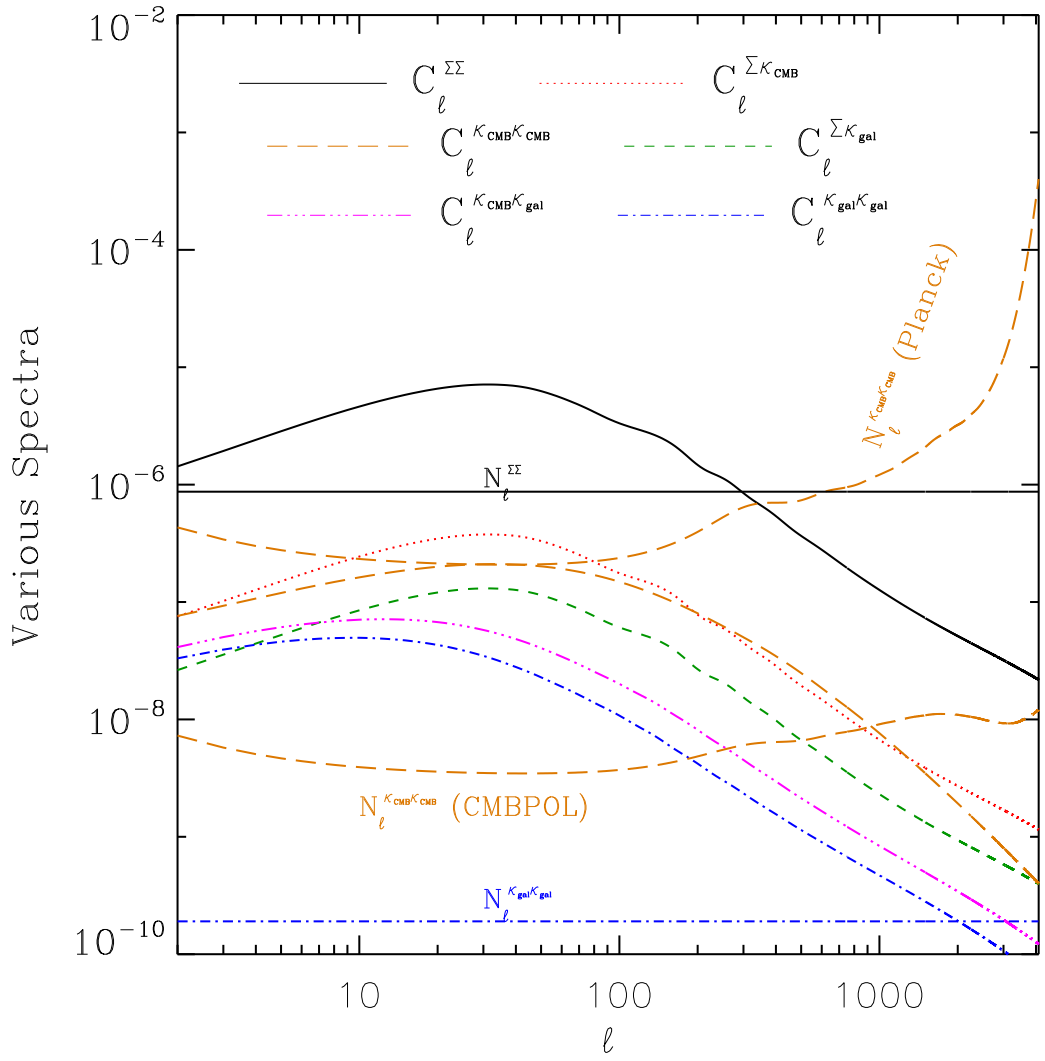

Figure 3.2: Various power spectra that enter the calculation of the error on the lensing ratio (cf. eq. 3.13). Each of the noise power spectra has been plotted with the same line style as its corresponding signal power spectrum and labeled as N_ℓ. The noise spectrum for the CMB lensing reconstruction has been indicated both for Planck and CMBPOL.

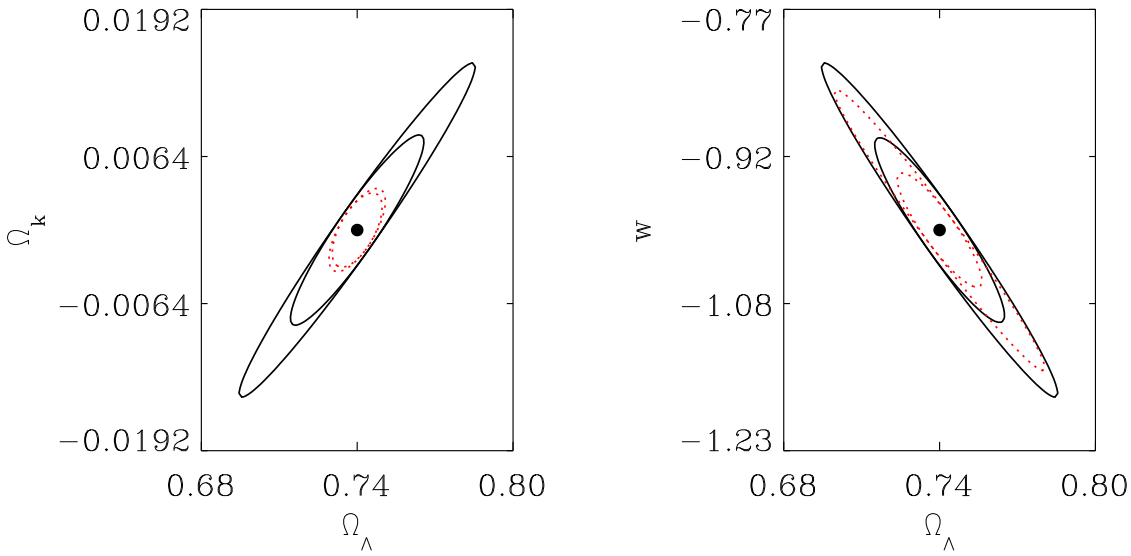

Figure 3.3: *Left Panel*: Improvements of constrains in the $\Omega_k - \Omega_\Lambda$ plane for a vacuum energy model with Planck by adding a 1% measurement of the lensing-ratio. The outer solid contour is the 68% confidence interval from primary CMB alone while the inner solid contour is the same after adding the lensing-ratio. The dotted contours have the same interpretation but represent the case where information from lensing extraction has been added to the CMB Fisher matrix. *Right Panel:* Same as left, but for the $w - \Omega_\Lambda$ plane, assuming flatness.

Fisher matrix for the lensing-ratio,

$$F_{ij}^{r} = \frac{\partial \ln r}{\partial p_i} \frac{1}{\sigma^2(\ln r)} \frac{\partial \ln r}{\partial p_j}. \tag{3.14}$$

and add it to the Fisher matrix from a CMB experiment. The error in a parameter is then estimated from the inverse of the combined Fisher matrix as $\sigma(p_i) = \sqrt{[\mathbf{F}^{-1}]_{ii}}$. We consider two variants of the CMB Fisher Matrix, one with only the primordial power spectra and the other with the power spectra involving the weak lensing deflection field extracted from CMB lensing measurements (Lesgourgues et al., 2006; Perotto et al., 2006). We do not consider any foreground contamination in any of these. Fig. 3.3 shows the constraints predicted with Planck specifications and a 1% error on the lensing-ratio, for minimal extensions to the standard 6-parameter model. These constrains are marginalized over all other parameters. The constraints on curvature assuming $w = -1$ and on w assuming flatness, both improve over the primary CMB case after adding in the ratio. For CMB with lensing extraction the

improvement on w is still substantial while that on Ω_k is marginal.

Following Lesgourgues et al. (2006), we also consider a more general 11-parameter model with w, fraction of dark matter in massive neutrinos f_ν, the effective number of neutrino species, the running of the spectral index and the primordial Helium fraction. We adopt a fiducial value of 0.1 eV for the total neutrino mass. The constraints on the interesting subspace of parameters are shown in Fig. 3.4. We find in this case that adding in the ratio significantly improves the constraints on w and f_ν over the primary CMB case. In fact, for w and Ω_Λ the improvements surpass those from the lensed CMB Fisher matrix. This is particularly interesting because the lensed-CMB-only constraints require an estimate of the convergence field from the four point function in the lensed CMB itself and is more prone to systematics than the cross-correlations that enter the ratio calculation. From Fig. 3.4, it is apparent that for the CMB Fisher matrix with lensing extraction the constraint on the neutrino mass is rather tight, so that no further gain is obtained by adding in the lensing-ratio. It is important to keep in mind that Fisher matrix methods tend to overestimate the error on neutrino mass due to non-Gaussianity in the associated likelihood (Perotto et al., 2006). Therefore, the errors estimated here are somewhat higher than those predicted from a full Monte-Carlo forecast.

We next consider models with curvature and a free dark energy parameter w. CMB measurements allow for a large degenerate valley in the $w - \Omega_k$ plane making Fisher Matrix results deceptive. We treat this model by imposing a strong CMB prior in which we explore the parameter space while keeping the high-redshift variables $\Omega_{\rm b}h^2$, $\Omega_m h^2$ and $\theta_A = r_s(z_0)/d_A(\eta_0)$ fixed. For each degenerate parameter set, we calculate the value of r as well as the spherically averaged baryon acoustic oscillation (BAO) distance ratio (Percival et al., 2007; Eisenstein et al., 2005), $r_s(z_d)/D_v(z)$, where r_s is the comoving sound horizon scale at the drag epoch, z_d and D_v is an effective distance measure to redshift z. We compute it for $z = 1.5$, a typical median redshift for an ADEPT-like survey. The constraints in the $w-\Omega_k$ plane from each of these methods are shown in Fig 3.5 for a 0.4% measurement of the BAO ratio with ADEPT (Seo & Eisenstein, 2007) combined with a 1% measurement of

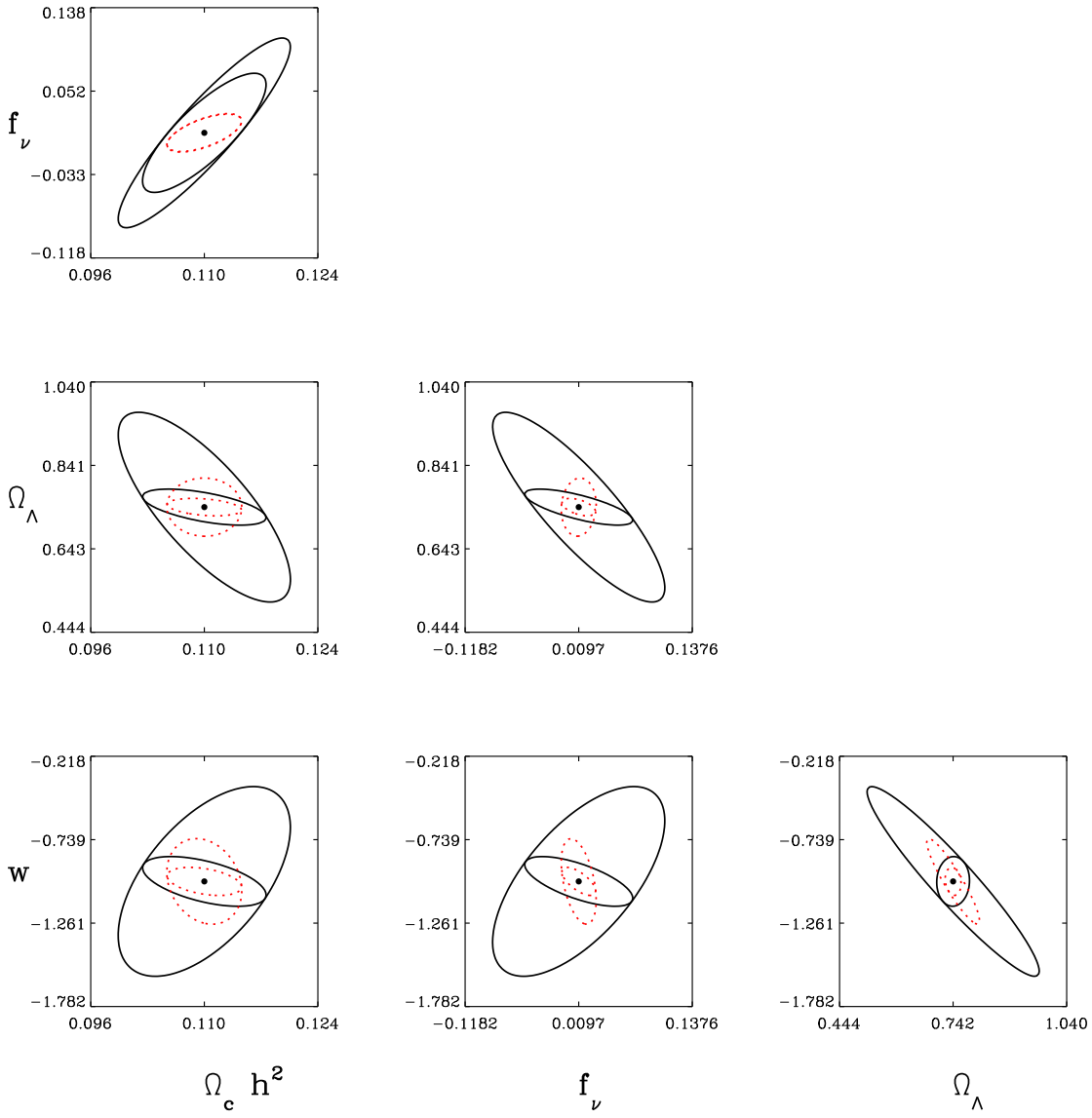

Figure 3.4: Improvements in the constraints on the interesting subset of parameters in the eleven parameter model involving massive neutrinos and free dark-energy equation of state (see text). The interpretations of the contours are same as in Fig. 3.3

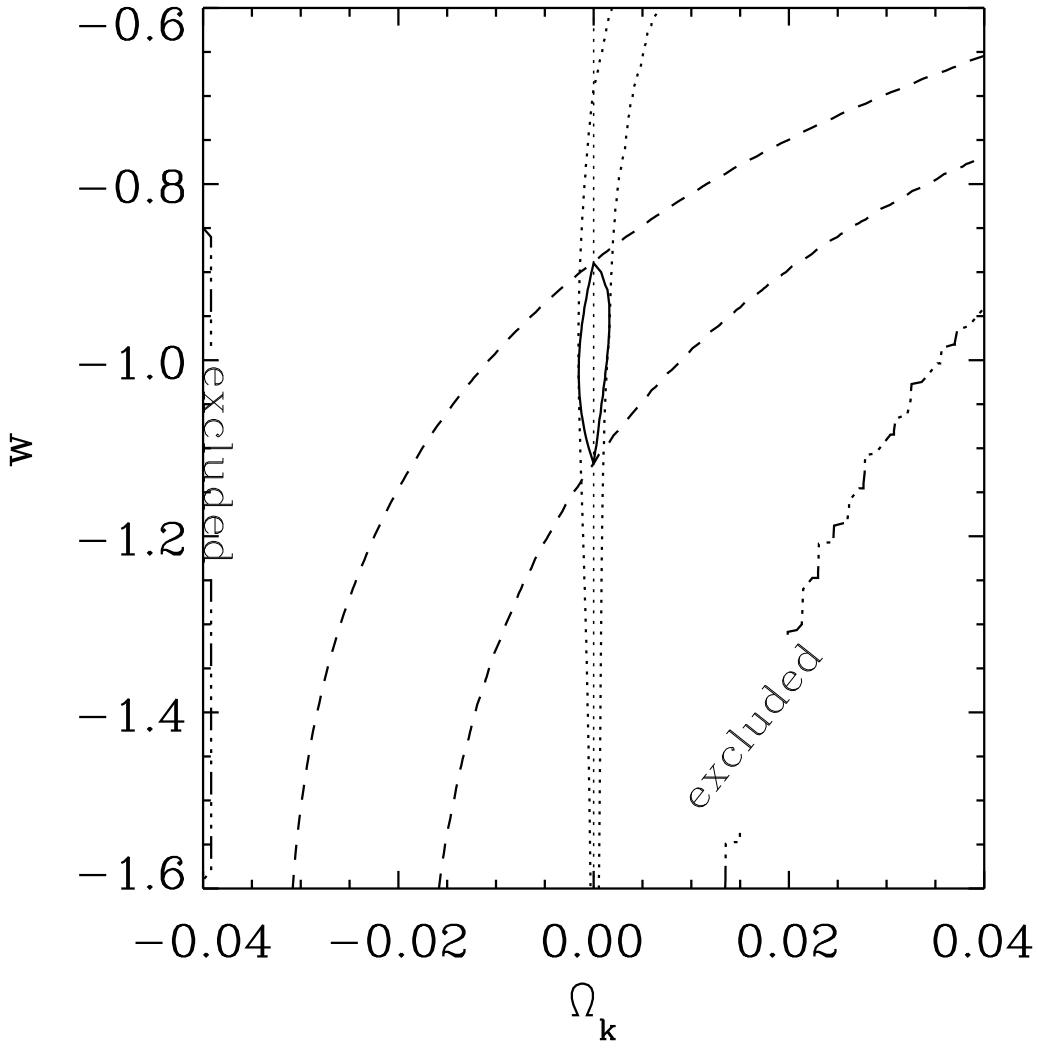

Figure 3.5: Constraints (68%) in the w-Ω_k plane from BAO and lensing-ratio measurements. The dashed line indicate constraints from the lensing-ratio while the dotted line represents the same for the BAO ratio. The solid contour shows the joint constraint. Regions outside the contours labeled "excluded" are not allowed due to the strong CMB prior (see text).

the lensing-ratio. We find that the degeneracy direction for the BAO is quite different from that for the lensing-ratio. Together they can put a $\sim 0.01\%$ limit on Ω_k and a simultaneous $\sim 10\%$ limit on w, without adding in any other cosmological prior.

Next, we turn to scenarios with early dark energy. In particular, we choose the dark energy parametrization proposed by Doran & Robbers (2006), namely,

$$\Omega_d(a) = \frac{\Omega_d^0 - \Omega_d^e(1 - a^{-3w_0})}{\Omega_d^0 + \Omega_m^0 a^{3w_0}} + \Omega_d^e(1 - a^{-3w_0}) \tag{3.15}$$

where Ω_d^0 is the present value of the dark energy density function, $\Omega_d(a)$, and Ω_d^e is its asymptotic value at high redshift. In this parametrization, the dark energy equation of state $w(a)$ has the value w_0 at present, crosses over to $w \simeq 0$ during matter domination and goes to $w \simeq 1/3$ in the radiation dominated era. Two relations of interest in this model that follow from the definition of the Hubble parameter,

$$H^2(a) = H_0^2 \frac{(\Omega_{\rm m} a^{-3} + \Omega_r a^{-4})}{1 - \Omega_d(a)} \tag{3.16}$$

are the scaling, with Ω_d^e, of the comoving sound horizon at last scattering or the drag epoch, namely,

$$r_s(\Omega_d^e) = \sqrt{1 - \Omega_d^e}\ \ r_s(\Omega_d^e = 0), \tag{3.17}$$

and the behavior of the comoving angular diameter distance which, for flat cosmologies, given by,

$$d_A(z) = \frac{c}{H_0} \int_0^z dz \frac{\sqrt{1 - \Omega_d(z)}}{[\Omega_{\rm m}(1+z)^3 + \Omega_r(1+z)^4]^{1/2}}. \tag{3.18}$$

We consider the parameter space spanned by (w_0, Ω_d^e) and study how well it can be constrained given measurements of the lensing ratio, the CMB and the BAO. We again impose the strong CMB prior, and compute the observables for each point in the (w_0, Ω_d^e) space degenerate with respect to the CMB. Since early dark energy shifts the comoving sound horizon according to equation (3.17), and we are fixing the values $\Omega_{\rm m} h^2$ and $\Omega_b h^2$ (which fixes the redshift of last scatter), equation (3.18) immediately implies that the only way to keep the angular scale $\theta_A = r_s(z_0)/d_A(\eta_0)$ constant is by varying Ω_d^0 such that d_A scales like $\sqrt{1 - \Omega_d^e}$. Thus, quite counter-intuitively, we find that the early value of the dark energy

indirectly affects low redshift evolution. An unfortunate consequence of this is that both BAO and lensing ratio measurements are rendered insensitive to the value of Ω_d^e. As shown by Linder & Robbers (2008), it is possible to have a set of cosmological models degenerate with respect to the CMB without having $\Omega_{\rm m}h^2$ strictly constant. For example, holding $\Omega_{\rm m}$, and therefore Ω_d^0 constant, it is still possible to have nearly indistinguishable CMB power spectra. In this case, to preserve θ_a, one has to change h accordingly. This, again, leads to the shift in low redshift distances and makes our observables insensitive to Ω_d^e. These issues are discussed in some detail in the Appendix.

3.5 Conclusions

We have proposed a way of measuring a ratio of comoving angular diameter distances that appear in the lensing kernels for CMB and galaxy lensing. By combining Planck, ADEPT and LSST, it is possible make a percent level measurement of this ratio. A polarization based experiment like CMBPOL has the potential of making a more precise measurement. The precision in the measurement can be potentially increased by combining it with cluster mass reconstruction based measurement of the same quantity. The ratio is sensitive to late-time geometry and composition of the Universe and a percent level measurement combined with Planck data can provide interesting constraints and consistency checks, independently of other cosmological probes. By choosing the CMB as one of the lens planes, this method allows higher redshifts to be probed than galaxy-lensing cosmography.

While the distance ratio is sensitive to late time dark energy, we find it to be rather insensitive to early dark energy, particularly for the parametrization proposed in Doran & Robbers (2006). As discussed in the Appendix, when a strong CMB prior is imposed, the values of low redshift parameters shift in conjunction with the asymptotic high redshift value of early dark energy in such a manner as to render both the BAO ratio and the lensing ratio rather insensitive probes. This behavior is most likely a specific feature of the said parametrization. The effectiveness of the lensing ratio as a cosmological tool for a wider class of quintessence models remains to be studied.

3.A BAO and lensing ratios as probes of early dark energy

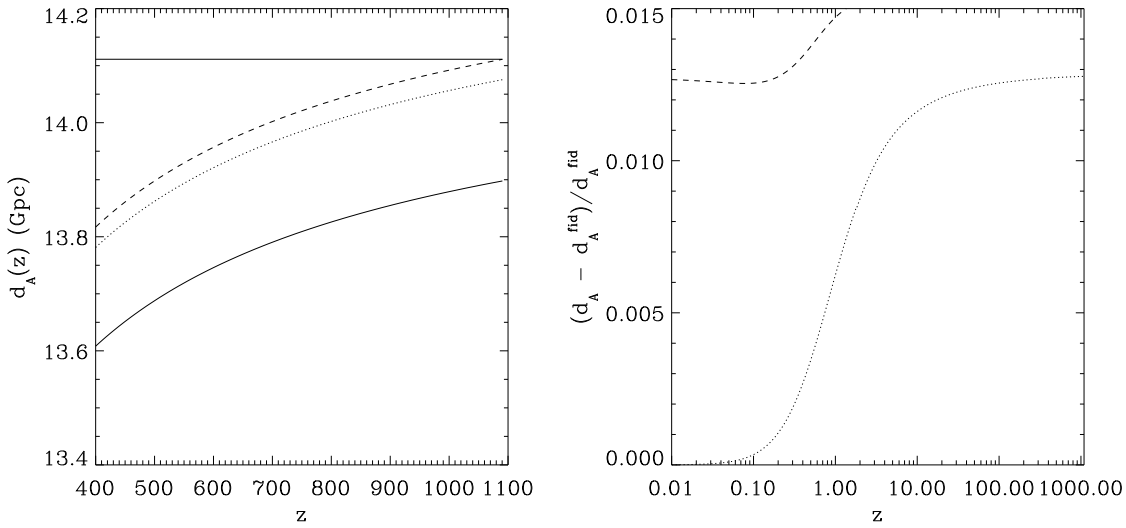

Figure 3.A.1: *Left:* Comoving angular diameter distance at the high redshift end for various models. The solid curve corresponds to the fiducial early dark energy model with $\Omega_d^0 = 0.742$, $w_0 = -1$ and $\Omega_d^e = 0.03$. The horizontal line indicates the value of $d_A(z_0)$ at the last scattering surface required by a wrong model with $\Omega_d^e = 0$, to keep the CMB angular scale, θ_A, constant. The dotted line represents a model with all parameters kept same as the fiducial model, except Ω_d^e which is set to zero. This falls short of the required $d_A(z_0)$ and hence the only free parameter in the model, Ω_d^0, has to be adjusted to achieve the required $d_A(z_0)$. The final model that would be wrongly inferred by matching the CMB acoustic scale, has $\Omega_d^0 = 0.735$ and is shown by the dashed line. *Right:* Fractional difference in the comoving angular diameter distance $d_A(z)$ from the fiducial model. The dotted line represents the fractional error for the same model as shown by the dotted line on the left plot. As expected the difference in this case goes to zero at low redshift. The dashed line shows fractional difference in the wrongly inferred model. Note that since this model had its Ω_d^0 shifted low, it overestimates the true distances by $\sim 1.5\%$ for $z \gtrsim 1$ and by 1.3% for $z \lesssim 0.5$.

Let us choose the fiducial dark energy model as one with $\Omega_d^0 = 0.742$, $w_0 = -1$ and $\Omega_d^e = 0.03$ with the other cosmological parameters set at the values described in the body of the paper. Now, if we had wrongly assumed $\Omega_d^e = 0$ i.e. a Λ model, then by fitting the CMB, we would find a set of parameters that would keep the angle $\theta_A = r_s(z_0)/d_A(z_0)$ constant. As $r_s \propto (1 - \Omega_d^e)^{1/2}$, we would find a model that overestimates the sound horizon and

hence the comoving angular diameter distance to the last scattering surface by the factor $(1-0.03)^{-1/2} \simeq 1.015$ i.e. by 1.5%. In particular, if we also impose the strong constraint that $\Omega_{\rm m}h^2$ is a constant, this model would have a value of Ω_d^0 that would be slightly lower than the true value, namely ~ 0.735. This would, in turn, make us overestimate the value of $d_A(z)$ to all redshifts (see Fig. 3.A.1).

Now consider the BAO ratio at some redshift z_{BAO}. For the sound horizon at the drag epoch, we would again make an overestimate by the same factor, $\sim 1.5\%$. But at the same time, we overestimate $d_A(z_{BAO})$ or $c/H(z_{BAO})$ by an almost similar factor because Ω_d^0 has shifted (see Figs. 3.A.1 & Figs. 3.A.2). Therefore, the transverse ratio $r_s(z_D)/d_A(z_{BAO})$ or the line-of-sight ratio $r_s(z_D)H(z_{BAO})$ estimated in the wrong model will be rather close to the true values, thereby making it hard to detect the presence of early dark energy. In fact, these figures show that deviations from the fiducial ratio occur only at the 0.2% level at $z \lesssim 0.5$. Because the angular scale of the CMB acoustic peak is a precisely measured quantity, it is expected that even if the strong CMB prior is relaxed, a MCMC type exploration of the parameter space would reveal a similar insensitivity of the BAO to Ω_d^e (Doran et al., 2007).

For the lensing ratio, the situation is even worse, as depicted in the right panel of Fig. 3.A.2. Here, due to overall shift of all distance scales, the difference between the inferred and the true model is less than 0.1% at all lens redshifts.

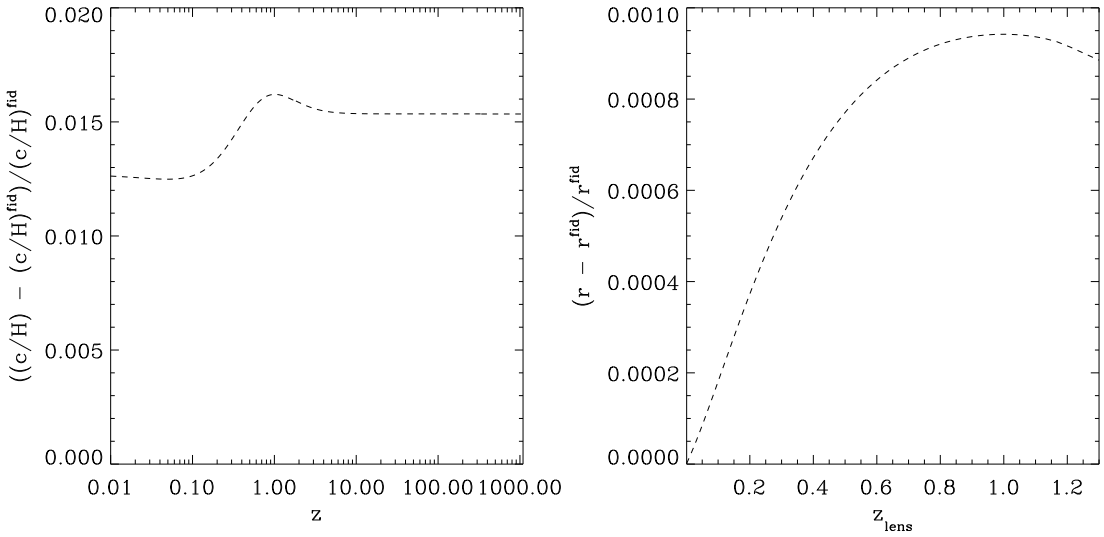

Figure 3.A.2: *Left:* Fractional difference from the fiducial of the Hubble scale $c/H(z)$ in the wrongly inferred model of Fig. 3.A.1. *Right:* Same as left, for the lensing ratio as a function of the lens redshift.

References

Bartelmann, M. & Schneider, P. 2001, Phys. Rep., 340, 291

Doran, M. & Robbers, G. 2006, Journal of Cosmology and Astro-Particle Physics, 6, 26

Doran, M., Stern, S., & Thommes, E. 2007, Journal of Cosmology and Astro-Particle Physics, 4, 15

Eisenstein, D. J., Zehavi, I., Hogg, D. W., Scoccimarro, R., Blanton, M. R., Nichol, R. C., Scranton, R., Seo, H.-J., Tegmark, M., Zheng, Z., Anderson, S. F., Annis, J., Bahcall, N., Brinkmann, J., Burles, S., Castander, F. J., Connolly, A., Csabai, I., Doi, M., Fukugita, M., Frieman, J. A., Glazebrook, K., Gunn, J. E., Hendry, J. S., Hennessy, G., Ivezić, Z., Kent, S., Knapp, G. R., Lin, H., Loh, Y.-S., Lupton, R. H., Margon, B., McKay, T. A., Meiksin, A., Munn, J. A., Pope, A., Richmond, M. W., Schlegel, D., Schneider, D. P., Shimasaku, K., Stoughton, C., Strauss, M. A., SubbaRao, M., Szalay, A. S., Szapudi, I., Tucker, D. L., Yanny, B., & York, D. G. 2005, ApJ, 633, 560

Hirata, C. M. & Seljak, U. 2003, Phys. Rev. D, 67, 043001

Hu, W., Holz, D. E., & Vale, C. 2007, Phys. Rev. D, 76, 127301

Hu, W. & Okamoto, T. 2002, ApJ, 574, 566

Jain, B. & Taylor, A. 2003, Physical Review Letters, 91, 141302

Kaiser, N. 1992, ApJ, 388, 272

Lesgourgues, J., Perotto, L., Pastor, S., & Piat, M. 2006, Phys. Rev. D, 73, 045021

Lewis, A. & Challinor, A. 2006, Phys. Rep., 429, 1

Linder, E. V. & Robbers, G. 2008, Journal of Cosmology and Astro-Particle Physics, 6, 4

Percival, W. J., Cole, S., Eisenstein, D. J., Nichol, R. C., Peacock, J. A., Pope, A. C., & Szalay, A. S. 2007, MNRAS, 381, 1053

Perotto, L., Lesgourgues, J., Hannestad, S., Tu, H., & Y Y Wong, Y. 2006, Journal of Cosmology and Astro-Particle Physics, 10, 13

Seo, H.-J. & Eisenstein, D. J. 2007, ApJ, 665, 14

Yoo, J. & Zaldarriaga, M. 2008, ArXiv e-prints, 805

Chapter 4

CMB Lensing and the WMAP Cold Spot

Abstract

Cosmologists have suggested a number of intriguing hypotheses for the origin of the "WMAP cold spot", the coldest extended region seen in the CMB sky, including a very large void and a collapsing texture. Either hypothesis predicts a distinctive CMB lensing signal. We show that the upcoming generation of high resolution CMB experiments such as ACT and SPT should be able to detect the signatures of either textures or large voids. If either signal is detected, it would have profound implications for cosmology.

4.1 Introduction

One of the most intriguing features in the WMAP[1] (Bennett et al., 2003) maps of the microwave sky is the Cold Spot (Vielva et al., 2004; Cruz et al., 2005, 2006, 2007a). Under the standard assumption of statistically homogenous Gaussian random fluctuations, the *a posteriori* probability of finding such a feature on the last scattering surface is less than 2% (Cruz et al., 2005, 2006). The Cold Spot also appears to have a flat frequency spectrum

[1]Wilkinson Microwave Anisotropy Probe; http://map.gsfc.nasa.gov/

and is located in a region of low foreground emission, making it unlikely to be caused by Galactic foregrounds or the Sunyaev-Zel'dovich effect (Sunyaev & Zeldovich, 1970). This has led some theorists to speculate that the Cold Spot is a secondary effect, generated at some intermediate distance between us and the last scattering surface. One such model proposes that the Cold Spot may have been caused by the Rees-Sciama effect (Rees & Sciama, 1968) due to an underdense void of comoving radius $\sim 200h^{-1}$Mpc and fractional density contrast $\delta \sim -0.3$ at redshift of $z \lesssim 1$ (Inoue & Silk, 2006, 2007). Interestingly, Rudnick et al. (2007) reported a detection of an underdense region with similar characteristics in the distribution of extragalactic radio sources in the NRAO VLA Sky Survey in the direction of the Cold Spot, a claim which has recently been challenged (Smith & Huterer, 2008). An alternative view (Cruz et al., 2007b) proposes that the spot was caused by the interaction of the CMB photons with a cosmic texture, a type of topological defect that can give rise to hot and cold spots in the CMB (Turok & Spergel, 1990). Bayesian analysis by Cruz et al. (2008) claims that the texture hypothesis seems to be favored over the void explanation, mainly because such large voids as required by the latter is highly unlikely to form in a ΛCDM structure formation scenario. Irrespective of whether the Cold Spot was caused by a void or a texture, the CMB photons interacting with such an entity would have been gravitationally deflected. The deflections would lead to a systematic remapping of the primordial CMB anisotropies in and around the Cold Spot. In this brief report, we use simple analytic models for the void and the texture to address the issue of detectability of the gravitational lensing signature of either model, using upcoming high resolution CMB experiments.

For calculations presented in this paper, we assume a WMAP 5-year (Dunkley et al., 2008) flat ΛCDM cosmology with a total matter density parameter $\Omega_m = 0.258$ and a vacuum energy density $\Omega_\Lambda = 0.742$. The spectral index of the primordial power spectrum is set to $n_s = 0.963$ and the primordial amplitude for curvature perturbations is taken as $A_s = 2.41 \times 10^{-9}$ at a pivot scale of $0.002h^{-1}$Mpc. The present value of the Hubble parameter is taken as $H_0 = 72$ km s^{-1} Mpc^{-1}.

4.2 Lensing by the Void

Gravitational redshift of photons passing through cosmic voids can produce decrements in the observed CMB temperature. This so-called Rees-Sciama effect (Rees & Sciama, 1968) has been proposed as a possible explanation for the existence of the Cold Spot by Inoue & Silk (2006, 2007). They assume a compensated spherical underdense region with fractional density contrast $\delta \sim -0.3$ at $z \sim 1$, and their analysis suggest that the comoving radius of the region required to explain the observed Cold Spot is $\sim 200h^{-1}$Mpc. An order of magnitude estimate by Rudnick et al. (2007) for a completely empty void ($\delta = -1$) at $z \lesssim 1$ puts the comoving radius at $\sim 120h^{-1}$Mpc. To put these dimensions in perspective, both observations (Hoyle & Vogeley, 2004; Patiri et al., 2006) and numerical simulations (Colberg et al., 2005; Platen et al., 2008) suggest that for $\delta \sim -0.8$ the typical void size tends to be around $\sim 10h^{-1}$Mpc. This means that a $\sim 100 - 200h^{-1}$Mpc void is extremely unlikely to form in the concordance cosmology. Nevertheless, if such a void does exist, its presence should also be apparent through the gravitational deflection of the CMB photons that pass through or near it.

Voids, especially the large ones, are seldom spherical and tend to show large axis ratios (Shandarin et al., 2006; Platen et al., 2008). We use this property to our advantage and model the void responsible for the Cold Spot as a homogeneous cylinder with its axis aligned along the line of sight. We take its comoving radius to be $r_v = 150$ Mpc and its comoving line of sight depth to be $L = 200$ Mpc. The mean redshift of the cylinder is taken to be $\bar{z} = 0.8$. Under the thin lens approximation (Bartelmann & Schneider, 2001), the simple geometry allows us to approximate the cylinder as a disc of surface underdensity $\Delta\Sigma = \delta \langle\Sigma\rangle$ at redshift $\bar{z}$, where $\langle\Sigma\rangle = \bar{\rho}L/(1+\bar{z})$, $\bar{\rho}$ being the physical background density of the universe at that redshift and $\delta < 0$ denotes the fractional density contrast. This places the cylinder at a comoving distance $D_L = 2770.3$ Mpc from us and makes its angular radius $R_V = 3.1°$. To describe a point on the lens plane, we set up a polar coordinate system (r, θ) on the lens plane, with the origin at the center of the disc. Here we treat r as an angular variable. Using the Gauss's Law for lensing and the circular symmetry of the problem, we can write

the solution for the effective deflection for a CMB photon as $\boldsymbol{\alpha}_V = \alpha_V(r)\hat{r}$ where,

$$\alpha_V(r) = \begin{cases} A_V r & \text{for } r < R_V. \\ A_V \frac{R_V^2}{r} & \text{for } r \geq R_V \end{cases} \tag{4.1}$$

with

$$\begin{aligned} A_V &= \frac{4\pi G}{c^2} |\delta| \langle \Sigma \rangle \frac{D_{LS}}{D_s} \frac{D_L}{(1+\bar{z})} \\ &= \frac{3}{2}\left(\frac{H_0}{c}\right)^2 |\delta| \, \Omega_m L \frac{D_{LS}}{D_s} D_L (1+\bar{z}) \\ &= 0.01785 \ \ |\delta| \end{aligned} \tag{4.2}$$

where in the last step we have substituted the adopted values of the parameters. Here, D_L and D_S are the comoving distances from the observer to the lens and the source plane (i.e., the last scattering surface). D_{LS} represents the comoving distance between the lens and the source.

Note that the void acts a diverging lens and the maximum deflection occurs at the edge of the void. For a perfectly empty void $\delta = -1$ the peak deflection has a value of $3.3'$, while for a void with moderate underdensity, $\delta \sim -0.3$ the maximum deflection is $\sim 1'$. We would like to point out here that the model of the void we have considered is uncompensated because we have not surrounded it with an overdense shell as is often done when modeling voids. Such a compensated void will have a similar deflection profile inside the void but the deflection angles will rapidly fall to zero at the outer edge of the compensating shell (Amendola et al., 1999). Since the void itself has a size of 6° and most of the detection algorithms we will discuss will depend on mapping the CMB in a roughly 8° square patch around it, the details of the deflection field outside a few degrees of the void will be unimportant for our order of magnitude estimate.

4.3 Lensing by the Texture

An alternate explanation for the anomalous Cold Spot entertains the possibility of a collapsing cosmic texture at $z \sim 6$ that interacted with the CMB photons (Cruz et al., 2007b).

Textures are cosmic defects that form when a simple Lie group, like SU(2), is completely broken (Turok, 1989). The formation and evolution of textures follow a scaling solution in which they collapse and unwind on progressively larger scales. A texture modifies the space-time metric around itself in such a manner that photons that cross it before collapse are redshifted, while those crossing after collapse are blueshifted. Therefore, depending on whether a texture that collapsed at some conformal time τ, was outside or inside the sphere defined by the currently detected CMB photons at the same time τ, we would observe a cold or a hot spot along the direction of the texture (Turok & Spergel, 1990). Incidentally, the texture would also produce gravitational deflection of the CMB photons interacting with it. Under the same spherically symmetric scaling approximation as adopted in Cruz et al. (2007b), it can be shown (Durrer et al., 1992) that to lowest order in the symmetry breaking energy scale, the deflection of a photon trajectory due to a texture can be written as $\boldsymbol{\beta} = -\beta(r)\hat{r}$, where

$$\beta(r) = 2\sqrt{2}\epsilon \frac{r/R_T}{\sqrt{1+4(\frac{r}{R_T})^2}}. \tag{4.3}$$

Here R_T is the characteristic angular scale of the texture, and is given by

$$R_T = \frac{2\sqrt{2}\kappa(1+z_T)}{E(z_T)\int_0^{z_T} dz/E(z)}, \tag{4.4}$$

where $E(z) = (\Omega_{\rm m}(1+z)^3 + \Omega_\Lambda)^{1/2}$, z_T is the redshift of the texture and κ is a fraction of unity. The amplitude of the deflection is set by $\epsilon = 8\pi^2 G\eta^2$ where η is the symmetry-breaking energy scale. Note that in writing the above equation, we have employed a similar co-ordinate system (r, θ) as we did for the void, on the plane transverse to the line of sight and having its origin at the texture center. The effective deflection angle $\boldsymbol{\alpha}_T = -\alpha_T(r)\hat{r}$, by which the CMB photons are remapped on the sky, is then given by,

$$\begin{aligned} \alpha_T(r) &= \frac{D_{LS}}{D_S}\beta(r) \\ &= A_T \frac{r}{\sqrt{1+4(\frac{r}{R_T})^2}}, \end{aligned} \tag{4.5}$$

with

$$A_T = \frac{2\sqrt{2}\epsilon}{R_T}\frac{D_{LS}}{D_S}. \tag{4.6}$$

Unlike the void, the texture acts as a converging lens.

Bayesian template fitting for a collapsing texture was performed by Cruz et al. (2007b) on the 3-year WMAP data around the Cold Spot using the analytic temperature decrement profile given in Turok & Spergel (1990). Their fit suggests a value of $\epsilon \sim 8 \times 10^{-5}$ for the amplitude and $R_T \sim 5^\circ$ for the scale parameter. The authors argue that their best fit value for ϵ is biased high due to noise and by performing the same template fitting on several simulated CMB maps with a cold texture spot in each, they find that the true amplitude is close to 4×10^{-5}, consistent with the upper bound, 5×10^{-5} inferred from the CMB power spectrum (Bevis et al., 2004). For the lensing template equation (4.5), we therefore adopt the values $\epsilon = 4 \times 10^{-5}$ and $R_T = 5^\circ$. Texture simulations put the value of κ appearing in equation (4.4) at ~ 0.1, which together with the adopted value of R_T imply the redshift of the texture to be $z \sim 6$. This, in turn gives $A_T = 5.19 \times 10^{-4}$. Note that the scaling profile in equation (4.5) is valid only for comoving distances $r \lesssim R_T$ and usually a Gaussian fall-off is assumed beyond this radius. We neglect this detail as we will be interested in detecting the signal on a patch of the order of the size of the Cold Spot. With the values of A_T and R_T deduced above, the peak deflection near the edge of the Cold Spot will be $\sim 0.1'$, more than an order of magnitude smaller than the corresponding value for the void. This can be understood with the following scaling argument. If $M_{<r}$ represents the mass or energy density interior to some radius r in the void or the texture, then the temperature decrement of the CMB photons will be of order the time rate of change of the potential, $GM_{<r}/(r\ t)$, t being a characteristic time scale. For the void, $t \sim t_H$, the Hubble time, whereas for the texture, the characteristic time scale is the light crossing time $t \sim r/c \ll t_H$. Therefore, to produce the same temperature decrement, the texture requires less energy density than the void, i.e. $M_{<r}^{texture} << M_{<r}^{void}$. Since the gravitational deflection $\alpha \sim GM_{<r}/r$, the deflection due to the texture is expected to be much smaller than that due to the void.

4.4 Can CMB Observations Detect Voids and Textures?

Several ongoing and upcoming CMB experiments have been designed to survey smaller sections of the CMB sky with much higher angular resolutions and sensitivities than ever before. For example, the Atacama Cosmology Telescope (ACT) [2] and the South Pole Telescope (SPT) [3] are designed to map roughly a tenth of the CMB sky at arcminute angular resolution and sensitivities of around 10 μK per arcminute sky pixel. In this section, we will estimate the significance with which the void or the texture hypothesis can be confirmed by studying their lensing signatures with a high resolution CMB experiment like ACT.

Gravitational lensing caused by massive objects on the line of sight between us and the last scattering surface produces coherent distortions of the small scale features in the CMB, much like the shape distortions of background galaxies due to the lensing by a cluster. The deflection field couples to the large scale gradients in the CMB and correlates the gradients with the small scale features. This property can be used to reconstruct the convergence profile of the lens, a subject that has been studied in detail over recent years (Seljak & Zaldarriaga, 2000; Hu & Okamoto, 2002; Hirata & Seljak, 2003; Dodelson, 2004; Vale et al., 2004; Maturi et al., 2005; Lewis & King, 2006; Hu et al., 2007; Yoo & Zaldarriaga, 2008). In our case, since the lensing template has been already defined by fitting the temperature decrement of the Cold Spot, we can approach the problem in a simpler manner: given a deflection template $\boldsymbol{\alpha}(\boldsymbol{r}) = \alpha(r)\hat{r}$, we ask how likely is it to be detected by a CMB experiment.

We begin by writing the lensed temperature field as,

$$\begin{aligned} \tilde{T}(\boldsymbol{r}) &= T\left(\mathbf{r} + \boldsymbol{\alpha}(r)\right) \\ &\simeq T(\mathbf{r}) + \frac{\partial T(\mathbf{r})}{\partial r}\alpha(r). \end{aligned} \tag{4.7}$$

We formulate the problem of detecting the template by introducing a coefficient to the template : $\alpha \rightarrow c\alpha$, and constructing the maximum likelihood estimator for c. The unlensed

[2] http://www.physics.princeton.edu/act/
[3] http://pole.uchicago.edu/spt/

temperature field can be written as,

$$\hat{T}(\mathbf{r}) \simeq \tilde{T}(\boldsymbol{r}) - c\frac{\partial \tilde{T}(\mathbf{r})}{\partial r}\alpha(r), \tag{4.8}$$

in terms of which, we can write the likelihood function as,

$$2\ln\mathcal{L} = \hat{T}^T(\mathbf{r})\mathbf{C}^{-1}\hat{T}(\mathbf{r}) \tag{4.9}$$

where $\mathbf{C}(\mathbf{r},\mathbf{r}') = \langle T(\mathbf{r})T(\mathbf{r}')\rangle$. This gives the following maximum likelihood estimator for c :

$$\hat{c} = \frac{\left[\frac{\partial\tilde{T}(\mathbf{r})}{\partial r}\alpha(r)\right]^T \mathbf{C}^{-1}\tilde{T}(\mathbf{r})}{\left[\frac{\partial\tilde{T}(\mathbf{r})}{\partial r}\alpha(r)\right]^T \mathbf{C}^{-1}\left[\frac{\partial\tilde{T}(\mathbf{r})}{\partial r}\alpha(r)\right]}. \tag{4.10}$$

By construction, $\langle c\rangle = 1$; therefore, the signal to noise for detection can be written as,

$$\begin{aligned}\left(\frac{S}{N}\right)^2 &= \frac{1}{\sigma_c^2} = \frac{1}{2}\left\langle\frac{\partial^2\ln\mathcal{L}}{\partial c^2}\right\rangle \\ &= \left\langle\left[\frac{\partial\tilde{T}(\mathbf{r})}{\partial r}\alpha(r)\right]^T \mathbf{C}^{-1}\left[\frac{\partial\tilde{T}(\mathbf{r})}{\partial r}\alpha(r)\right]\right\rangle.\end{aligned} \tag{4.11}$$

In the Fourier space $\boldsymbol{\ell}$ conjugate to $\mathbf{r}$, this becomes,

$$\left(\frac{S}{N}\right)^2 = \sum_\ell f_{\rm sky}\frac{(2\ell+1)}{2}\frac{S_\ell}{C_\ell + N_\ell}, \tag{4.12}$$

where we have replaced an integral by a sum and introduced the factor $f_{\rm sky}$, which is the fraction of sky area observed, to correct for the fact that all Fourier modes cannot be realized on a finite patch. Here,

$$S_\ell = \int \frac{d^2\boldsymbol{\ell}'}{(2\pi)^2}\left[\boldsymbol{\alpha}(\boldsymbol{\ell}')\cdot(\boldsymbol{\ell}-\boldsymbol{\ell}')\right]^2 \tilde{C}_{\left|\boldsymbol{\ell}-\boldsymbol{\ell}'\right|} \tag{4.13}$$

and we have used the definition of the power spectrum,

$$\left\langle T^*(\boldsymbol{\ell})T(\boldsymbol{\ell}')\right\rangle = (2\pi)^2 C_\ell\delta(\boldsymbol{\ell}-\boldsymbol{\ell}'). \tag{4.14}$$

In equation (4.12), N_ℓ is the instrumental noise for the CMB experiment, and is given by

$$N_\ell = 4\pi f_{\rm sky}\frac{\tau^2}{t_{\rm obs}N_{\rm det}}\exp\left[\frac{\ell(\ell+1)\theta^2_{\rm FWHM}}{8\ln 2}\right] \tag{4.15}$$

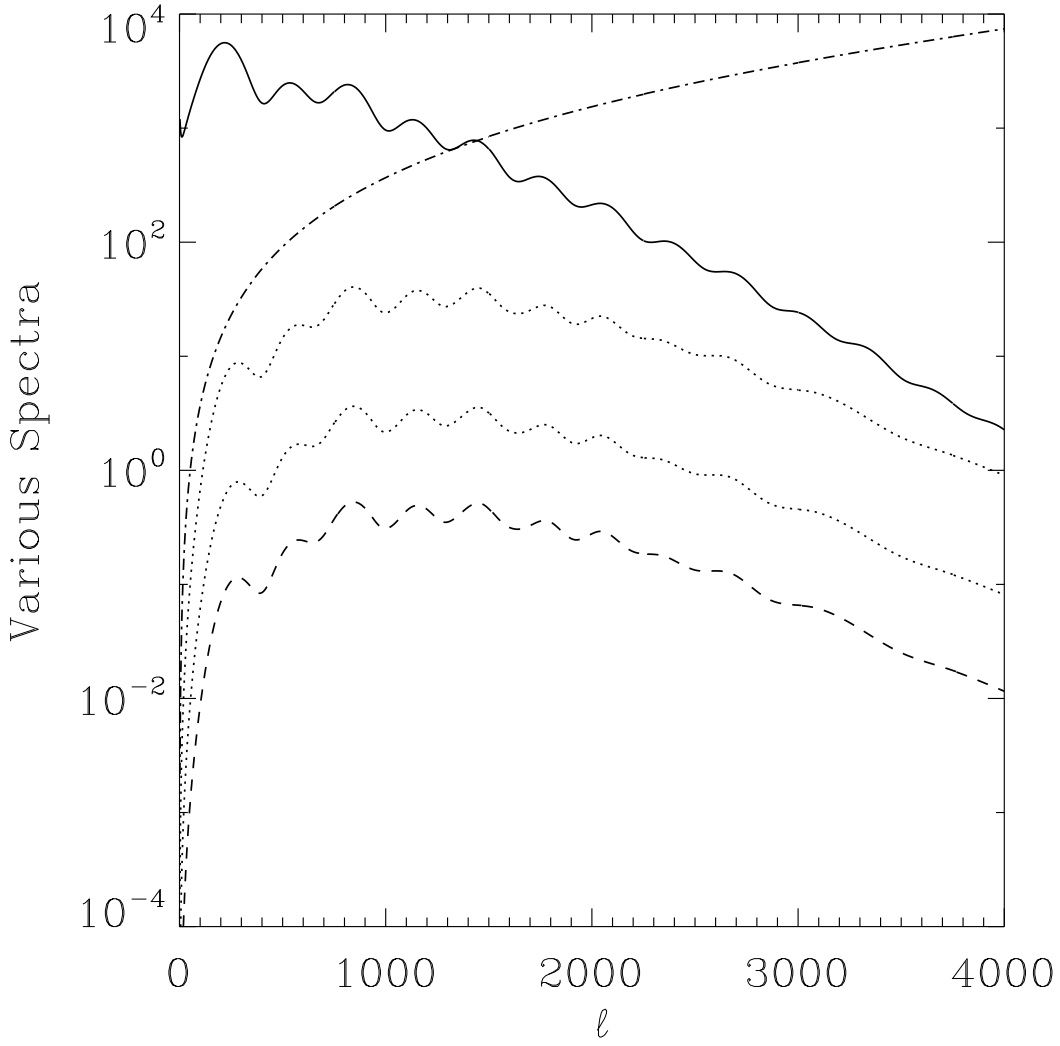

Figure 4.1: Various terms that enter the calculation of the signal to noise equation (4.12). The solid curve represents the CMB power spectrum C_ℓ, while the dot-dashed curve represents the instrumental noise for the assumed experimental specifications (see text) and for an exposure time of 16 minutes. The upper (lower) dotted curve represents S_ℓ for the void with $\delta = -1$ ($\delta = -0.3$). The dashed line represents S_ℓ for the texture.

where τ is noise-equivlent-temperature of each detector (usually expressed in $\mu K\sqrt{s}$), $t_{\rm obs}$ is the duration of observation, $N_{\rm det}$ is the number of detectors and $\theta_{\rm FWHM}$ is the full-width-at-half-maximum of the beam, assuming it to be Gaussian.

In order to evaluate S_ℓ, we compute the Fourier transforms of the deflection fields due to the void equation (4.1) and the texture equation (4.5),

$$\boldsymbol{\alpha}(\boldsymbol{\ell}) = \begin{cases} -i\boldsymbol{\ell}\ 4\pi A_V R_V J_1(\ell R)/\ell^3 & \text{(Void)} \\ i\boldsymbol{\ell}\ \frac{\pi}{2} A_T R_T\ e^{-\ell R_T/2}(\ell R_T + 2)/\ell^3 & \text{(Texture).} \end{cases} \tag{4.16}$$

Various spectra that enter the calculation of the signal to noise are depicted in Fig. 4.1. For the void we have considered two cases: a completely empty $\delta = -1$ case, which is a toy model suggested by (Rudnick et al., 2007) and the $\delta = -0.3$ case as modeled in detail by (Inoue & Silk, 2006). As expected, the signal variance S_ℓ for the texture is about an order of magnitude smaller than that of the void with $\delta = -0.3$. To calculate the signal to noise, we consider a CMB experiment with a $1'$ beam and a detector array with $N_{\rm det} = 800$ detectors, each having a noise-equivalent-temperature, $\tau = 300\ \mu K\ \sqrt{s}$. We assume that the instrument spends an amount of time $t_{\rm obs}$ on a 8° square patch containing the Cold Spot, so that $f_{\rm sky} \sim 1.55 \times 10^{-3}$. Figure 4.2 displays the signal to noise ratio for the detection of the deflection template as a function of exposure time. It is seen that the void should be readily detectable (or ruled out) at high significance with exposure times of only a few minutes. On the other hand, a significant detection of the texture would require several hours of integration. The calculations above suggest that both the void and the texture hypotheses can be easily tested by any of the ongoing and upcoming experiments, although realistically, the texture case may need some dedicated allocation of time at the Cold Spot.

4.5 Conclusion

If either a texture or a void is responsible for the WMAP cold spot, then there should be a distinctive lensing signature seen in the CMB. We have shown that a void would gravita-

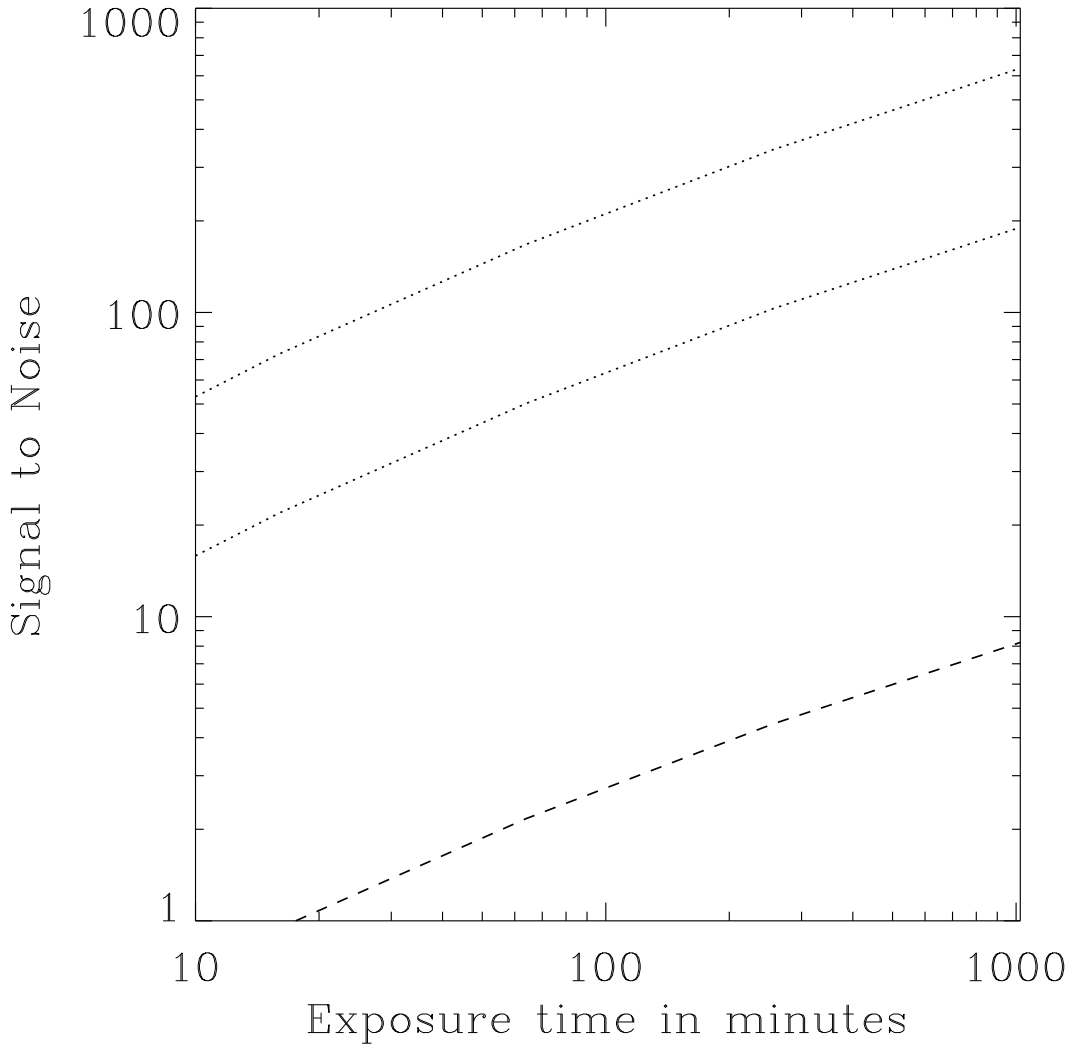

Figure 4.2: Signal to noise for the detection of the lensing template by the experiment described in the text, as a function of the time of exposure of an 8° square region centered on the Cold Spot. The upper (lower) dotted line corresponds to the case for the void with $\delta = -1$ ($\delta = -0.3$). The dashed line represent the case for the cosmic texture.

tionally lens the CMB photons appreciably so that its presence should be detectable at high significance with arcminute scale CMB experiments. For a cosmic texture that collapsed at $z \sim 6$, we find that the gravitational lensing effect on the CMB is more subtle than the void, but should be detectable with longer integration. Together with other indicators, like the power spectrum and the bispectrum (Masina & Notari, 2008) and measurements of the temperature-polarization cross-correlation Cruz et al. (2007b), CMB lensing appears to be a powerful aid in constraining the theories of the WMAP cold spot anomaly.

Acknowledgements

Sudeep Das thanks APC, Paris for its hospitality during his visit to work on this project. Das and Spergel acknowledge NASA grant NNX08AH30G and NSF grant 0707731.

References

Amendola, L., Frieman, J. A., & Waga, I. 1999, Mon. Not. R. Astron. Soc, 309, 465

Bartelmann, M. & Schneider, P. 2001, Physics Reports, 340, 291

Bennett, C. L., Halpern, M., Hinshaw, G., Jarosik, N., Kogut, A., Limon, M., Meyer, S. S., Page, L., Spergel, D. N., Tucker, G. S., Wollack, E., Wright, E. L., Barnes, C., Greason, M. R., Hill, R. S., Komatsu, E., Nolta, M. R., Odegard, N., Peiris, H. V., Verde, L., & Weiland, J. L. 2003, ApJS, 148, 1

Bevis, N., Hindmarsh, M., & Kunz, M. 2004, Phys. Rev. D, 70, 043508

Colberg, J. M., Sheth, R. K., Diaferio, A., Gao, L., & Yoshida, N. 2005, Mon. Not. R. Astron. Soc, 360, 216

Cruz, M., Cayón, L., Martínez-González, E., Vielva, P., & Jin, J. 2007a, ApJ, 655, 11

Cruz, M., Martínez-González, E., Vielva, P., & Cayón, L. 2005, Mon. Not. R. Astron. Soc, 356, 29

Cruz, M., Martinez-Gonzalez, E., Vielva, P., Diego, J. M., Hobson, M., & Turok, N. 2008, ArXiv e-prints, 804

Cruz, M., Tucci, M., Martínez-González, E., & Vielva, P. 2006, Mon. Not. R. Astron. Soc, 369, 57

Cruz, M., Turok, N., Vielva, P., Martínez-González, E., & Hobson, M. 2007b, Science, 318, 1612

Dodelson, S. 2004, Phys. Rev. D, 70, 023009

Dunkley, J., Komatsu, E., Nolta, M. R., Spergel, D. N., Larson, D., Hinshaw, G., Page, L., Bennett, C. L., Gold, B., Jarosik, N., Weiland, J. L., Halpern, M., Hill, R. S., Kogut, A., Limon, M., Meyer, S. S., Tucker, G. S., Wollack, E., & Wright, E. L. 2008, ArXiv e-prints, 803

Durrer, R., Heusler, M., Jetzer, P., & Straumann, N. 1992, Nuclear Physics B, 368, 527

Hirata, C. M. & Seljak, U. 2003, Phys. Rev. D, 67, 043001

Hoyle, F. & Vogeley, M. S. 2004, ApJ, 607, 751

Hu, W., DeDeo, S., & Vale, C. 2007, New Journal of Physics, 9, 441

Hu, W. & Okamoto, T. 2002, ApJ, 574, 566

Inoue, K. T. & Silk, J. 2006, ApJ, 648, 23

—. 2007, ApJ, 664, 650

Lewis, A. & King, L. 2006, Phys. Rev. D, 73, 063006

Masina, I. & Notari, A. 2008, ArXiv e-prints, 808

Maturi, M., Bartelmann, M., Meneghetti, M., & Moscardini, L. 2005, A&A, 436, 37

Patiri, S. G., Betancort-Rijo, J. E., Prada, F., Klypin, A., & Gottlöber, S. 2006, Mon. Not. R. Astron. Soc, 369, 335

Platen, E., van de Weygaert, R., & Jones, B. J. T. 2008, Mon. Not. R. Astron. Soc, 387, 128

Rees, M. J. & Sciama, D. W. 1968, Nature, 217, 511

Rudnick, L., Brown, S., & Williams, L. R. 2007, ApJ, 671, 40

Seljak, U. & Zaldarriaga, M. 2000, ApJ, 538, 57

Shandarin, S., Feldman, H. A., Heitmann, K., & Habib, S. 2006, Mon. Not. R. Astron. Soc, 367, 1629

Smith, K. M. & Huterer, D. 2008, ArXiv e-prints, 805

Sunyaev, R. A. & Zeldovich, Y. B. 1970, Ap&SS, 7, 3

Turok, N. 1989, Phys. Rev. Lett., 63, 2625

Turok, N. & Spergel, D. 1990, Physical Review Letters, 64, 2736

Vale, C., Amblard, A., & White, M. 2004, New Astronomy, 10, 1

Vielva, P., Martínez-González, E., Barreiro, R. B., Sanz, J. L., & Cayón, L. 2004, ApJ, 609, 22

Yoo, J. & Zaldarriaga, M. 2008, ArXiv e-prints, 805

Appendix A

Next Generation Redshift Surveys and the Origin of Cosmic Acceleration

Abstract

Cosmologists are exploring two possible sets of explanations for the remarkable observation of cosmic acceleration: dark energy fills space or general relativity fails on cosmological scales. We define a null test parameter $\epsilon(k,a) \equiv \Omega_m^{-\gamma} d\ln D/d\ln a - 1$, where a is the scale factor, D is the growth rate of structure, $\Omega_m(a)$ is the matter density parameter, and γ is a simple function of redshift. We show that it can be expressed entirely in terms of the bias factor, $b(a)$, (measured from cross-correlations with CMB lensing) and the amplitude of redshift space distortions, $\beta(k,a)$. Measurements of the CMB power spectrum determine $\Omega_{m\,0}H_0^2$. If dark energy within GR is the solution to the cosmic acceleration problem, then the logarithmic growth rate of structure $d\ln D/d\ln a = \Omega_m^{\gamma}$. Thus, $\epsilon(k,a) = 0$ on linear scales to better than 1%. We show that in the class of Modified Gravity models known as $f(R)$, the growth rate has a different dependence on scale and redshift. By combining measurements of the amplitude of β and of the bias, b, redshift surveys will be able to

determine the logarithmic growth rate as a function of scale and redshift. We estimate the predicted sensitivity of the proposed SDSS III (BOSS) survey and the proposed ADEPT mission and find that they will test structure growth in General Relativity to the percent level.

A.1 Introduction

In General Relativity (GR), there are four variables characterizing linear cosmic perturbations: the two gravitational potentials Ψ and Φ, the anisotropic stress, σ, and the pressure perturbation, δp. All of these variables can depend on the wave number, k, and the expansion factor a. We focus initially on models with no dark energy clustering or pressure and discuss these effects later in the paper. We assume scalar linear perturbations around a flat FRW background in the Newtonian gauge,

$$ds^2 = -(1+2\Psi)dt^2 + a^2(1+2\Phi)dx^2 \tag{A.1}$$

and work in the quasi-static, linear approximation, which is valid for sub-horizon modes still in the linear regime.

The evolution of perturbations is described by the continuity, Euler and Poisson equations (*i.e.* Jain & Zhang (2007)):

$$\begin{aligned} \Delta_m' &= -k_H V_m, & \text{(A.2)} \\ V_m' + V_m &= \frac{k}{aH}\Psi, & \text{(A.3)} \\ k^2\Phi &= -4\pi G a^2 \rho_m \Delta_m. & \text{(A.4)} \end{aligned}$$

With the assumption of no anisotropic stress, $\Phi = -\Psi$, these equations can be combined to derive the equation of motion for the growth factor D, defined as $D(k,z) = \delta_m(k,z)/\delta_m(k,z=\infty)$:

$$D'' + (2 + \frac{H'}{H})D' - \frac{4\pi G}{H^2}\rho_m D = 0; \tag{A.5}$$

where $H = \dot{a}/a$ is the Hubble function, and a prime denotes derivative with respect to $\ln a$. From Eq. (A.5) one can infer the two key features of GR with smooth dark energy. First, the growth factor is exactly determined once the Hubble function $H(a)$ is known; and second, since none of the coefficients is a function of scale, the growth factor is scale-independent. Therefore, for a given expansion history, one can test GR in two ways: checking that the theoretical solution of Eq. (A.5) agrees with observations, and testing the hypothesis of scale-independence (Bertschinger & Zukin, 2008; Bertschinger, 2006; Ishak et al., 2006; Daniel et al., 2008; Dore et al., 2007; Linder & Cahn, 2007; Zhang et al., 2007; Wang, 2007; Sahni & Starobinsky, 2006; Yamamoto et al., 2008) . The growth rate of structure in GR is well approximated by Ω_m^γ, where the fitting function $\gamma(z) \simeq 0.557 - 0.02z$ is accurate at the 0.3% level (Polarski & Gannouji, 2007). We define a function that tests the growth rate of structure and can be directly related to observables:

$$\epsilon(k,a) = \Omega_m^{-\gamma(a)} \frac{d\ln D}{d\ln a} - 1 = \frac{a^{3\gamma} H(a)^{2\gamma}}{(\Omega_{m,0} H_0^2)^\gamma} \frac{d\ln D}{d\ln a} - 1. \tag{A.6}$$

The combination $\Omega_{m,0}H_0^2$ can be constrained via CMB measurements; it is currently known to within the 5% level fro the WMAP5 data (Dunkley et al., 2008), with an expected gain of a factor $\simeq 4$ from the upcoming satellite CMB mission Planck. The solid line in Fig. A.1 shows $\epsilon(a)$ in GR with dark energy: regardless of the details of the dark energy model, $\epsilon(a) \simeq 0$ in the linear regime. By measuring this quantity, we can characterize deviations from General Relativity.

A.2 f(R) theories in the PPF formalism

To quantify the expected deviations, we study a class of modified gravity (MoG) models known as $f(R)$ theories, whose action is written as

$$\mathcal{S} = \frac{1}{16\pi G} \int d^4x \sqrt{-g}(R + f(R)) + \mathcal{S}_m; \tag{A.7}$$

S_m is the action of standard matter fields. It has been noted long ago (Carroll et al., 2004; Capozziello et al., 2003) that models where $f(R)$ is an inverse power of the Ricci scalar can

give rise to late-time acceleration; however, many of those models have been shown not to be cosmologically viable due to gravitational instability (Dolgov & Kawasaki, 2003).

Recently, Song et al. (2007) introduced an effective parametrization for $f(R)$ theories which does not rely on any particular model and is able to discard models suffering from instabilities. The cosmological evolution is obtained by fixing the expansion history to match that of a dark energy model, for which we assume a constant equation of state w:

$$H^2 = H_0^2(\Omega_m a^{-3} + (1-\Omega_m)a^{-3(1+w)}). \tag{A.8}$$

Such requirement for $H(a)$ translates into a second-order equation for $f(R)$, which can be solved numerically. Of the two initial conditions of this equation, one can be fixed requiring that $f(R)/R \to 0$ at early times (*i.e.* for large R) in order to recover GR; the second defines a one-parameter family of curves which all generate the given $H(a)$. Such parameter is conveniently chosen as (also see Starobinsky (2007)):

$$B_0 = \left(\frac{f_{RR}}{1+f_R}R'\frac{H}{H'}\right)_0. \tag{A.9}$$

Here f_R and f_{RR} represent the first and second derivative of f with respect to R, respectively. GR is represented by the special case $B_0 = 0$, so that B_0 effectively quantifies the deviation from GR at the present time. Furthermore, the gravitational stability condition is easily established as $B_0 > 0$.

The additional degrees of freedom of the $f(R)$ gravity introduce modifications in the Poisson equation and in the relation between the two gravitational potentials (Jain & Zhang, 2007), which now read:

$$k^2(\Phi - \Psi) = 4\pi G_{\rm eff}(k,a)a^2\rho_m\Delta_m \tag{A.10}$$

and

$$\Psi = (g(k,a)-1)\frac{k}{aH}(\Phi - \Psi). \tag{A.11}$$

The equation for the growth factor in MoG takes the form:

$$D'' + (2 + \frac{H'}{H})D' + \frac{4\pi G_{\rm eff}(k,z)(g(k,z)-1)}{H^2}\rho_m D = 0. \tag{A.12}$$

Given $H(a)$, a MoG model is not completely defined unless $G_{\rm eff}(k,a)$, the effective Newton's Constant, and the metric ratio $g(k,a) = (\Phi+\Psi)/(\Phi-\Psi)$, are known, contrary to the GR case. For the class of $f(R)$ theories under study, and in the sub-horizon, linear regime, Hu & Sawicki (2007a) have provided a fit to $G_{\rm eff}$ and g as

$$\begin{aligned} G_{\rm eff}(k,a) &= G_{\rm eff}(a) = \frac{G_N}{1+f_R}, \\ g(k,a) &= \frac{g_{SH}(a) - \frac{1}{3}(0.71\sqrt{B}(k/aH))^2}{1+(0.71\sqrt{B}(k/aH))^2}, \end{aligned} \tag{A.13}$$

where B is the function appearing in Eq. (A.9), and $g_{SH}(a)$ is the super-horizon metric ratio (see Song et al. (2007); Hu & Sawicki (2007a) for details).

The key result is that the $f(R)$ models all predict an enhancement in the growth rate of structure. In fact, any positive value of B_0 gives rise to a negative f_R, so that the effective Newton constant is larger with respect to GR. Moreover, both terms in $g(k,a)$ have a negative sign, which induce further enhancement of matter clustering, as can be seen from Eq. (A.12). Since $G_{\rm eff}(k,z) = G_N/(1+f_R)$ does not depend on k, the scale dependence of the growth factor can only arise from the second term of Eq. (A.13). On large scales, the dominant term in the metric ratio is $g_{SH}(a)$, while for increasing values of k, the second term in the expression for $g(k,a)$ becomes important and tends to the constant value of $-1/3$ for large k. The scale of the transition from scale-free to scale-dependent growth factor is $k/aH \simeq B^{-1/2}$; due to the asymptotic behavior of $g(k,a)$, the growth differs significantly from GR even for models with very small values of B_0, on sufficiently small scales. A mechanism to restore GR on scales of the galaxy and smaller is discussed in (Hu & Sawicki, 2007b,a). Fig. A.1 shows $d\ln(D)/d\ln(a)\Omega_m(a)^\gamma - 1$ for a few different values of B_0 and k/aH_0. For the GR case, $B_0 = 0$, $\epsilon(k,a) - 1 \simeq 0$ with no scale dependence.

A.3 Measuring the growth of structure

Peculiar velocities displace galaxies along the line of sight in redshift space and distort the power spectrum of galaxies observed in redshift space. This effect is known as linear redshift space distortion and was first derived by Kaiser (1987). In redshift-space, the power

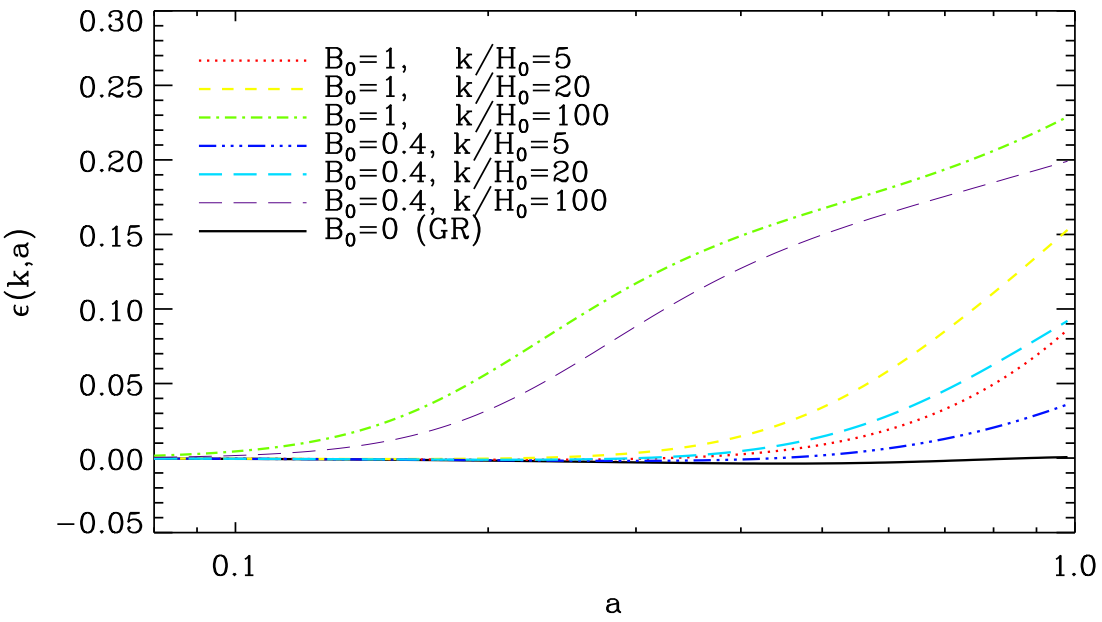

Figure A.1: The behavior of $\epsilon(k,a) = \Omega_m^{-\gamma} d\ln D/d\ln a - 1$ in GR (solid line) and in $f(R)$ models, as a function of B_0 and k. Growth is enhanced for $B_0 \neq 0$ and at smaller scales in alternative theories. In GR, $\epsilon(a) = 0$.

spectrum is amplified by a factor $(1+\beta\mu_{\mathbf{k}}^2)^2$ over its real-space counterpart,

$$P^s(\mathbf{k}) = (1+\beta\mu_{\mathbf{k}}^2)^2 P(k), \tag{A.14}$$

where $P^s(\mathbf{k})$ and $P(k)$ are redshift and real space power spectra, respectively, $\mu_{\mathbf{k}} = \hat{z}\cdot\hat{k}$ is the cosine of the angle between the wavevector $\hat{k}$ and the line of sight $\hat{z}$, and β is the linear redshift-space distortion parameter defined as

$$\beta(a) = \frac{1}{b}\frac{d\ln D}{d\ln a}; \tag{A.15}$$

b is the linear bias, which we assume to be independent of scale.

Galaxy redshift surveys can be used to directly measure β, and, if the bias is known, the growth rate of perturbations. In fact, the redshift space power spectrum can be decomposed into harmonics, whose relative amplitude depend on the growth rate of structure through β. The possibility of using such dependence in order to constrain dark energy properties has been explored in Guzzo et al. (2008); here we focus on the measurements of the scale dependence of β as a smoking gun of Modified Gravity.

We assume that β is obtained through the ratio of quadrupole to monopole moments of the redshift power spectrum (Hamilton, 1997)

$$\frac{P_2(k)}{P_0(k)} = \frac{\frac{4}{3}\beta + \frac{4}{7}\beta^2}{1+\frac{2}{3}\beta+\frac{1}{5}\beta^2}, \tag{A.16}$$

and use the prescription in Feldman et al. (1994) to get the errors in the above quantities:

$$\frac{\sigma(P_i(k))}{P_i(k)} = \left(\frac{(2\pi)^3\int d^3\mathbf{r}\bar{n}^4(\mathbf{r})\psi^4(\mathbf{r})[1+\frac{1}{\bar{n}(\mathbf{r})P_i(k)}]^2}{V_k\left[\int d^3\mathbf{r}\bar{n}^2(\mathbf{r})\psi^2(\mathbf{r})\right]^2}\right)^{1/2} \tag{A.17}$$

where $\bar{n}(\mathbf{r})$ is the mean galaxy density, ψ is the weight function, V_k is the volume of the shell in k-space, and the index "i" assumes the values 0 and 2 for monopole and quadrupole, respectively.

The linear bias for a population of large-scale structure tracers can be estimated by cross-correlating the line-of-sight projected density of the tracer with a convergence map reconstructed by CMB lensing techniques, and comparing the resulting signal with theory.

The weak lensing potential responsible for lensing the CMB can be written as the line-of-sight integral (Bartelmann & Schneider, 2001),

$$\phi(\hat{\boldsymbol{n}}) = -\int d\eta \frac{d_A(\eta_0 - \eta)}{d_A(\eta_0) d_A(\eta)} [\Phi - \Psi](d_A(\eta)\hat{\boldsymbol{n}}, \eta), \tag{A.18}$$

where $d_A(\eta)$ is the comoving angular diameter distance corresponding to the comoving distance η, and η_0 is the comoving distance to the last scattering surface. A quadratic combination of the measured CMB temperature and polarization (Hu & Okamoto, 2002; Okamoto & Hu, 2003; Hirata & Seljak, 2003) provides an estimator of the convergence field, $\kappa = \frac{1}{2}\nabla^2\phi$. In this study, we have used the prescription of Hu & Okamoto (2002) to compute the expected noise power spectrum, $N_\ell^{\kappa\kappa}$, corresponding to the reconstructed convergence field by cross-correlating κ with the projected fractional overdensity of the tracer,

$$\Sigma(\hat{\boldsymbol{n}}) = \int d\eta W(\eta) b\, \delta_m(\eta\hat{\boldsymbol{n}}, \eta) \tag{A.19}$$

where W is the normalized tracer distribution function in comoving distance. We measure the cross-correlation spectrum:

$$C_\ell^{\kappa-\Sigma} = \frac{3}{2} b\, \Omega_m H_0^2 \int d\eta \frac{W(\eta)}{a(\eta)} P(\frac{\ell}{d_A}, \eta) \frac{d_A(\eta_0 - \eta)}{d_A(\eta) d_A(\eta_0)} \tag{A.20}$$

where $P(k, \eta)$ is the matter power spectrum at the comoving distance η and we have related the wavenumber k to the multipole ℓ via the Limber approximation (Limber, 1954). The signal-to-noise ratio for such a cross-correlation can be estimated as (Peiris & Spergel, 2000),

$$\left(\frac{S}{N}\right)^2 = f_{\rm sky} \sum (2\ell + 1) \frac{\left(C_\ell^{\kappa-\Sigma}\right)^2}{\left(C_\ell^{\kappa\kappa} + N_l^{\kappa\kappa}\right)\left(C_\ell^{\Sigma\Sigma} + N_\ell^{\Sigma\Sigma}\right)} \tag{A.21}$$

where $f_{\rm sky}$ is the fraction of sky over which the cross-correlation is performed. For tracer counts the noise is Poisson, and the power spectrum is given by, $N_\ell^{\Sigma\Sigma} = 1/\hat{n}$ where $\hat{n}$ is the number of tracer objects per steradian.

Since the signal is proportional to the bias, b, the expected error on b can be written as

$$\Delta b/b \simeq 1/(S/N). \tag{A.22}$$

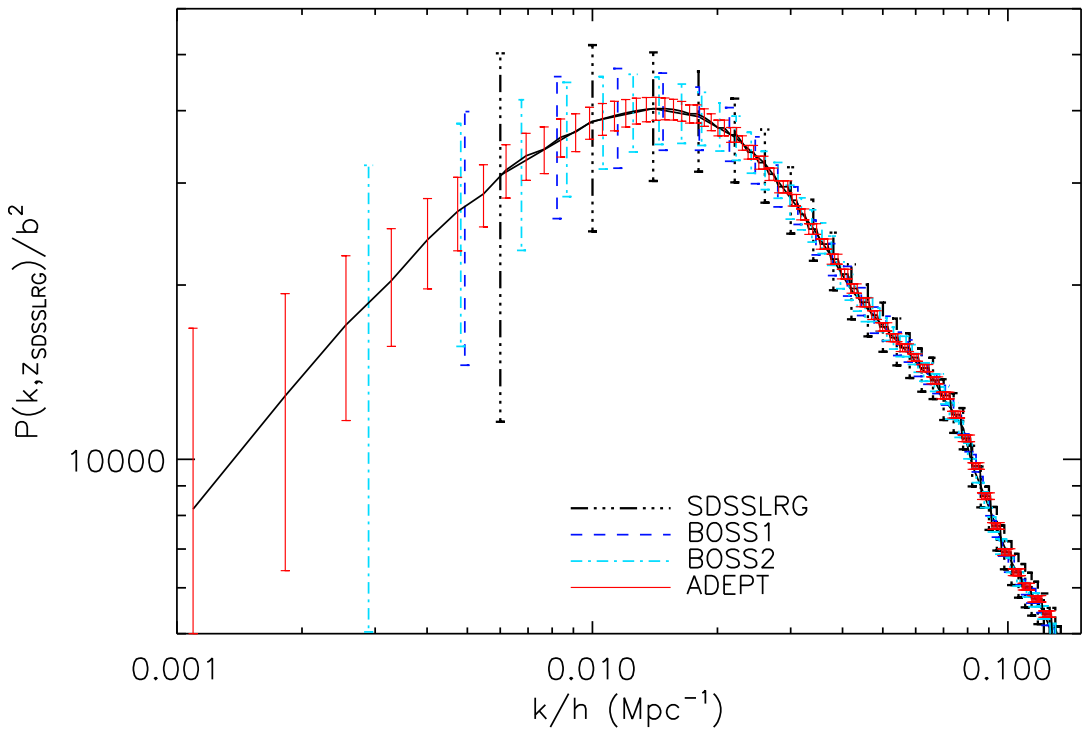

Figure A.2: Errors on $P(k)$, normalized to the SDSS-LRG median redshift (z=0.31) for all surveys.

We consider three present and forthcoming redshift galaxy surveys: the SDSS LRG sample (Tegmark et al., 2006), its extension BOSS-LRG [1] , which we divide in two redshift bins, labeled as BOSS1 and BOSS2, and the proposed survey ADEPT [2] . Specifics of each experiment are listed in Table A.1. In all cases we assume that β and b do not change significantly with redshift within a survey, so that the observed quantity is $\beta(k, z_c)$, where z_c is roughly the central redshift of the survey. As a direct comparison the capabilities of the three galaxy surveys under examination, we show the real space matter power spectrum, normalized to the SDSS LRGs median redshift, with its errorbars in Fig. A.2. We also consider three possible CMB experiments: a PLANCK-like CMB experiment with 65% sky coverage and temperature and polarization sensitivities of 28 μK-arcmin and 57 μK-arcmin, respectively;

[1] www.sdss3.org
[2] www7.nationalacademies.org/ssb/be_nov_2006_bennett.pdf

Galaxy Survey	$\hat{n}$	$A/10^3$	z_c	b	CMB Expt.	(S/N)	$\Delta b/b(\%)$
					PLANCK	5.8	17.3
SDSSLRG	12.4	3.8	0.31	2	PACT	11.4	8.8
					IDEAL	20.4	4.9
					PLANCK	10.8	9.3
BOSS1	40.	10	0.3	2	PACT	25.5	3.9
					IDEAL	52.5	1.9
					PLANCK	17.0	5.9
BOSS2	110.	10	0.6	2	PACT	39.4	2.5
					IDEAL	78.2	1.3
					PLANCK	52.8	1.9
ADEPT	3500	27	1.35	1	PACT	107.5	0.9
					IDEAL	228.3	0.4

Table A.1: Predictions for the errors on bias from the cross-correlation studies described in the text. For each combination of experiments, we display the number of galaxies per square degree ($\bar{n}$); the area of overlap (A), the signal-to-noise with which the cross correlation of tracer surface density with CMB-lensing can be extracted, (S/N), and the percentage error in the bias, b, for the tracer.

a next generation CMB survey based on using a camera similar to that on ACT or SPT with a polarimeter and a ~ 3 years observing program (labeled PACT) with 65% sky coverage and temperature and polarization sensitivities of 13 μK-arcmin and 18 μK-arcmin and an ideal polarization experiment (labeled IDEAL), with 65% sky coverage and temperature and polarization sensitivities of 1 μK-arcmin and 1.4 μK-arcmin, respectively. The expected results from cross-correlation with the ADEPT and BOSS surveys, and the SDSS LRG are displayed in Table A.1.

A.4 Results

We show our main results in Fig. A.3. Errorbars are computed using Planck as the complementary CMB lensing survey for SDSS LRG and BOSS, and PACT for ADEPT. We summarize the current status of β and bias measurements in Table A.2, and add the expected errorbars on ϵ at two different scales, $k/h = 0.05$ Mpc^{-1} and $k/h = 0.2$ Mpc^{-1}, from our analysis, for comparison.

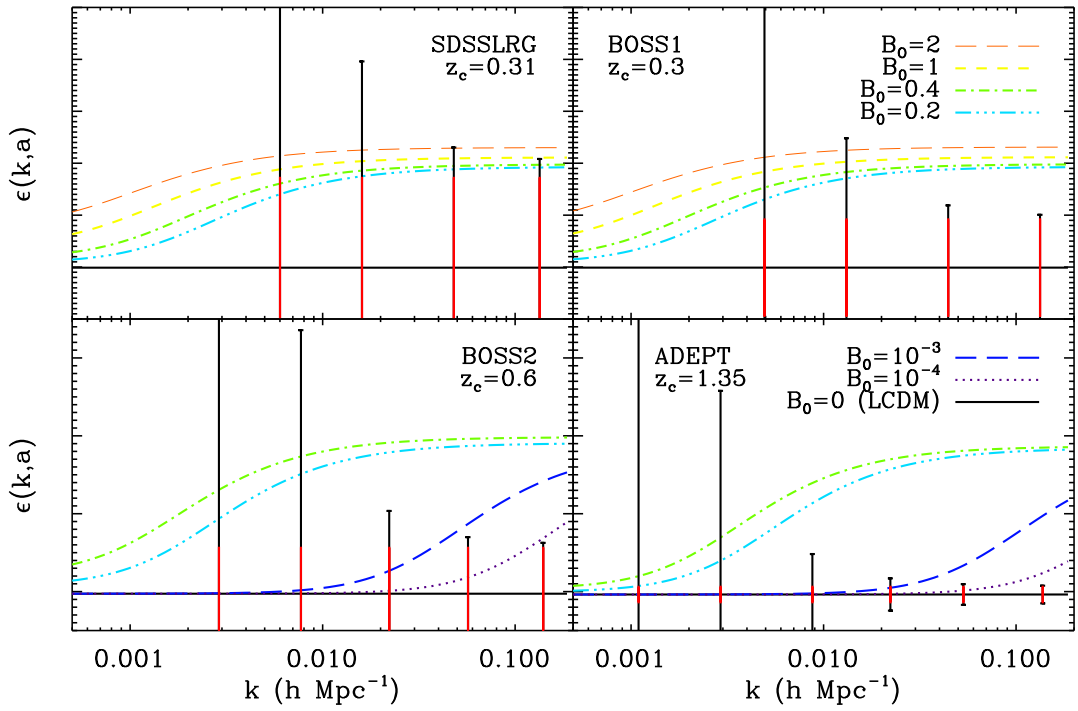

Figure A.3: $\epsilon(k, z)$ for the four surveys, as a factor of B_0 and k. Total errorbars around the ΛCDM case are shown in black; the smaller red errorbars are from bias only.

The errors on bias are scale-independent and vary from 17% for SDSS LRG to ~ 1 % for ADEPT. Errors on β depend on scale; we bin our simulated data in bins in k space of width $\Delta \ln k = 1/e$, and see that for all surveys errorbars decrease as we go to smaller scales. The corresponding constraints on ϵ are as strong as a few percent for BOSS, and of the order of 1% for ADEPT.

The combined effect of smaller errors and of the asymptotic behavior of the growth factor, which induces a large deviation of $\epsilon(k, a)$ from its GR value on small scales, is that redshift galaxy surveys are more sensitive to the small-scale modification of gravity than to the large-scale one. Ultimately, the smallest observable value of B_0 will not be set by the capabilities of the survey, but by the breakdown of the linear regime assumption. Assuming $k \simeq 0.05$ Mpc^{-1} as an upper limit, and for values of aH corresponding to redshifts between 0 and 2, the smallest B_0 inducing scale-dependent growth is $B_0 \simeq 10^{-4}$. Such value is within reach of ADEPT; future experiments that detect redshifted 21 centimeter emission could probe even larger values of k/aH in the linear regime.

A.5 Conclusions and discussion

We have built a null test parameter for General Relativity, $\epsilon(k, a)$, based on the consistency between expansion history and structure growth expected in GR. Such parameter can be expressed in terms of the combination $\Omega_{0m}h^2$, probed by the CMB experiments, the linear matter perturbations growth factor, probed by redshift galaxy surveys, and the linear bias, probed by cross-correlation of the two.

We have predicted the achievable precision in the measurement of $\epsilon(k, a)$ for three redshift galaxy surveys, SDSS LRG, BOSS and ADEPT, together with Planck and a possible future CMB experiment, PACT. We have interpreted such result in the context of a one-parameter family of modified gravity theories, known as $f(R)$, which can give rise to cosmic acceleration. In such models, the matter clustering is enhanced on all scales with respect to the GR case, and the enhancement is largest on small scales. We concluded that the peculiar signatures of the $f(R)$ theories will be definitely detectable with a survey like ADEPT.

Table A.2: Currently available data for measurements of ϵ through β and b (from Nesseris & Perivolaropoulos (2008), with the addition of the measurement reported in Guzzo et al. (2008)), and comparison with our predictions. Only the error coming from uncertainties in β and b is considered.

z	β	b	$\Delta\epsilon/\epsilon(\%)$	Ref.	z	$\Delta\epsilon/\epsilon(\%)$ $k = 0.05\,h$/Mpc	$\Delta\epsilon/\epsilon(\%)$ $k = 0.2\,h$/Mpc	COMBINATION OF SURVEYS
0.15	0.49 ± 0.09	1.04 ± 0.11	21.5	Hawkins et al. (2003),Verde et al. (2002)	0.3	22.0	10.1	BOSS1 + Planck
0.35	0.31 ± 0.04	2.25 ± 0.08	25.7	Tegmark et al. (2006)	0.31	39.5	21.0	SDSS LRG + Planck
0.55	0.45 ± 0.05	1.66 ± 0.35	24.0	Ross et al. (2006)	0.5	9.3	5.5	BOSS + Planck
0.77	0.70 ± 0.26	1.3 ± 0.1	39.6	Guzzo et al. (2008)	0.6	10.6	6.5	BOSS2 + Planck
1.4	$0.60^{+0.14}_{-0.11}$	1.5 ± 0.20	27.7	da Angela et al. (2006)	1.35	2.1	1.1	ADEPT + PACT
3.0	–	–	19.9	McDonald et al. (2005)				

More generally, any detection of deviation of ϵ from zero that was not due to some observational systematic would be a signature of truly novel physics with enhanced growth, pointing either to non-GR physics or to unexpected properties of dark energy: dark energy models with a non-zero sound speed are characterized by an oscillatory behavior of the growth (DeDeo et al., 2003), and scalar field dark energy suppresses growth on large scales (Unnikrishnan et al., 2008). Similarly, massive neutrinos suppress $\epsilon(k, a)$ on scales below the neutrino free streaming scale (see Lesgourgues & Pastor (2006) for review).

We warmly thank E. Aubourg, C. Hirata, W. Hu, R. H. Lupton, M. A. Strauss and L. Verde for useful suggestions. DNS thanks the APC in Paris for its hospitality. This work was supported by NSF grant AST-0707731, the NSF PIRE program and the NASA LTSA program.

References

Bartelmann, M. & Schneider, P. 2001, Phys. Rept., 340, 291

Bertschinger, E. 2006, Astrophys. J., 648, 797

Bertschinger, E. & Zukin, P. 2008

Capozziello, S., Carloni, S., & Troisi, A. 2003

Carroll, S. M., Duvvuri, V., Trodden, M., & Turner, M. S. 2004, Phys. Rev., D70, 043528

da Angela, J. et al. 2006

Daniel, S. F., Caldwell, R. R., Cooray, A., & Melchiorri, A. 2008

DeDeo, S., Caldwell, R. R., & Steinhardt, P. J. 2003, Phys. Rev., D67, 103509

Dolgov, A. D. & Kawasaki, M. 2003, Phys. Lett., B573, 1

Dore, O. et al. 2007

Dunkley, J. et al. 2008

Feldman, H. A., Kaiser, N., & Peacock, J. A. 1994, Astrophys. J., 426, 23

Guzzo, L. et al. 2008, Nature, 451, 541

Hamilton, A. J. S. 1997

Hawkins, E. et al. 2003, Mon. Not. Roy. Astron. Soc., 346, 78

Hirata, C. M. & Seljak, U. 2003, Phys. Rev., D67, 043001

Hu, W. & Okamoto, T. 2002, Astrophys. J., 574, 566

Hu, W. & Sawicki, I. 2007a, Phys. Rev., D76, 104043

—. 2007b, Phys. Rev., D76, 064004

Ishak, M., Upadhye, A., & Spergel, D. N. 2006, Phys. Rev., D74, 043513

Jain, B. & Zhang, P. 2007

Kaiser, N. 1987, Mon. Not. Roy. Astron. Soc., 227, 1

Lesgourgues, J. & Pastor, S. 2006, Phys. Rept., 429, 307

Limber, D. N. 1954, Astrophys. J., 119, 655

Linder, E. V. & Cahn, R. N. 2007, Astropart. Phys., 28, 481

McDonald, P. et al. 2005, Astrophys. J., 635, 761

Nesseris, S. & Perivolaropoulos, L. 2008, Phys. Rev., D77, 023504

Okamoto, T. & Hu, W. 2003, Phys. Rev., D67, 083002

Peiris, H. V. & Spergel, D. N. 2000, Astrophys. J., 540, 605

Polarski, D. & Gannouji, R. 2007

Ross, N. P. et al. 2006

Sahni, V. & Starobinsky, A. 2006, Int. J. Mod. Phys., D15, 2105

Song, Y.-S., Hu, W., & Sawicki, I. 2007, Phys. Rev., D75, 044004

Starobinsky, A. A. 2007, JETP Lett., 86, 157

Tegmark, M. et al. 2006, Phys. Rev., D74, 123507

Unnikrishnan, S., Jassal, H. K., & Seshadri, T. R. 2008

Verde, L. et al. 2002, Mon. Not. Roy. Astron. Soc., 335, 432

Wang, Y. 2007

Yamamoto, K., Sato, T., & Huetsi, G. 2008

Zhang, P., Liguori, M., Bean, R., & Dodelson, S. 2007, Phys. Rev. Lett., 99, 141302